Collot, J.-Y., Greene, H. G., Stokking, L. B., et al., 1992
Proceedings of the Ocean Drilling Program, Initial Reports, Vol. 134

8. SITE 828[1]

Shipboard Scientific Party[2]

HOLE 828A

Date occupied: 25 October 1990

Date departed: 26 October 1990

Time on hole: 1 day, 10 hr, 30 min

Position: 15°17.34′S, 166°17.04′E

Bottom felt (rig floor; m; drill-pipe measurement): 3097.6

Distance between rig floor and sea level (m): 10.90

Water depth (drill-pipe measurement from sea level, m): 3086.7

Total depth (rig floor; m): 3209.00

Penetration (m): 111.40

Number of cores (including cores with no recovery): 15

Total length of cored section (m): 111.40

Total core recovered (m): 101.34

Core recovery (%): 91

Oldest sediment cored:
Depth below seafloor (m): 111.4
Nature: volcanic breccia
Age: early Eocene
Measured velocity (km/s): 1.548

Hard rock:
Depth below seafloor (m): 90.8
Nature: brecciated aphyric basalt
Measured velocity (km/s): 1.912

Comments: Beacon was dropped for Site 828 during approach to Site 827.

HOLE 828B

Date occupied: 26 October 1990

Date departed: 27 October 1990

Time on hole: 22 hr

Position: 15°17.26′S, 166°16.96′E

Bottom felt (rig floor; m; drill-pipe measurement): 3093.0

Distance between rig floor and sea level (m): 11.00

Water depth (drill-pipe measurement from sea level, m): 3082.0

Total depth (rig floor; m): 3222.00

Penetration (m): 129.00

Number of cores (including cores with no recovery): 4

Total length of cored section (m): 39.00

Total core recovered (m): 7.92

Core recovery (%): 20.3

Oldest sediment cored:
Depth below seafloor (m): 100.0
Nature: volcanic breccia
Age: Eocene
Measured velocity (km/s): 1.912

Comments: Washed to 90 mbsf.

Principal results: Site 828 (proposed site DEZ-1) is located on the North d'Entrecasteaux Ridge (NDR) of the d'Entrecasteaux Zone (DEZ) of ridges. It lies just west (about 2 km) of the trace of the New Hebrides subduction zone where the ridge is colliding with the New Hebrides Island Arc. A short geophysical survey was undertaken to confirm the existence of sedimentary cover that would assure proper spudding-in of the drill. The proposed site, consisting of a flat, terrace-like feature situated about a third of the way down the northern flank of the ridge, proved to be a desirable drilling place. Here basement rocks appeared to lie within 200 m of the seafloor. Beneath the flat surface of the terrace-like feature a basin exists, ponding material that may record a tectonically undisturbed history of sedimentation. The NDR is an aseismic ridge 40 km wide and 3 km high that is reported to be composed of mid-ocean ridge basalt basement rocks and covered with well-layered rocks and sediments. It is believed to be the northern termination of an Eocene subduction/obduction zone, of which remnants are exposed on New Caledonia. The collision and subduction of the NDR is thought to be responsible for clogging the subduction zone here and the formation and elevation of Wousi Bank, located on the forearc slope just opposite of the present eastern terminus of the ridge. This site was chosen to document the nature and age of the NDR and to provide a critical reference section of DEZ north-ridge rocks to enable recognition of these rocks in other drill holes. Information collected at this site will be used to determine the reaction of the accretionary wedge to collision, and whether such incorporated rocks form large blocks.

We cored 111.4 m and recovered 101.34 m of sediment and brecciated volcanic rock in Hole 828A, and penetrated only 129.0 m in Hole 828B, coring 39.0 m to recover 7.9 m of brecciated basement-like rock. Four lithostratigraphic units have been described, primarily from Hole 828A: Unit I (0–58.7 mbsf) predominantly consists of Pleistocene volcanic silt with an increasing percentage of clay downcore and unconformably(?) overlies Unit II. Unit II (58.7–69.3 mbsf) is a soupy foraminiferal ooze with nannofossils of late Miocene–early(?) Pliocene to Pleistocene age that is in sharp unconformable contact with the underlying unit (Unit III). Two subunits have been defined for Unit II. Subunit IIA (58.7–61.9 mbsf) consists of Pleistocene foraminiferal ooze with nannofossils and volcanic silt; silt and ashy layers alternate with firm to soupy beds. Subunit IIB (61.9–69.3 mbsf) consists of upper Miocene to lower Pliocene unconsolidated foraminiferal ooze and is separated from Subunit IIA by color change where the volcanic components of the sediment ends. Unit III (69.3–90.8 mbsf) is predominantly a nannofossil chalk of early to late Oligocene age lying unconformably upon Unit IV; most, if not all, of the Miocene and uppermost Oligocene appears to be absent from the core. Unit IV (90.8–111.4 mbsf) consists of an upper (90.8–106.8 mbsf) layer of volcanic breccia containing basaltic clasts and a lower (106.8–111.4 mbsf) predominantly brecciated aphyric basalt/dolerite zone. On the basis of planktonic foraminifers found in the core catcher, the age of these flows may be middle Eocene, although sediments sampled from the rest of the core proved barren, so their age could not be confirmed.

In Hole 828B only two of the above units were identified: Unit III (90.0–100.0 mbsf) composed of nannofossil chalk of latest Eocene to earliest Oligocene age and Unit IV (100.0–119.4 mbsf) of brecciated aphyric basalt/dolerite. These units correlate well with Hole 828A.

---

[1] Collot, J.-Y., Greene, H. G., Stokking, L. B., et al., 1992. *Proc. ODP, Init. Repts.*, 134: College Station, TX (Ocean Drilling Program).

[2] Shipboard Scientific Party is as given in the list of participants preceding the contents.

The rocks sampled at this site give an excellent history of the sedimentation and the tectonic movements of the ridge. The very immature volcanic breccias or scree deposits drilled at the bottom of both holes may have been derived from a nearby volcanic island. Rocks recovered from the top of Unit IV suggest a high oxidation environment, which could indicate a soil horizon formed when the ridge was near or above sea level. Distinct ash layers observed in many of the cores will be useful in dating and locating volcanic events that have occurred along the New Hebrides Island Arc and elsewhere within the region. The absence of most of the Miocene section suggests a period when the ridge was either emergent or in an area where erosion or nondeposition of sediments occurred. Finally, the transition from the nannofossil ooze of Unit II to the volcanic silt of Unit I will document the approach of the ridge to the arc.

A preliminary tectonic analysis of faults observed in the upper part of Hole 828B suggests a set of conjugate normal faults. These faults cut through the northeast flank of the ridge and may be induced by bending of the plate before subduction.

Nannofossils and planktonic foraminifers were the best source of age information. The sedimentary samples in Hole 828A (based on core-catcher samples only) ranged in age from late Pleistocene to middle Eocene.

Magnetic measurements of samples from Hole 828A gave clear evidence of several magnetic polarity reversals. Sediments in the first 61.4 mbsf were deposited during the Brunhes Chron (i.e., age less than 0.7 Ma). A detailed polarity reversal sequence is recorded from 70.9 to 89.9 mbsf and correlates very well with the biostratigraphic units.

Initial results of fluid analyses indicate that chloride concentrations exhibit a broad distinct maximum, reaching values of 570 mM (approximately 2% higher than seawater) at 50 mbsf. Samples from Site 827 were characterized by high chloride concentrations; thus the chloride maximum observed at Site 828 may represent water that flowed out of the wedge. Calcium and magnesium concentrations are similar to the values measured at Site 827 as well. The solute concentrations can also be explained, however, by diffusion upward from reaction zones in the basement rocks and thus are not proof that the water has flowed from the wedge. Nutrient data (alkalinity, ammonia, and phosphate) show only minor amounts of organic matter oxidation, which suggests that there is little (perhaps 0.5%) organic carbon in the sediment. Due to hole collapse, logging was not undertaken.

The most notable changes of physical properties at Site 828 are the increase in porosity and water content and the decrease in bulk density in lithostratigraphic Unit I (0–57.7 mbsf in Hole 828A). This unit and lithostratigraphic Unit I (0–86.0 mbsf in Hole 827A) at Site 827 comprise similar lithologies (dark greenish gray unlithified volcanic silt with interbeds of very dark gray, normally graded beds of sandy volcanic silt) and can therefore be correlated to each other. Porosity and water content increase in lithostratigraphic Unit I at Site 828, whereas general decrease occurs at Site 827. At about 58 mbsf, porosity is about 10% higher at Site 828 than at Site 827, water content is about 20% higher, and bulk density is 0.3 mg/m^3 lower. Also, the measured shear strength values at Site 828 are generally lower than at Site 827 and do not show the same strong and continuous increase with depth, which suggests that the sediments at Site 828 generally are less disturbed than at Site 827.

BACKGROUND AND OBJECTIVES

Site 828 is the second of a series of sites (Sites 827–831) within the collision area of the d'Entrecasteaux Zone (DEZ). It is located on the northern flank of the North d'Entrecasteaux Ridge (NDR), about 2 km west of the trace of the New Hebrides subduction zone and about 40 km from the western shore of Espiritu Santo Island in the central New Hebrides Island Arc (Fig. 1). Our primary objective was to drill through the sediment cover of the ridge to recover basement rocks that could be used to date the ridge and to compare with rocks that may be recovered from beneath the décollement at Site 829.

The NDR is the northern ridge of the DEZ, a two-ridge system that also includes the South d'Entrecasteaux Chain (SDC). The DEZ is a fairly continuous system that is elevated 2 to 4 km above the seafloor, is over 100 km wide, and extends for over 600 km from New Caledonia to Vanuatu where it is in active collision with the central New Hebrides Island Arc (see "Introduction" chapter, this volume; Fig. 2). The DEZ is believed to be the northern arcuate extension of a northeast-dipping Eocene subduction/obduction system, parts of which are exposed on New Caledonia (Daniel et al., 1977; Maillet et al., 1983). Seafloor sampling along the DEZ west of 166°00'E (Maillet et al., 1983) and drilling in the North Loyalty Basin (Shipboard Scientific Party, 1975) approximately 75 km southeast of Sabine Bank of the SDC has yielded data from which the tectonic development and history of the DEZ are speculated. Dredge samples taken along the DEZ indicate that basement rocks of the NDR are similar to mid-ocean ridge basalts (MORB) (Maillet et al., 1983); fission-track ages of these rocks ranged from 56 Ma to 36 Ma (Eocene to Oligocene). Maillet et al. (1983) propose that the morphology of the DEZ originated from extensional horst-and-graben tectonics, resulting in uplift and exposure of ocean-floor basement rocks.

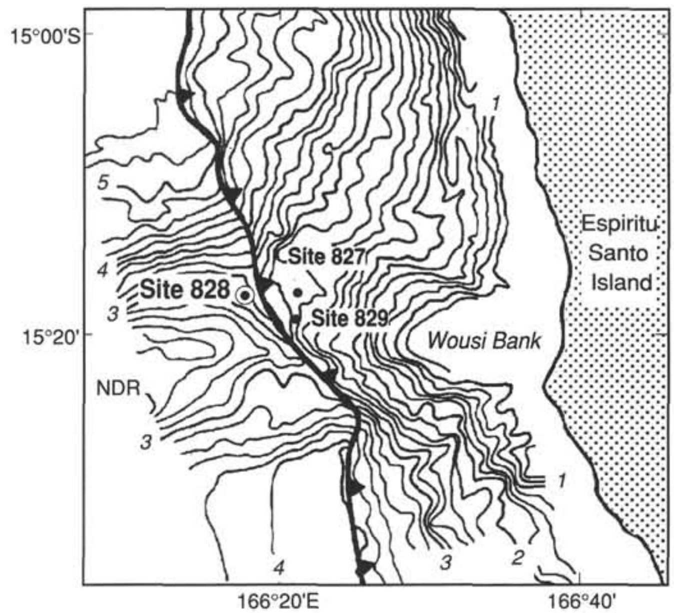

Figure 1. Bathymetric map of the d'Entrecasteaux collision zone offshore of Espiritu Santo Island, central New Hebrides Island Arc, Vanuatu (modified after Collot et al., 1989). The location of Site 828 (circled dot) is shown in relation to Sites 827 and 829. Heavy line indicates trace of subduction zone, teeth are on the upper plate. NDR = North d'Entrecasteaux Ridge. Bathymetry in kilometers; contour interval is 200 m.

Luyendyk et al. (1974) suggested that the DEZ was a fracture zone. Collot et al. (1985) concluded that the eastern DEZ may be a pre-Miocene south-dipping subduction zone. Burne et al. (1988), whose data support the hypotheses of Maillet et al. (1983) that the NDR consists of at least 37-Ma ocean floor uplifted during the middle Miocene, suggest that the SDC represents the remnants of an Eocene proto-island arc formed contemporaneously with subduction along the northern margin of the DEZ. This interpretation is supported by rocks dredged from Bougainville Guyot on the SDC that are of island-arc affinity (Collot et al., unpubl. data).[3]

[3] Collot, J.-Y., Lallemand, S., Pelletier, B., Eissen, J.-P., Glaçon, G., Fisher, M. A., Greene, H. G., Boulin, J., Daniel, J., and Monzier, M. Geology of the d'Entrecasteaux–New Hebrides island arc collision: results from a deep-sea submersible survey (submitted to *Tectonophysics*).

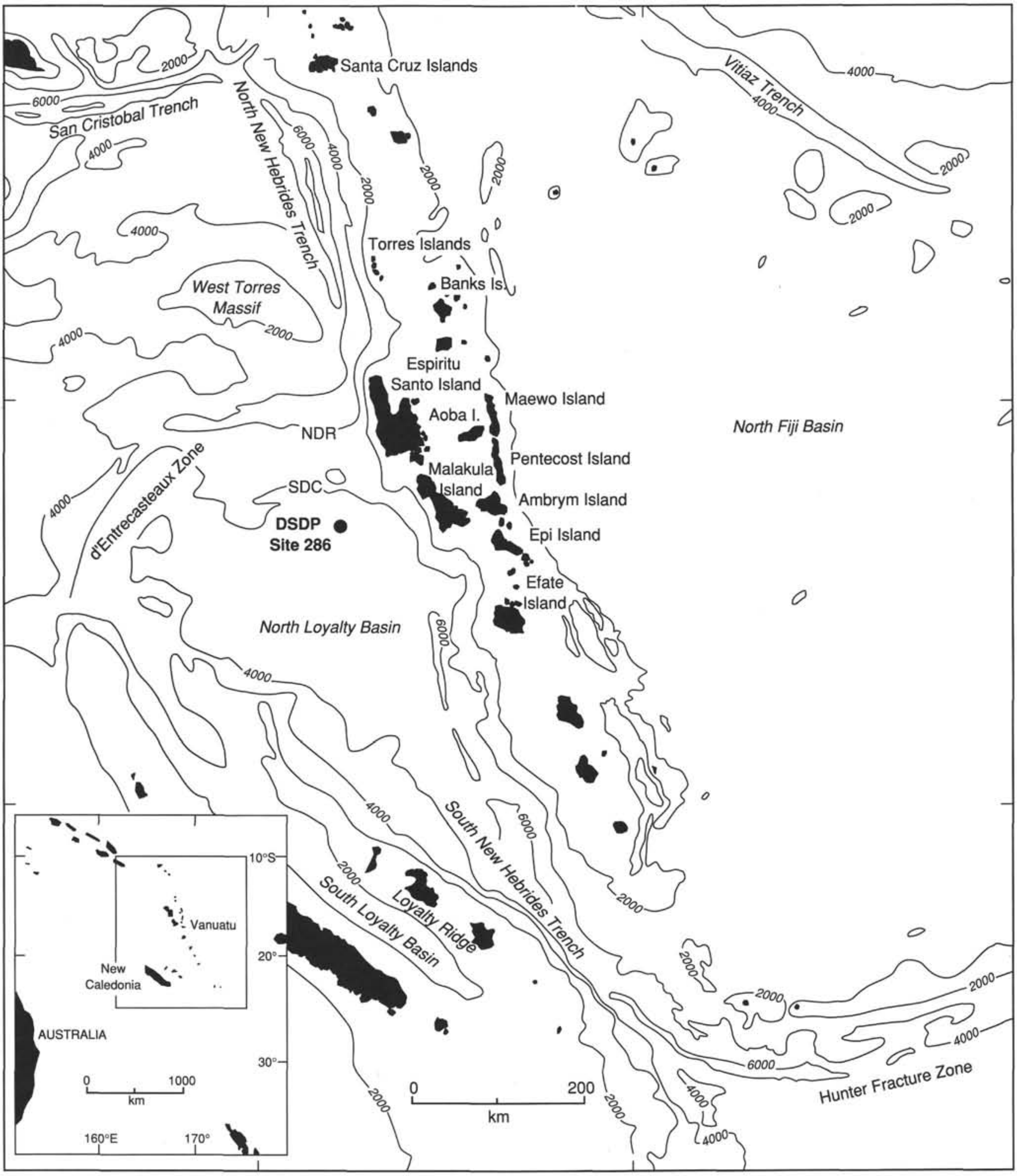

Figure 2. Generalized bathymetric map of the New Hebrides Island Arc and d'Entrecasteaux Zone (modified after Kroenke et al., 1983). NDR = North d'Entrecasteaux Ridge; SDC = South d'Entrecasteaux Chain. Bathymetry in meters.

The DEZ is a tectonically derived feature much older than the presently active New Hebrides Island Arc and has existed long enough to accumulate a sedimentary record that could chronicle geologic events associated with the possible reversal of New Hebrides subduction polarity and the initiation of ridge-arc collision. Seismic reflection profiles collected across the DEZ indicate that a 100- to 200-m blanket of sediment covers the NDR and that hard, layered carbonate rocks cover the guyots of the SDC (Fisher, 1986; Burne et al., 1988; Fisher et al., 1991; Collot et al., 1989). It is possible that the difference in the morphology, sedimentary cover, and basement rock composition of the two ridges deforms the forearc slope differently where these ridges are impinging upon the arc. The NDR is being subducted beneath the arc with relatively little disturbance of the arc-slope rocks compared to the SDC, which largely deforms the arc-slope rocks (Fisher et al., 1986). Thus, our scientific objectives were as follows:

1. To determine sediment and basement lithology of the NDR for comparison with samples recovered from above and beneath the décollement at Site 829; this will be used to assist in the identification of the décollement.
2. To determine through the evaluation of lithostratigraphy, biostratigraphy, paleomagnetism, and radiometric age determination of cored samples the time and place of origin of the ridge; this will help to document the northward absolute movement of the Australia-India plate and the initiation of the collisional processes.
3. To determine the timing, longevity, and location of volcanic eruptions through the study of ash chemistry and chronology; this will help to document the time of island building for both the New Hebrides Island Arc and the SDC.
4. To determine when the eastern part of the NDR came under the sedimentary influence of the New Hebrides Island Arc by studying the mineralogy and paleontology of the Neogene sedimentary rocks; this will help to refine regional plate motion and formation of the New Hebrides Island Arc.

SEISMIC STRATIGRAPHY

Multichannel Seismic Data

Site 828 is located on the North d'Entrecasteaux Ridge. Multichannel seismic reflection data and results of dredging indicate that this ridge is covered by a thin (about 100–200 m) sediment layer. This layer is presumed to overlie igneous oceanic crust because Eocene MORB was dredged from the flanks of the ridge 200 km west of the New Hebrides Island Arc (Maillet et al., 1983). Multichannel seismic data (Figs. 3 and 4) show reflections from the thin sediment cap and poor reflections from the underlying basement. Drilling has verified that the sediment layers include pelagic and hemipelagic debris collected as the ridge moved toward the island arc. Although the multichannel seismic line shown in Figure 4 shows only poor basement reflections, elsewhere along the ridge reflections from within the presumed igneous basement

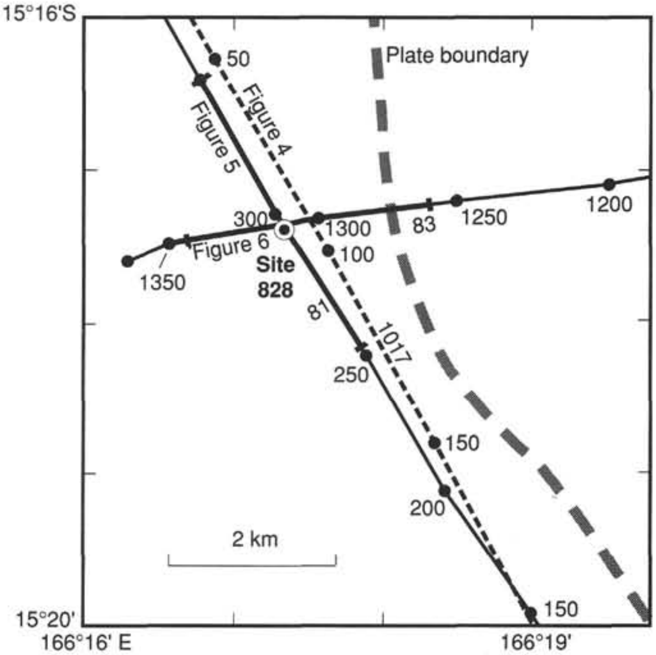

Figure 3. Trackline map showing the locations of Site 828, single-channel seismic lines 81 and 83, and multichannel seismic line 1017 (Multipso cruise).

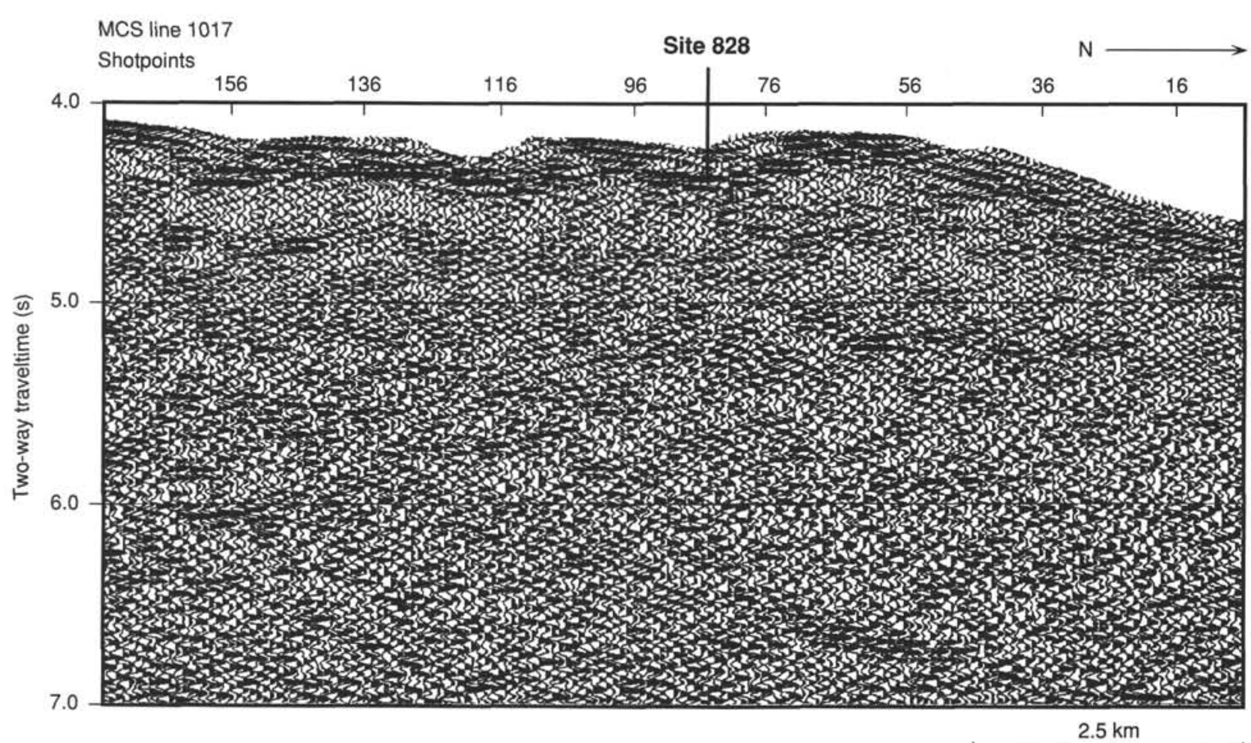

Figure 4. Part of migrated multichannel seismic (MCS) line 1017 (Multipso cruise).

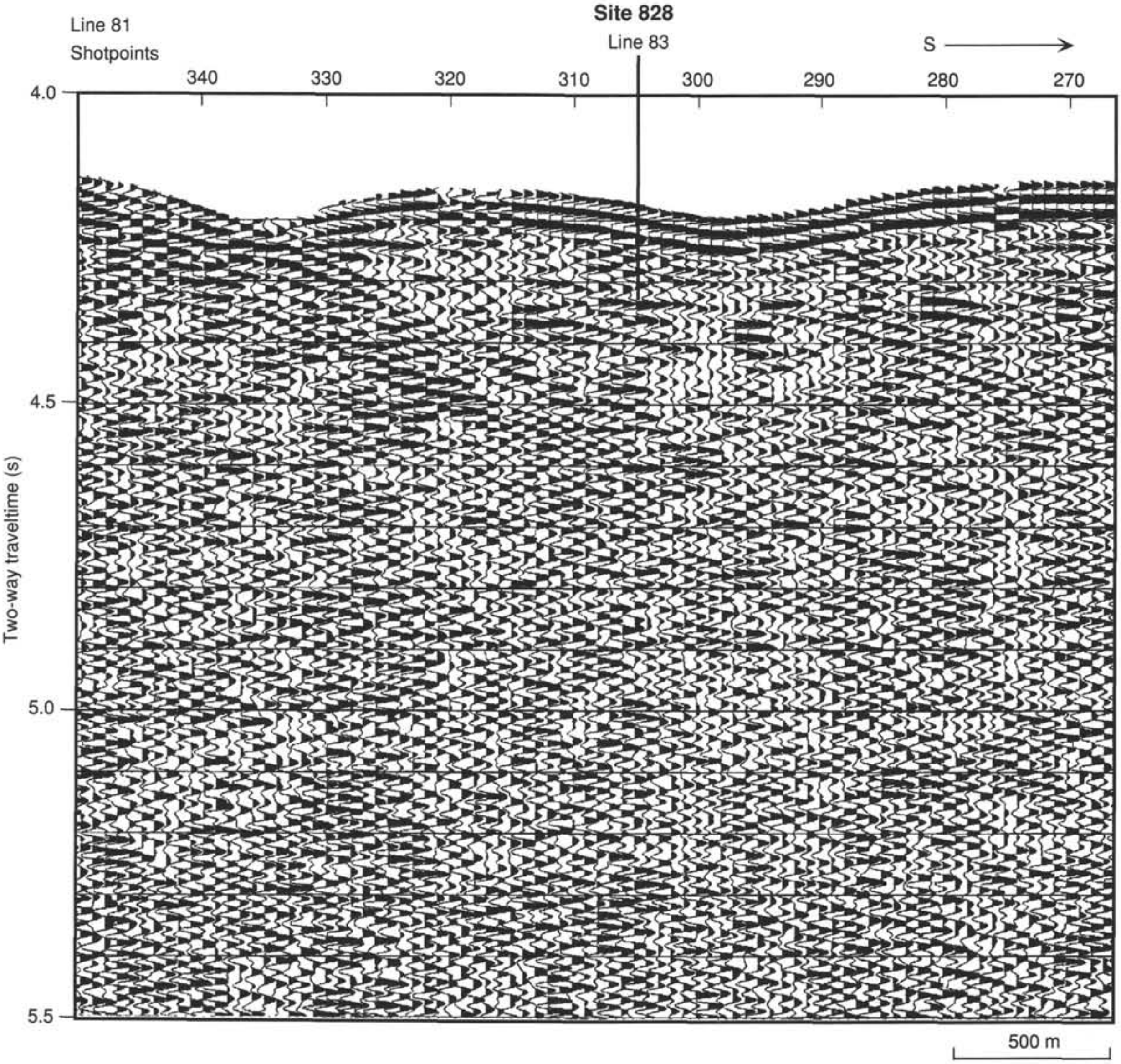

Figure 5. Part of single-channel seismic line 81.

are more continuous and have variable east and west apparent dips. These reflections indicate that some intrabasement interfaces extend to depths as great as 6 km.

Single-Channel Seismic Data

To aid final placement of Site 828, we obtained single-channel seismic reflection data over this site, using two 80-in.^{3} water guns for the source and a streamer that has a 100-m-long active section. These data were processed aboard the ship using SIOSEIS software running on a Masscomp computer. The processing steps included predictive deconvolution, bandpass filtering, and automatic gain control.

Vertical velocity data from physical properties measurements ("Physical Properties" section, this chapter) indicate that the acoustic velocity of rocks within the upper 98 m of penetrated rock averaged 1600 m/s. No well-log information were obtained to give a more complete indication of velocity variation. Thus, the sub-seafloor traveltime to the bottom of the hole at 129 mbsf is 0.161 s (Figs. 5 and 6).

Single-channel seismic lines 81 and 83 (Figs. 3, 5, and 6) cross near Site 828. Both seismic sections indicate that the sub-seafloor traveltime to the bottom of the hole (0.161 s) is just at or below the onset of the reflection from the presumed igneous basement. Of the two seismic lines, line 83 (Fig. 6) shows the more continuous basement reflection, and the traveltime to the hole bottom lies below the basement top. Thus, fragments of hard rocks from the lowest cores obtained at this site are probably basement samples. Neither seismic line reveals much of the varied stratigraphy encountered in the hole.

OPERATIONS

Hole 828A

The drillship moved in dynamic positioning mode from Site 827 to the location of the beacon dropped earlier on proposed site DEZ-1. The precision depth recorder (PDR) indicated a drilling depth of about 3125 meters below sea level (mbsl), but again the reading proved too deep. Seafloor depth finally was established at 3086.7 mbsl after a full-barrel misrun with the advanced piston coring (APC) system.

APC cores were taken with excellent results through volcanic silt, calcareous ooze, and foraminiferal sand to 95

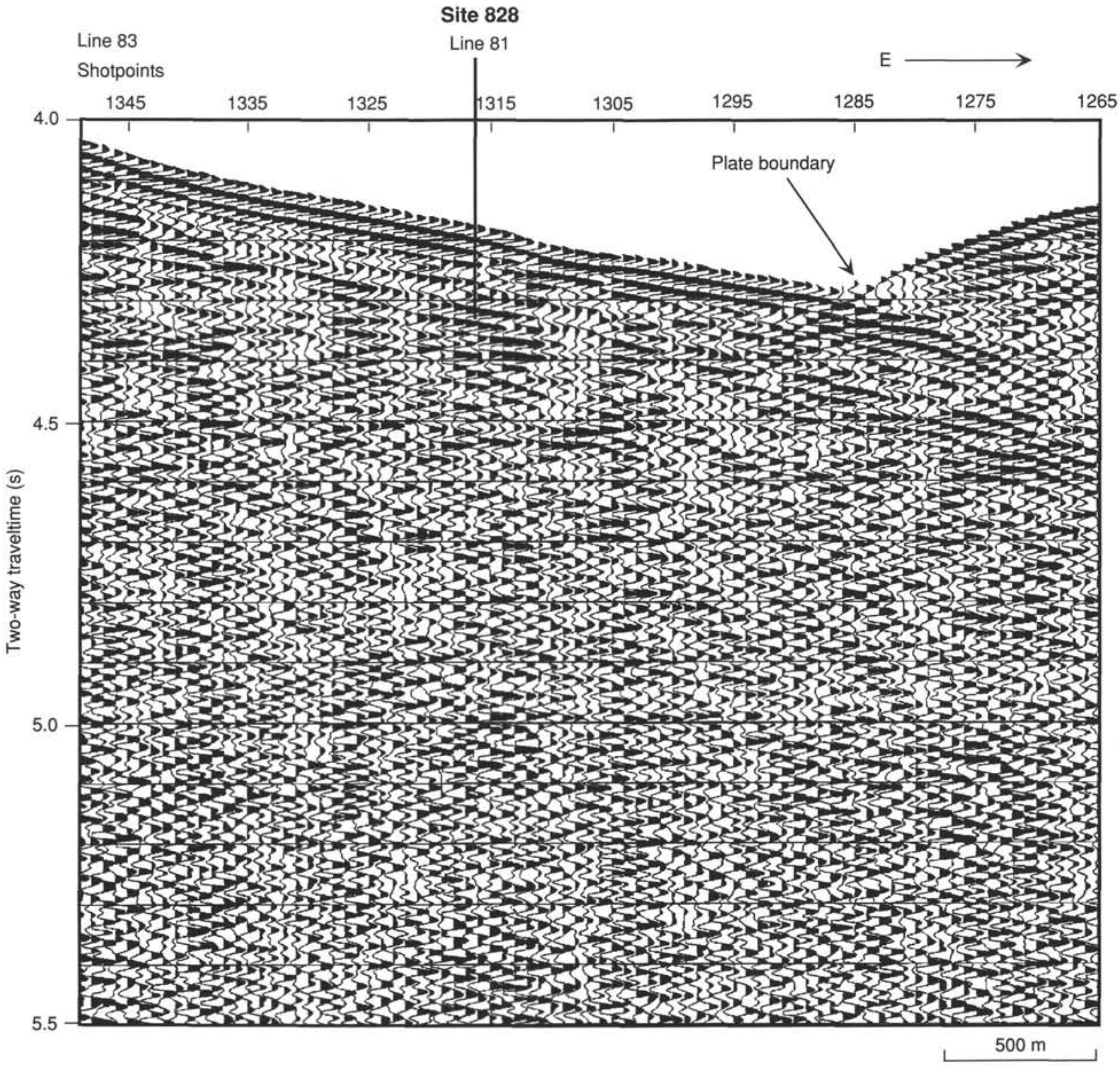

Figure 6. Part of single-channel seismic line 83.

mbsf, where hard rocks abruptly stopped the APC. Core orientation was only partially successful because of instrument problems.

Two extended core barrel (XCB) cores were attempted but recovered less than 1 m of brecciated volcanic rock. Further drilling was beyond the capabilities of the XCB system and the polycrystalline diamond compact drag-type drill bit used with it, so the motor-driven core barrel system was employed to recover over 2 m of extremely rubbly material.

Hole problems began as the final core was being retrieved. The drill string became stuck for several minutes as the pipe trip began but eventually was freed and recovered without incident. Total penetration was 111.4 m and core recovery averaged 91% (Table 1).

Hole 828B

The second attempt to reach basement used the rotary core barrel (RCB) system. The ship was offset 214 m to the northwest in an effort to avoid the unstable and rubbly unit encountered in Hole 828A.

The hole was washed to 90 mbsf and continuous RCB coring began. The first core recovered sediments but the following two cores contained only pebbles of volcanic rock. The hole became unstable, and a fourth core was attempted after trying to stabilize the hole. The pipe became stuck when the bit was lifted off the bottom of the hole. The pipe was freed after 45 min of working and jarring. The hole was judged to be undrillable and the final core barrel was recovered with the drill string. Total penetration was 129 m and core recovery averaged 20% (Table 1).

LITHOSTRATIGRAPHY

Sedimentary Units

Lithostratigraphic analyses of the 109.3 m of sedimentary and igneous rocks recovered from Holes 828A and 828B, drilled to depths of 111.4 and 129.0 m, respectively, indicate that the sequence is best divided into four major units (Table 2 and Fig. 7). Lithologic divisions proposed herein compare well with physical properties and biostratigraphic data at Hole 828 (see "Biostratigraphy" and "Physical Properties" sections, this chapter).

Table 1. Coring summary, Holes 828A and 828B.

Core	Date (1990)	Time (UTC)	Depth (mbsf)	Length cored (m)	Length recovered (m)	Recovery (%)	Age
134-828A-							
1H	25 October	1945	0.0–4.4	4.4	4.36	99.1	Pleistocene
2H	25 October	2110	4.4–13.9	9.5	9.95	105.0	Pleistocene
3H	25 October	2200	13.9–23.4	9.5	9.98	105.0	Pleistocene
4H	25 October	2245	23.4–32.9	9.5	9.73	102.0	Pleistocene
5H	25 October	2330	32.9–42.4	9.5	9.95	105.0	Pleistocene
6H	26 October	0030	42.4–51.9	9.5	9.87	104.0	Pleistocene
7H	26 October	0115	51.9–61.4	9.5	9.58	101.0	Pleistocene
8H	26 October	0200	61.4–70.9	9.5	9.73	102.0	Oligocene
9H	26 October	0245	70.9–80.4	9.5	10.05	105.8	Oligocene
10H	26 October	0330	80.4–89.9	9.5	9.84	103.0	Oligocene
11H	26 October	0515	89.9–95.4	5.5	5.49	99.8	?Eocene
12X	26 October	0645	95.4–97.4	2.0	0.36	18.0	—
13X	26 October	0850	97.4–106.8	9.4	0.36	3.8	—
14N	26 October	1100	106.8–107.8	1.0	0.24	24.0	—
15N	26 October	1400	107.8–111.4	3.6	1.85	51.4	—
Coring totals				111.4	101.34	91.0	
134-828B-							
1R	27 October	0630	90.0–100.0	10.0	7.76	77.6	Eocene
2R	27 October	0805	100.0–109.7	9.7	0.07	0.7	
3R	27 October	0950	109.7–119.4	9.7	0.09	0.9	
4R	27 October	1840	119.4–129.0	9.6	0.00	0.0	
Coring totals				39.0	7.92	20.3	

Note: Dashes indicate indeterminate age.

Hole 828A

Unit I

Depth: 0–58.7 mbsf
Interval: Sections 134-828A-1H-1, 0 cm, to 134-828A-7H-5, 83 cm
Thickness: 58.7 m
Age: Pleistocene

Unit I is composed of a Pleistocene sequence of dark greenish gray (10Y 3/1 to 4/1), unlithified volcanic silt with interbeds of very dark gray (5Y 3/1), normally graded, sandy volcanic silt with foraminifers. Many interbeds have scoured bases. Bioturbation has effectively mixed the uppermost sediments of these interbeds into the overlying volcanic silt creating a smeared effect (Fig. 8). The percentage of clay tends to increase with increasing depth within the unit, making up 30%–50% of the sediment below. Carbonate content is approximately 10% from 0 to 45 m, but increases to as much as 25% near the base of the unit (Fig. 9). The contact between Unit I and Unit II is marked by a dark brown (2.5Y 5/2) bioturbated ash layer.

Unit II

Depth: 58.7–69.3 mbsf
Interval: Sections 134-828A-7H-5, 83 cm, to 134-828A-8H-6, 42 cm
Thickness: 10.6 m
Age: Pleistocene and early Pliocene or late Miocene

Unit II consists of dark brown to very pale brown to white (10YR 8/3 to 10YR 7/4–8/2), totally unconsolidated forami-

Table 2. Lithostratigraphic units, Hole 828A.

Interval	Unit	Subunit	Depth (mbsf)	Thickness (m)	Age
Sections 134-828A-1H-1, 0 cm, to -7H-5, 83 cm	I		0–58.7	58.7	Pleistocene
Sections 134-828A-7H-5, 83 cm, to -8H-6, 42 cm	II		58.7–69.3	10.6	Pleistocene and early Pliocene/late Miocene
Sections 134-828A-7H-5, 83 cm, to -8H-1, 48 cm		IIA	58.7–61.9	3.2	Pleistocene
		Possible unconformity			
Sections 134-828A-8H-1, 48 cm, to -8H-6, 42 cm		IIB	61.9–69.3	7.4	early Pliocene/ late miocene
		Unconformity			
Sections 134-828A-8H-6, 42 cm, to -11H-1, 92 cm	III		69.3–90.8	21.5	late to middle Oligocene
Sections 134-828B-1R-1, 0 cm, to -2R-1, 0 cm	III		90.0–100.0	10.0	earliest Oligocene/ latest Eocene
		Possible unconformity			
Sections 134-828A-11H-1, 92 cm, to -15N-2, 228 cm	IV		90.8–111.4	20.6	middle Eocene (?) (core catcher only)
Sections 134-828B-2R-1, 0 cm, to -3R-1, 12 cm	IV		100.0–119.4	19.4	Unknown (barren)

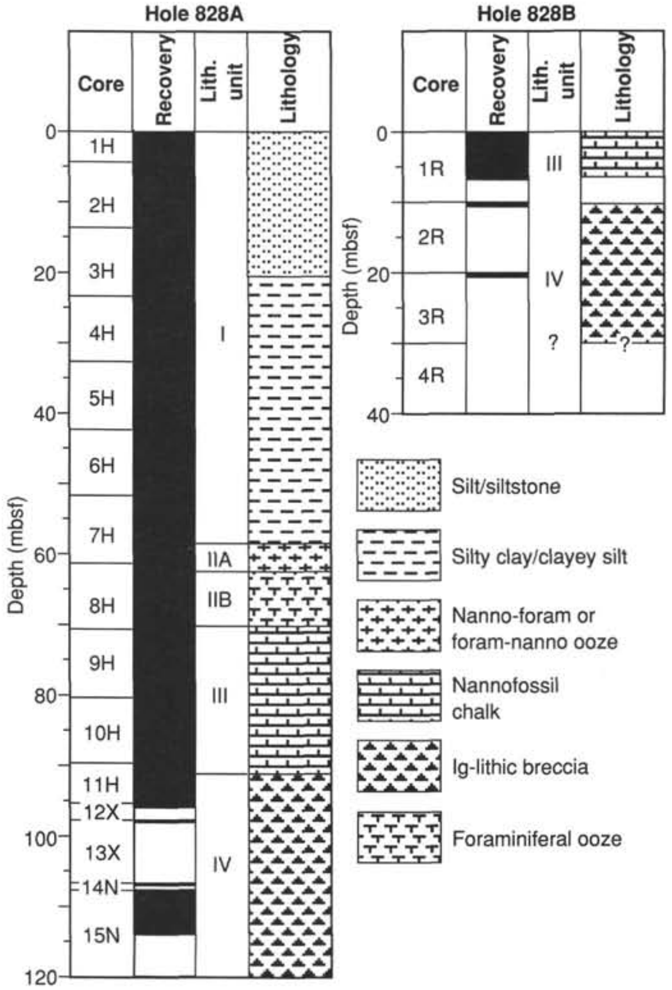

Figure 7. Diagram depicting the four major lithostratigraphic units of Holes 828A and 828B.

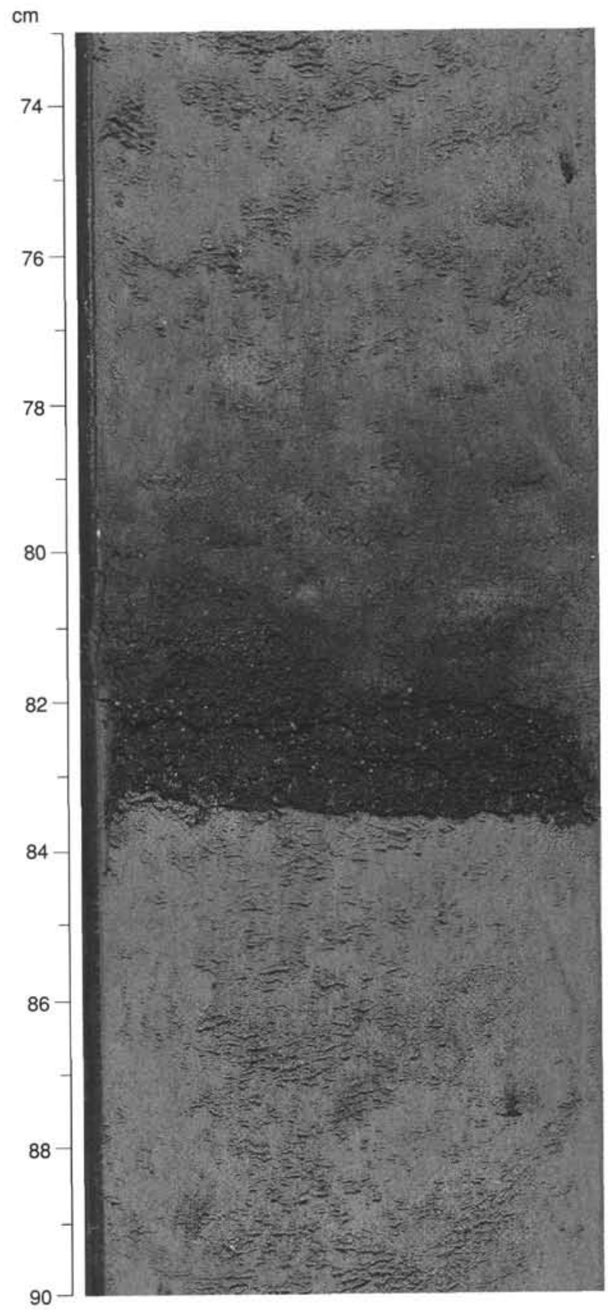

Figure 8. Photograph of interval 134-828A-7H-5, 73–90 cm, showing ash layer with sharp basal contact and smeared, bioturbated upper surface.

niferal ooze with nannofossils. Unit II is subdivided into two subunits based on the occurrence of volcanogenic minerals: volcanic components are minor portion of the sediments of Subunit IIA and are absent in Subunit IIB (Fig. 9). The contact between Unit II and Unit III is marked by an abrupt increase in lithification and bioturbation, as well as a reversal in the proportion of foraminifers to nannofossils.

Subunit IIA

Depth: 58.7–61.9 mbsf
Interval: Sections 134-828A-7H-5, 83 cm, to 134-828A-8H-1, 48 cm
Thickness: 3.2 m
Age: Pleistocene

Subunit IIA consists of light brownish gray to very pale brown (2.5Y 5/4 to 10YR 7/4) foraminiferal ooze with nannofossil and volcanic silt. Pumice clasts up to 2 cm in diameter, volcanic gravel horizons, and dark brown (2.5Y 5/2) ash layers, 1–4 cm thick, are sporadically distributed (Fig. 10). The proportion of volcanic components varies through the unit: silt and ashy layers alternate with firm-to-soupy beds of nearly pure foraminiferal sand (Fig. 11).

Subunit IIB

Depth: 61.9–69.3 mbsf
Interval: Sections 134-828A-8H-1, 48 cm, to 134-828A-8H-6, 42 cm
Thickness: 7.4 m
Age: early Pliocene or late Miocene

Subunit IIB consists of very pale brown to white (10YR 7/4 to 8/2) unconsolidated foraminiferal ooze. It is separated from Subunit IIA by a sharp color change where the volcanic component of the sediment ends (Fig. 10). The abundance of unconsolidated foraminifers results in a sediment texture that is reminiscent of beach sands.

Unit III

Depth: 69.3–90.8 mbsf
Interval: Sections 134-828A-8H-6, 42 cm, to 134-828A-11H-1, 92 cm
Thickness: 21.5 m
Age: early to late Oligocene

Unit III predominantly consists of highly bioturbated, light yellowish brown (10YR 6/4) nannofossil chalk. Isolated sub-

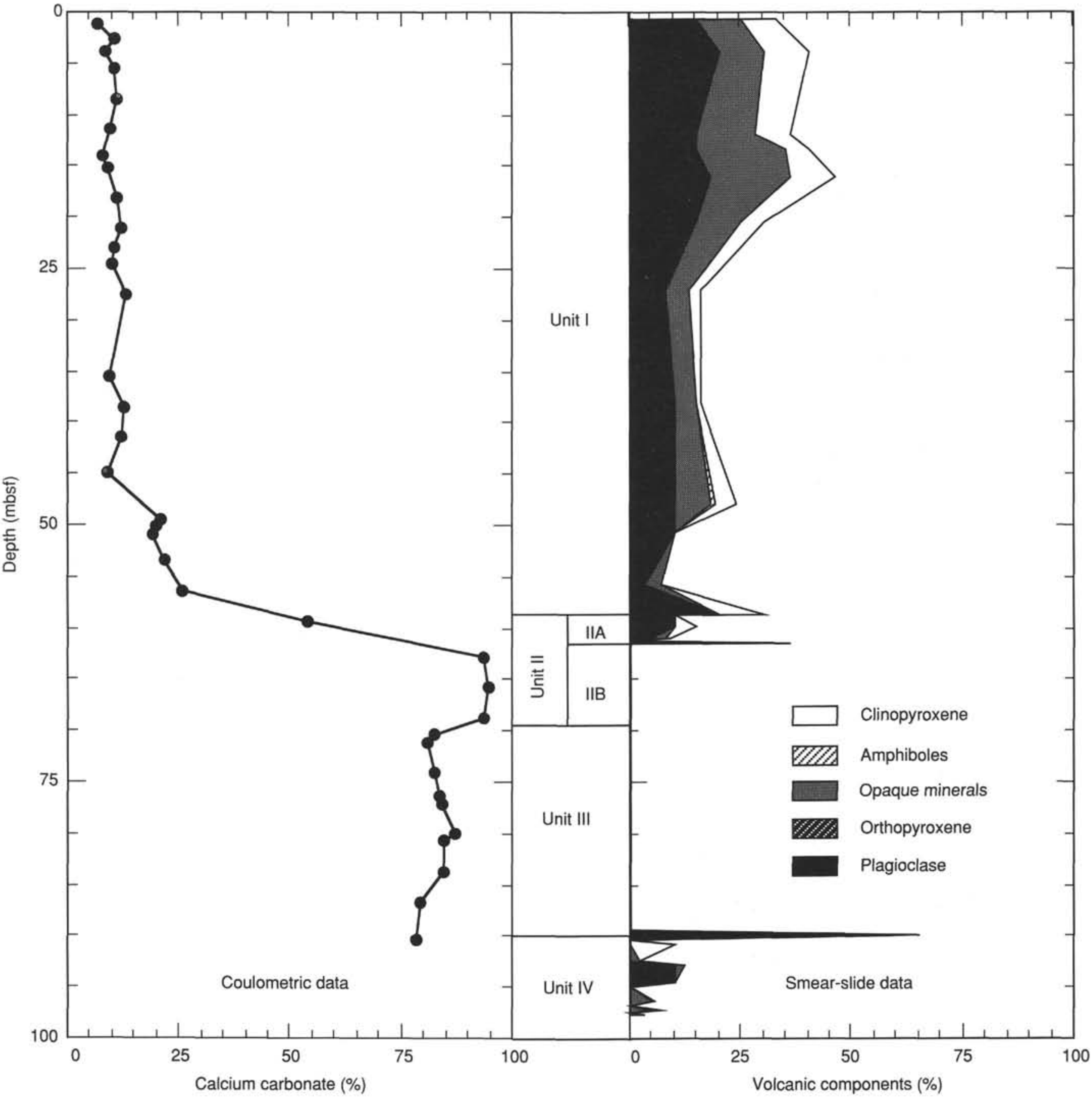

Figure 9. Percentage of calcium carbonate and constituent volcanogenic minerals plotted vs. depth at Hole 828A. The four major lithostratigraphic units have distinctive assemblages of these mineral suites.

rounded to rounded clasts of highly altered volcanic rock and beds of zeolitic silty sand occur, and several manganese nodules are found near the top of the unit. The abrupt contact between Units II and III (Fig. 12) coincides with a biostratigraphic hiatus, which indicates that most of the Miocene is missing across this boundary.

Unit IV

Depth: 90.8–111.4 mbsf
Interval: Sections 134-828A-11H-1, 92 cm, to 134-828A-15N-2, 185 cm
Thickness: 20.6 m
Age: *middle Eocene(?)*

Unit IV consists of ig-lithic breccia, brecciated lava flow deposits, and brecciated aphyric basalt/diabase. The ig-lithic breccia consists of matrix-supported, angular to subrounded, greenish gray (10Y 4/1) and dusky red (10R 3/3) clasts of volcanic rocks ranging in size from 2 to 5 cm. Chert may be present as rare light greenish gray clasts. The breccia matrix is pale olive green (5Y 6/4) and dusky red (10R 3/3), silty to clayey sand, with a trace amount of nannofossils. Green and red matrixes are intermixed. Further discussion

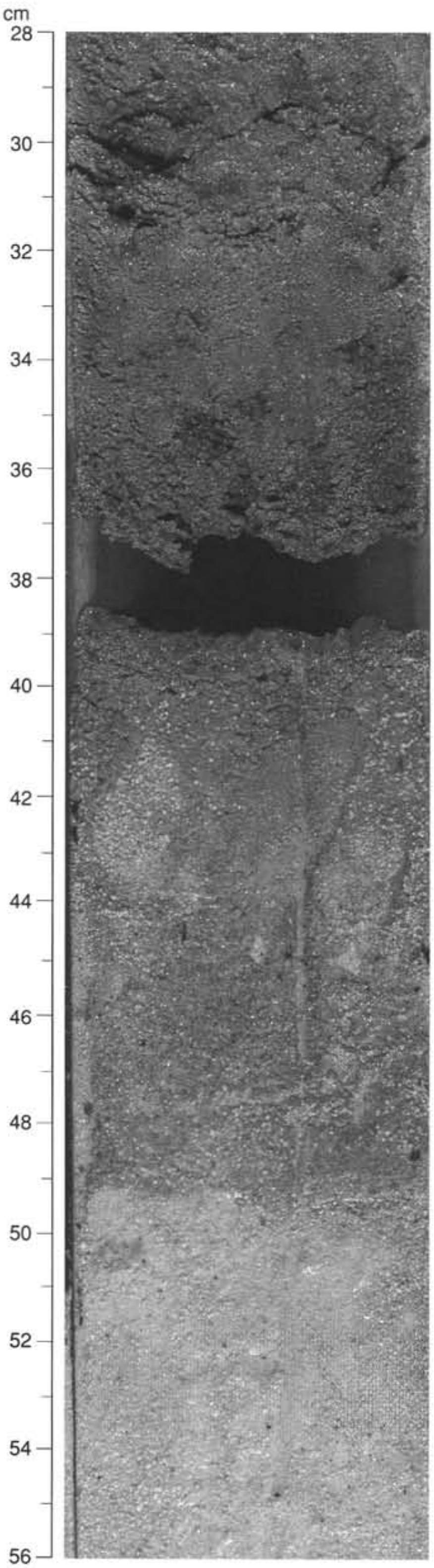

Figure 10. Photograph of interval 134-828A-8H-1, 28–56 cm, showing contact between Subunit IIA and IIB (48 cm). Unit IIB consists of white, pure foraminiferal sand. Volcanic gravel layer is located at and above the fissure (29–39 cm).

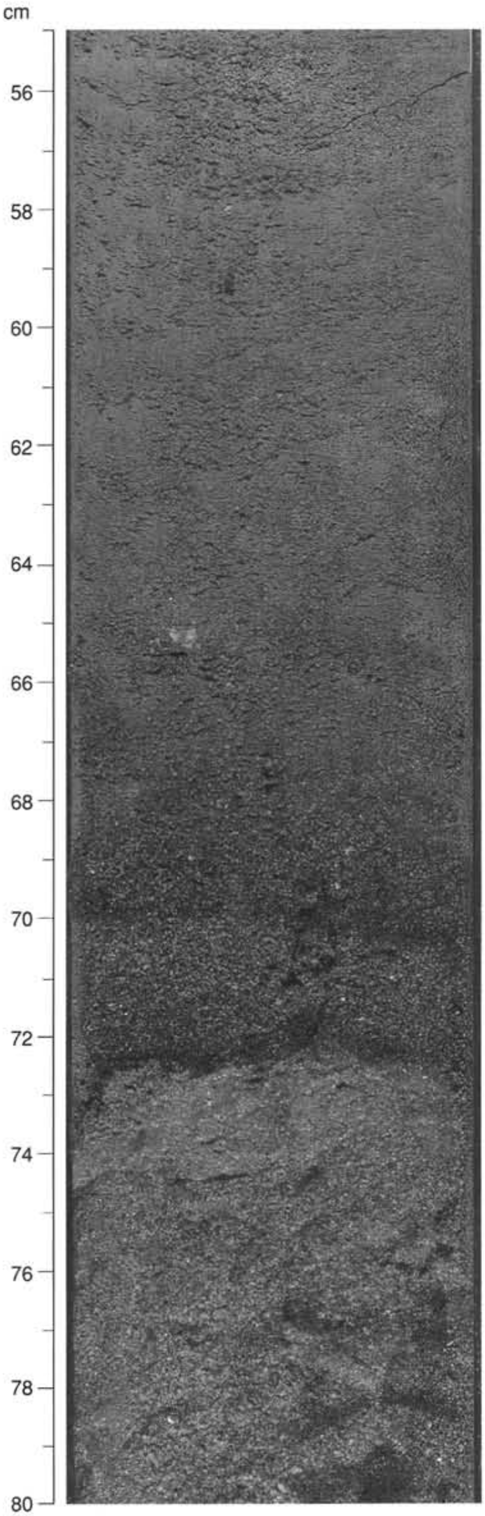

Figure 11. Photograph of interval 134-828A-7H-6, 55–80 cm, showing two ash layers (69.5–72.5 cm), overlain by silty foraminiferal sand and underlain by foraminiferal sand.

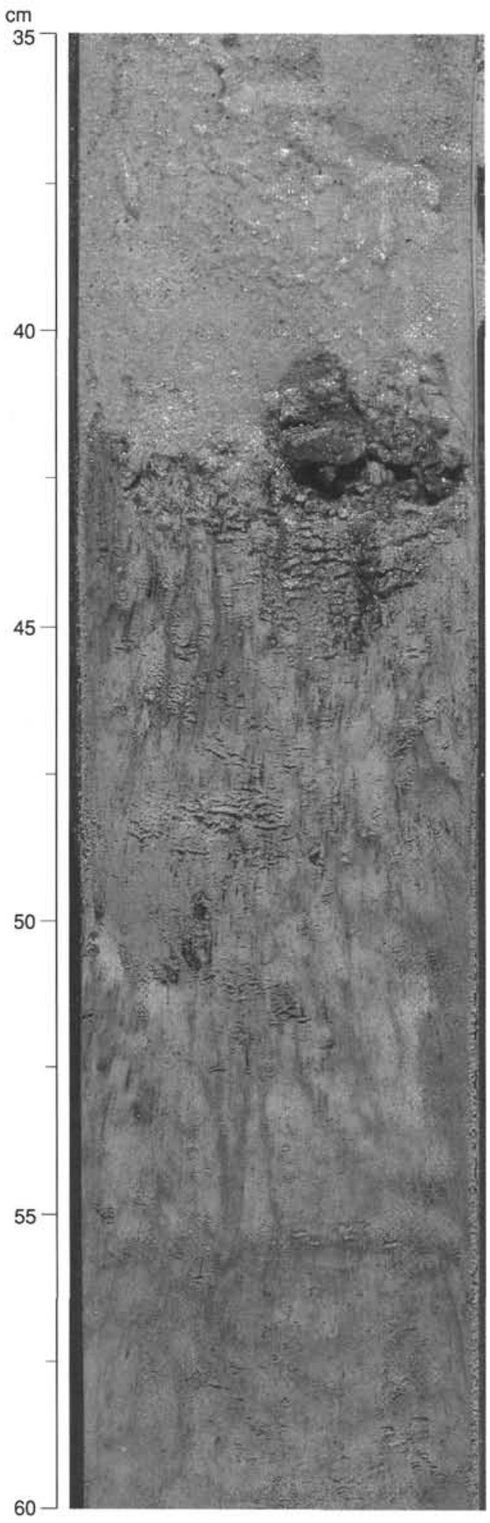

Figure 12. Photograph of interval 134-828A-8H-6, 35–60 cm, showing contact between Units II and III (42 cm). Unit II is unconsolidated foraminiferal ooze; Unit III is partially consolidated nannofossil chalk.

of the unit can be found in the "Igneous Petrology" section (this chapter).

Hole 828B

Lithostratigraphic analyses of sedimentary and igneous rocks recovered from Hole 828B indicate that the sequence is best divided into two major units that are correlative with Units III and IV of Hole 828A (Table 2 and Fig. 7).

Unit III

Depth: 90.0–100.0 mbsf
Interval: Sections 134-828B-1R-1, 0 cm, to 134-828B-2R-1, 0 cm
Thickness: 10.0 m
Age: earliest Oligocene or latest Eocene

We group the nannofossil chalks in the upper 7.15 m of Hole 828B into Unit III, as the sediments are similar to those in Hole 828A at 69.3–90.8 mbsf. Unit III comprises highly mottled, light gray to light brownish gray (10YR 7/2 to 6/2) nannofossil chalk with about 15% foraminifers. The lowermost 50 cm consist of a dark brown (7.5Y 5/3) volcanic silt with nannofossils that grade downward into a nannofossil-foraminiferal, silty, sandy mixed sediment. This interval also contains abundant dewatering structures (Fig. 13). Pumice fragments up to 3 cm in diameter are distributed sporadically throughout the chalk and silt intervals.

Unit IV

Depth: 100.0–119.4 mbsf
Interval: Sections 134-828B-2R-1, 0 cm, to 134-828B-4R-1, 0 cm
Thickness: 19.4 m
Age: Unknown (barren)

Unit IV in Hole 828B consists of brecciated aphyric basalt/diabase similar to that in Hole 828A (see "Igneous Petrology" section, this chapter).

BIOSTRATIGRAPHY

Pelagic microfossils from samples obtained at Site 828 indicate ages of Pleistocene to late Eocene. A disconformity at which the upper Pliocene to lower Pleistocene is missing is indicated by nannofossils, but not by foraminifers. A second prominent disconformity at which most, if not all, of the Miocene and the uppermost Oligocene is missing is supported by strong agreement between nannofossil and foraminiferal datums. Below this second disconformity, Oligocene and Eocene sediments represent apparently continuous deposition. Near the bottom of Holes 828A and 828B, biostratigraphic interpretation is hindered by the nonpelagic nature of the sediments.

From the top of Core 134-828A-1H to the base of Section 134-828A-7H-CC, both nannofossil (Zone CN14) and foraminiferal (Zone N22) assemblages indicate that the recovered material is of Pleistocene age. Beginning in Section 134-828A-8H-1, however, the nannofossil and foraminiferal analyses produce conflicting interpretations regarding the presence of a possible hiatus in the upper Pliocene and lower Pleistocene. The juxtaposition of sediments containing the nannofossil *Gephyrocapsa oceanica* (thus dated as middle Pleistocene, Zone CN14) with sediments containing a lower Pliocene or possibly upper Miocene assemblage (that includes *Reticulofenestra pseudoumbilica*) suggests a hiatus. Across the same interval, foraminiferal analysis reveals no anomalous assemblage pattern: upper Pliocene is indicated above the purported hiatus whereas lower Pliocene assemblages are observed below it. Several factors have led us to present a dual interpretation regarding this disagreement:

1. Reworking of significant amounts of Pliocene nannofossils prevents the reliable use of the last occurrence of nannofossil datums that normally distinguish lower Pleistocene from upper Pliocene sediments. In addition, nannofossil workers disagree about the reliability of the identification of the *Gephyrocapsa* group when using light instead of scanning electron microscopy. Thus, since light microscopy was used

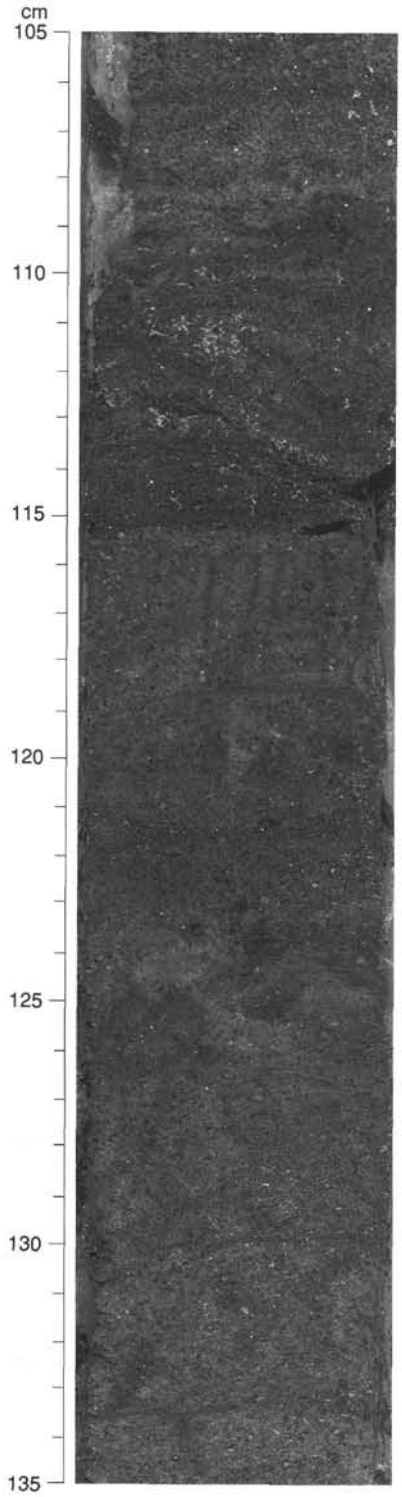

Figure 13. Photograph of interval 134-828B-1R-5, 105–135 cm, showing dewatering structures present at the base of Unit III (e.g., 116 to 120 cm) at Hole 828B.

aboard ship, age determinations based on nannofossils are uncertain in this interval.

2. The foraminiferal interpretation of the position of the Pliocene-Pleistocene boundary relies mainly upon the first occurrence of *Globorotalia truncatulinoides*, a species many researchers would argue is diachronous (Hills and Thierstein, 1989).

Since lithostratigraphical and some paleontological characteristics change abruptly across the supposed disconformity, the differing age interpretations based on nannofossils and foraminifers could have significant implications for tectonic models of the collision of the d'Entrecasteaux Ridge with the New Hebrides Island Arc.

Calcareous Nannofossils

Pleistocene

Samples 134-828A-1H-CC to 134-828A-8H-1, 30–32 cm, contain an assemblage typified by the presence of *Gephyrocapsa oceanica, G. caribbeanica, Helicosphaera kamptneri,* and *Calcidiscus leptoporus* and have thus been placed within Zone CN14 (Fig. 14). The co-occurrence of the age-diagnostic specimens *Discoaster asymmetricus* and *D. pentaradiatus* suggests a moderate degree of reworking of Pliocene nannofossils. Because older and younger floral assemblages in these samples may have been mixed, the last occurrences of the marker species *Pseudoemiliania lacunosa, Calcidiscus macintyrei,* and *Discoaster brouweri* are considered unreliable for age determination.

The Pliocene-Pleistocene boundary cannot be identified without *C. macintyrei* and *D. brouweri*; however, the presence of *G. oceanica* and *G. caribbeanica* in all samples above the disconformity suggests that these sediments are no older than middle Pleistocene. A sharp lithologic contact 50 cm below the top of Section 134-828A-8H-1, separating the Pleistocene from underlying lower Pliocene sediments, represents the disconformity at which the lower Pleistocene and upper Pliocene are missing.

Pliocene

A lower Pliocene floral assemblage, typified by *Discoaster assymetricus, D. pentaradiatus, R. pseudoumbilica,* and *S. abies* (Zone CN11) is recorded in Sample 134-828A-8H-1, 59–61 cm. Samples 134-828A-8H-5, 96–97 cm, and 134-828A-8H-6, 26–27 cm, contain *R. pseudoumbilica, D. asymmetricus, S. abies,* and *Ceratolithus primus*. This assemblage places these samples within the lower Pliocene Zone CN10.

Oligocene

From Sections 134-828A-8H-6 through 134-828A-9H-CC, a typical upper Oligocene assemblage is represented by *Sphenolithus distentus, S. predistentus, Dictycoccites bisectus,* and *Clausicoccolithus fenestrata* (Zone NP23). Beginning in Section 134-828A-10H-CC the presence of *Reticulofenestra umbilica* together with *C. fenestrata, S. predistentus,* and *D. bisectus* represents a change to lower Oligocene Zone NP22. Below this sample, the paucity of nannofossils prevents an age determination.

Eocene

Although an Eocene age for sediments in Hole 828A could not be confirmed using nannofossils, Sample 134-828B-1R-CC contained an Eocene assemblage (Zone NP20) as indicated by the presence of *Discoaster saipanensis* and *D. barbadiensis*; *R. umbilica, E. formosus, D. bisecta,* and *Cyclocargolithus floridanus* were also observed.

Planktonic Foraminifers

Pleistocene to Late Pliocene

Planktonic foraminifers in the uppermost cores of Hole 828A (Cores 134-828A-1H to 134-828A-7H) indicate Pleistocene ages. The common occurrence of *Globorotalia truncatulinoides*, along with an assemblage including *Pulleniatina*

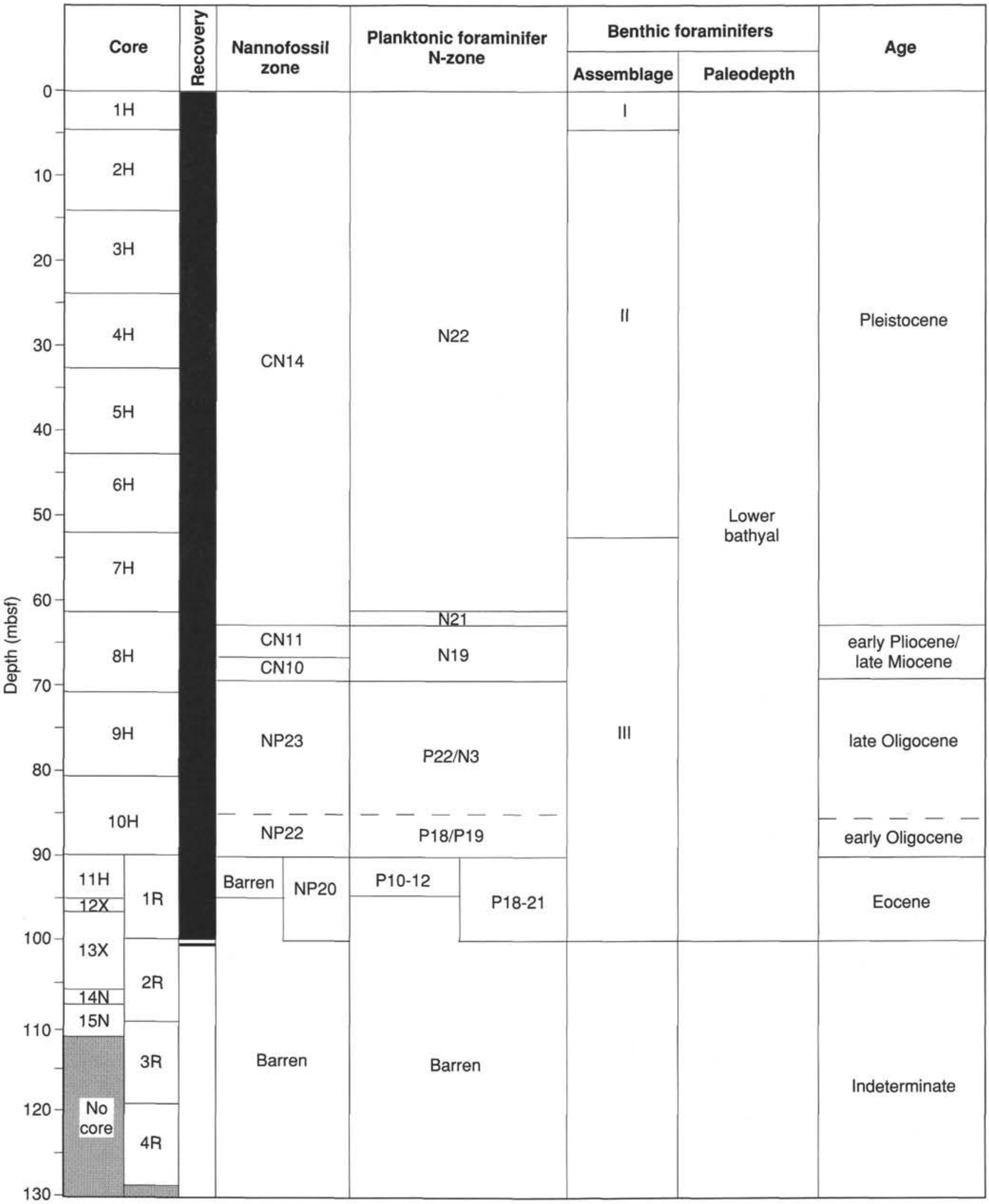

Figure 14. Biostratigraphic summary of Site 828.

obliquiloculata, Globigerinoides sacculifer, Orbulina universa, Sphaeroidinella dehiscens, Globorotalia ungulata, Neogloboquadrina dutertrei, Globorotalia crassaformis, and *Globorotalia menardii,* assigns the cores to the upper part of Zone N22. The presence of *Globorotalia tosaensis* recorded only in Sample 134-828A-7H-CC, suggests an age of early Pleistocene at this depth (61.4 mbsf). Nonetheless, paleomagnetic information for this span shows normal polarity that has been interpreted as the Brunhes Chron (late Pleistocene).

Evidence favoring the presence of the Pliocene-Pleistocene boundary in Core 134-828A-8H results primarily from the foraminiferal assemblage documented in Sample 134-828A-8H-1, 30–32 cm. The absence of *G. truncatulinoides,* coincident with the presence of *Dentoglobigerina altispira, Globorotalia limbata,* and *Globorotalia tosaensis* in this sample, supports a late Pliocene age (Zone N21, cf. Kennett and Srinivasan, 1983) and would thus indicate that the Pliocene-Pleistocene boundary lies between Samples 134-828A-7H-CC and 134-828A-8H-1, 30–32 cm.

Several authors, including Hills and Thierstein (1989), have shown that the first occurrence of *G. truncatulinoides* is unreliable as a chronostratigraphic marker. The presence of *D. altispira* and *G. limbata,* on the other hand, would seem to indicate a Pliocene age, irrespective of the presence of *G. truncatulinoides* in Sample 134-828A-8H, 30–32 cm. The occurrence of *D. altispira* and *G. limbata* could be attributed to reworking.

Pliocene to Latest Miocene(?)

The discrepancies in age determinations outlined above suggest that reworking is a common process at Site 828 (Sample 134-828A-8H-1, 30–32 cm) and may be associated with a major lithologic change at 61.9 mbsf (Sample 134-828A-8H-1, 50 cm). This lithologic change represents the contact between hemipelagic foraminiferal oozes (above) and pelagic foraminiferal oozes (below). Below the lithologic contact, interpreted as an unconformity, a typical lower Pliocene foraminiferal assemblage is observed in Sample 134-828A-8H-2, 69 cm. Common species found in this sample include *G. limbata, Globorotalia multicamerata, D. altispira, Spaeroidinellopsis kochi, Globorotalia tumida flexuosa,* and *Globorotalia juanai* transitional to *Globorotalia margaritae*. Earliest Pliocene (Zone N19) to latest Miocene(?) species are found as deep as Sample 134-828A-8H-5, 119–120 cm (e.g., *G. juanai* transitional to *G. margaritae*).

Oligocene

Below the lowermost Pliocene to uppermost Miocene(?) interval, a second major lithologic change appears at approximately 70 mbsf (Sample 134-828A-8H-6, 70 cm). At this depth, lower Pliocene to upper Miocene(?) foraminiferal oozes are in contact with upper Oligocene nannofossil oozes. The late Oligocene foraminiferal assemblage (Zone P22/N3) includes *Globigerina venezuelana, Globigerina tripartita, Globoquadrina binaiensis, Globorotalia opima,* and *D. altispira altispira,* found in Samples 134-828A-8H-CC and 134-828A-9H-CC. Nonetheless, clear evidence of the latest Oligocene was not recorded (e.g., the presence of *Globorotalia kugleri*). Below this, a lower Oligocene assemblage (Zone P18/P19) was determined in Sample 134-828A-10H-CC. Species identified in this sample include *Catapsydrax dissimilis, Globigerina tapuriensis, Globigerina ampliapertura,* and *Globigerina preturrilina*.

Eocene

Finally, in Sample 134-828A-11H-CC, a middle Eocene fauna is represented by *"Globigerinoides" higginsi, Globigerina eocaena, Globigerina cryptomphala*(?), *Truncorotaloides topilensis,* and *Morozovella spinulosa*. No foraminifers were found within Core 134-828A-11H, raising the possibility of reworking as a plausible explanation for the isolated middle Eocene sample.

In Hole 828B, on the other hand, a lower Oligocene assemblage (Zones P18–21) was found in Samples 134-828B-1R-1, 25 cm, and 134-828B-1R-4, 130 cm, where the following species were identified: *G. venezuelana, C. dissimilis, Globigerina gortanii, G. ampliapertura, Globigerina ciperoensis,* and *Globorotalia increbescens*. The foraminiferal age determined for this assemblage conflicts with the latest Eocene age suggested by nannofossils, but correlates well with the presumed stratigraphic equivalent in Hole 828A (see "Sediment Accumulation Rates" section, this chapter).

Benthic Foraminifers

Rare to common, well-preserved benthic foraminifers occur in the upper part of the Cenozoic strata at Site 828 (Sections 134-828A-1H-CC through 134-828A-6H-CC). A few poorly preserved benthic foraminifers are present in the lower part of Hole 828A, although no benthic foraminifers were found in Sections 134-828A-7H-CC and 134-828A-11H-CC.

The Cenozoic strata at Site 828 are divided into three assemblages based upon the variety of different species found in each one, as follows:

Assemblage Unit I

Section 134-828A-1H-CC includes several specimens of *Globobulimina pacifica, Melonis pacificus,* and *Melonis sphaeroides,* accompanied by some displaced specimens of *Bolivinita quadrilatera* and *Elphidium advena*.

Assemblage Unit II

Between Sections 134-828A-2H-CC and 134-828A-6H-CC, the characteristic species are deep-water foraminifers such as *Melonis pacificus, Pseudoparrella exigua,* and *Uvigerina hispidocostata*. The abundance of these species varies from sample to sample.

Assemblage Unit III

Below Section 134-828A-8H-CC, *Stilostomella lepidula* is the dominant species and is associated with a few specimens of *Pleurostomella alternans*.

All three assemblages contain paleobathymetric indicators: *Melonis pacificus* and *Melonis sphaeroides* of Assemblage Unit I; *Melonis pacificus* and *Pseudoparrella exigua* of Assemblage Unit II; and *Stilostomella lepidula* of Assemblage Unit III. These paleobathymetric indicators all suggest deposition in the lower bathyal zone (2000–3000 m). The differences observed in the assemblages may possess some additional paleoecologic significance, but shipboard time constraints prohibited a more quantitative investigation.

Radiolarians

Twenty-three samples from Hole 828A were examined for radiolarians but all were barren except for individual well-preserved specimens among the sand-sized mineral grains in the top four cores. Also barren were two samples examined from Core 134-828B-1R.

IGNEOUS PETROLOGY

Fragments of volcanic rocks were recovered from the lowermost parts of two holes drilled at Site 828 on the NDR. These volcanic rocks are found between 90.8 and 111.4 mbsf in Hole 828A and between 100.0 and 119.4 mbsf in Hole 828B (see "Lithostratigraphy" section, this chapter). In both cases rocks are assigned to lithologic Unit IV, which is below the

Table 3. Major and trace element analyses of volcanic rocks from Site 828, North d'Entrecasteaux Ridge.

Core, section Sample interval (cm) Rock type	15N-1 23–25 Basalt	15N-1 122–123 Basaltic andesite	15N-2 3–4 Basaltic andesite	15N-2 62–63 Basalt	12X-1 24–26 Basalt	7H-5 83–84 Ash layer
Major elements (wt%)						
SiO_2	49.37	53.25	52.13	48.68	50.71	
TiO_2	0.81	1.91	1.88	0.82	0.73	
Al_2O_3	18.11	14.36	14.46	17.86	16.46	
Fe_2O_3(t)	8.73	12.82	13.26	7.96	8.90	
MnO	0.13	0.19	0.20	0.15	0.15	
MgO	12.24	6.66	6.66	12.94	9.03	
CaO	7.03	5.43	5.53	8.31	10.19	
Na_2O	3.49	5.72	5.50	2.99	4.16	
K_2O	0.51	0.24	0.38	0.87	0.10	
P_2O_5	0.05	0.17	0.15	0.04	0.04	
Total	100.46	100.75	100.15	100.61	100.47	
LOI	6.19	3.41	3.70	6.77	6.77	
Mg#	0.74	0.51	0.50	0.76	0.67	
Trace elements (ppm)						
Ti	4856	11450	11271	4916	4376	5216
Ni	143	76	94	178	131	8
Cr	405	118	123	450	344	7
V	214	319	317	186	204	218
Cu	59	60	44	59	71	79
Zn	56	115	116	55	62	101
Sr	119	94	94	113	76	507
Rb	3	2	4	6	2	24
Ce	4	10	18	12	6	22
Ba	18	8	7	28	0	346
Nb	1	3	3	2	1	3
Zr	41	124	117	40	24	115
Y	17	40	40	14	18	27

Note: Fe_2O_3(t) = total iron as Fe_2O_3; LOI = loss on ignition; Mg# = MgO/(MgO + FeO_{total}) mol%.

Oligocene to Eocene nannofossil chalk (lithologic Unit III). They occur either as clasts in matrix-supported volcanic breccia (upper level) or as isolated lava fragments (lower level) that resulted from poor core recovery. Subangular to subrounded cobbles and pebbles show homogeneous lava textures, but in some cases form parts of volcanic breccias with reddish gray matrix.

A clast of greenish gray basaltic lava supported in a matrix of gray silt to dusky red sand was recovered from the upper level at 96 mbsf. This relatively differentiated basalt (Sample 134-828A-12X-1, 22–24 cm) has sparse phenocrysts of plagioclase (2%) and olivine (<1%) in a fine-grained matrix dominated by plagioclase (30%) and clinopyroxene (30%). Olivine is completely altered to serpentine and grains are recognized only by their characteristic morphology. Groundmass plagioclase and clinopyroxene show subophitic texture in which elongate plagioclase laths have slightly preferred orientation, and the anhedral clinopyroxenes sometimes form dendrites, indicative of quenching. The plagioclase laths are relatively large (0.1 to 0.3 mm) and are probably better referred to as microphenocrysts. The composition of plagioclase in both phenocrysts and groundmass is in the albite-oligoclase range. Other groundmass constituents are opaque minerals and turbid devitrified glass. Secondary calcite is pervasive, forming veins or filling vesicles.

Clasts of gray weathered lava ranging in size from 0.5 to 6 cm were recovered between 98 and 106 mbsf, just below the basaltic lava described above, but matrix was not recovered here. These clasts are similar in texture and color to the overlying lava, of which they are probably brecciated equivalents.

Rubbly lava fragments recovered from the lowest level of Hole 828A, between 107 and 111 mbsf, are fine-grained vesicular basalts and basaltic andesites. They are generally structureless and vary in size from unconsolidated coarse sand matrix, through pebbles, to cobbles. Some individual cobbles are composed of brecciated lava. These samples have undergone substantial alteration and oxidation: hand specimens characteristically show widespread areas of oxidation and development of chlorite together with veins of calcite. These alteration features are also evident in four thin sections, of which two (Samples 134-828A-15N-1, 23–25 cm, and 134-828A-15N-2, 62–63 cm) are basalts and two (Samples 134-828A-15N-1, 122–123 cm, and 134-828A-15N-2, 3–4 cm) are basaltic andesites. Olivine is completely altered to serpentine and chlorite, and plagioclase to sericite and clays. Clinopyroxene is relatively free from alteration. In addition, all samples show spots of opaque minerals 0.1 to 0.2 mm in diameter, which have the appearance of dark gray to reddish dark gray phenocrysts in the hand specimen. These opaque minerals are possibly anhedral iron oxide or hydroxide compounds that replace all the groundmass minerals but plagioclase. This feature is more evident in the basaltic andesites, which contain higher total Fe_2O_3, MnO, and TiO_2 than the basalts (Table 3). Calcite veining is not widespread among these samples; in Sample 134-828A-15N-2, 62–63 cm, calcite partially replaces olivine phenocrysts and fills vesicles in the groundmass. Radial clusters of zeolite are pervasive in the groundmass of the highly altered basalt (Sample 134-828A-15N-1, 23–25 cm).

The phenocryst assemblages inferred from the morphology consists of plagioclase + olivine ± clinopyroxene for basalts, and plagioclase + clinopyroxene for basaltic andesites. The estimated phenocryst content is much greater in the basalts (20 and 45 volume percent, or vol%) than in the basaltic andesites (6 vol% for both), all of which are more porphyritic than the basalt from the higher level in the same hole. The olivine pseudomorph content reaches 8 vol% in the basaltic

Sample 134-828A-15N-1, 23–25 cm. Groundmass constituents always include plagioclase laths, anhedral clinopyroxene, opaque minerals, and devitrified glass; they also include alkali feldspar in the basaltic andesites. A sample of highly phyric basalt Sample 134-828A-15N-2, 62–63 cm, shows subophitic texture, in which elongate anhedral clinopyroxene has the quench morphology of dendrites. This texture is similar to the higher-level basalt except for the clinopyroxene crystal size, which is much greater (0.1–1.0 mm vs. 0.03–0.1 mm). In contrast, both basaltic andesites show intergranular texture with granular clinopyroxene in the groundmass. Because of their highly altered character it is unlikely that the present chemical compositions are entirely representative of the original rocks.

Material similar to that in Hole 828A was recovered from 100–119 mbsf in Hole 828B, but here a piece of olivine dolerite (Sample 134-828B-3R-CC, 9–10 cm) was also included. The latter contains relatively fresh olivine (12 vol%) but the plagioclase (53 vol%) is albitized and sericitized and the clinopyroxene (30 vol%) has been largely altered to chlorite.

The variety of volcanic rock types found at the bottom of Holes 828A and 828B indicates that we had not penetrated "basement," in which we would have anticipated a more homogeneous basalt. Instead we appear to have sampled a very immature breccia or scree deposit that might have been associated with a volcanic island. The highly oxidized nature of the lowermost samples in Hole 828A suggests subaerial volcanism or eruptions in a shallow-water environment.

These rocks are more basic than the volcanic clasts from the sed-igneous breccia recovered at Site 827, which is across the trench toward Espiritu Santo Island. Samples from Site 827 often contain phenocryst-size orthopyroxene and hornblende, whereas those from Site 828 do not.

IGNEOUS GEOCHEMISTRY

Igneous rocks recovered from the two holes drilled at Site 828 have been described in the preceding "Igneous Petrology" section. One sample from the upper level (Sample 134-828A-12X-1, 24–26 cm; lithostratigraphic Unit IV) and four samples (Samples 134-828A-15N-1, 23–25 cm; 134-828A-15N-1, 122–123 cm; 134-828A-15N-2, 3–4 cm; 134-828A-15N-2, 62–63 cm; lithostratigraphic Unit IV) from the lower part of the breccia were selected for X-ray fluorescence (XRF) analyses on board, and the results are reported in Table 3. An ash layer (Sample 134-828A-7H-5, 82–83 cm), sampled from the top of lithostratigraphic Unit II of Hole 828A, has also been analyzed (Fig. 15). However, since this material was rather scarce, only trace element analyses are available. The ash layer contained about 90% volcanic and 10% organic and inorganic (calcite) components. The latter were removed using 1-N HCl solution in an ultrasonic bath. After leaching, the sample contained more than 95% dark brown glass shards, plus crystals of plagioclase, clinopyroxene, and magnetite. The material treated in this way can be regarded as approximating to the original magma composition.

Ash Layer Geochemistry

The trace element composition of the volcanic ash (Sample 134-828A-7H-5, 83–84 cm) has been plotted on a MORB-normalized incompatible element diagram (normalizing values from Pearce, 1982), together with some analyses of recent lavas from Epi and Emae islands, Vanuatu (Dupuy et al., 1982; Briqueu et al., 1984) (Fig. 16). These lavas range in composition from basalt (Epi 19, Emae 4) to dacite (Epi 30), thus representing a large spectrum of compositions erupted in the Central Chain of the New Hebrides Island Arc. The similarity between these patterns and that of the ash layer recovered from Hole 828A is striking, suggesting that the ash layer originated as a fall deposit from one of the recent eruptions from the nearby islands.

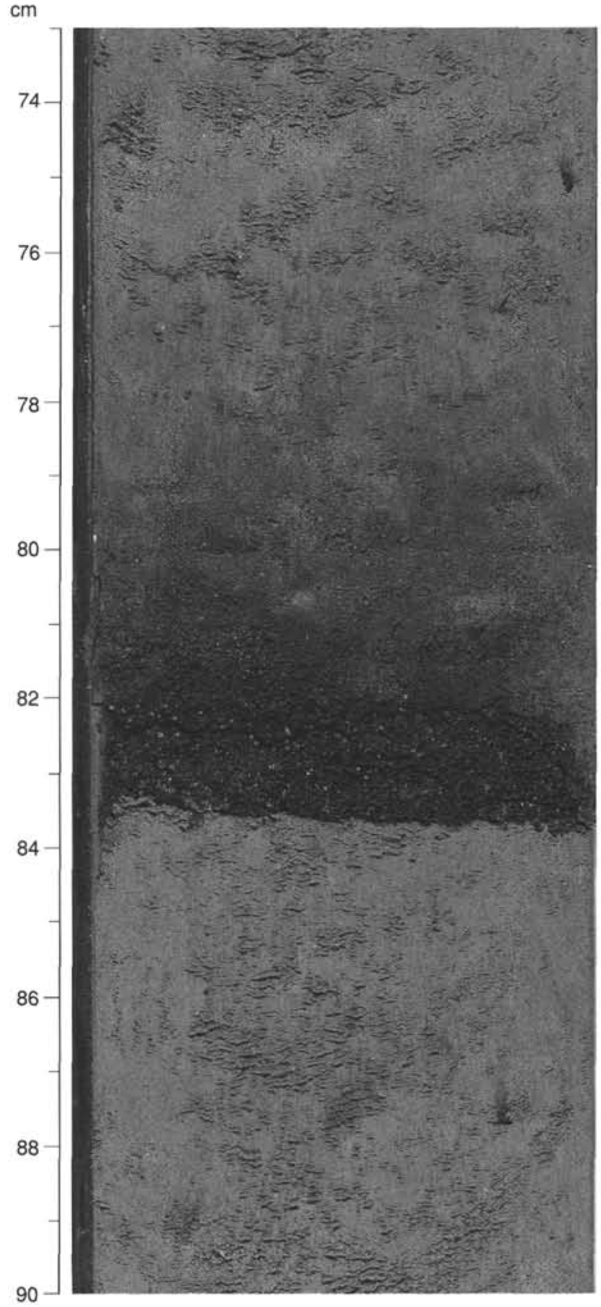

Figure 15. Photograph of the ash layer (Sample 134-828A-7H-5, 83–84 cm) occurring at the top of Unit II.

Lava Geochemistry

The analyses of Table 3 are reported on an anhydrous basis (see "Explanatory Notes" chapter, this volume, for the analytical procedure). The high loss on ignition (LOI; between 3.41 and 6.77 wt%) reflects the degree of alteration observed in thin section. In fact, the glassy material in the groundmass and most of the phenocrysts (i.e., olivine, clinopyroxene, and plagioclase) appear to be replaced by chlorite, serpentine, and calcite or altered to clay minerals. The percentage of second-

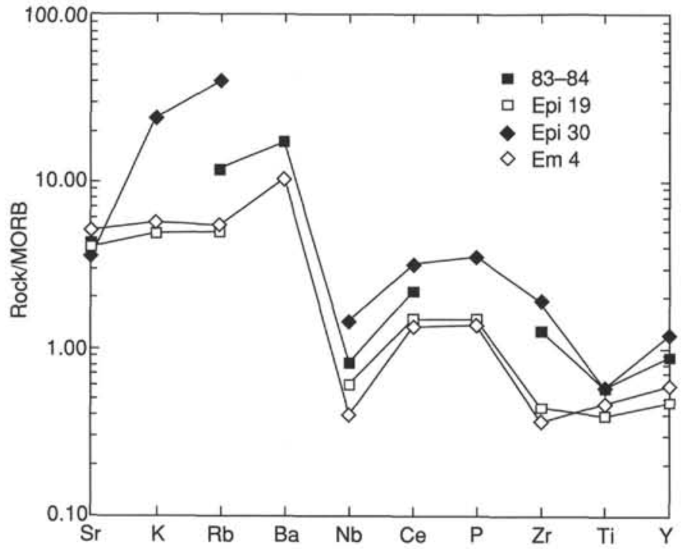

Figure 16. MORB-normalized incompatible element diagram of an ash layer from Site 828 and lavas from the New Hebrides Island Arc. 83–84 refers to Sample 134-828A-7H-5, 83–84 cm. Epi 19 and 30 refer to basalt and dacite, respectively, from Epi Island, and Em 4 indicates a basalt from Emae Island (Dupuy et al., 1982; Briqueu et al., 1984). Normalizing values from Pearce (1982).

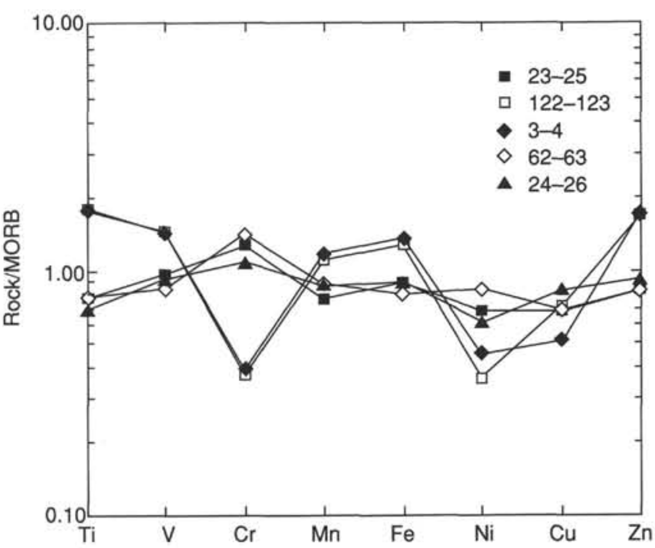

Figure 17. MORB-normalized compatible element diagram for basalts and basaltic andesites from the North d'Entrecasteaux Ridge (normalizing values from Dupuy et al., 1982). 23–25 = Sample 134-828A-15N-1, 23–25 cm; 122–123 = Sample 134-828A-15N-1, 122–123 cm; 3–4 = Sample 134-828A-15N-2, 3–4 cm; 62–63 = Sample 134-828A-15N-2, 62–63 cm; 24–26 = Sample 134-828A-12X-1, 24–26 cm.

ary minerals ranges from 20% to 80% (see "Igneous Petrology" section, this chapter).

Because the rocks are highly altered, data pertaining to the most mobile elements, such as K, Rb, Ba, and Sr, and to some extent Na and Mg, may not represent the original composition, and must be interpreted with some reservations. Weight percent of MgO, for example, appears to be quite high, considering that only a few percent of olivine phenocrysts have been observed in thin section. Sample 134-828A-12X-1, 24–26 cm, contains 9.03 wt% MgO, about 3% lower than Sample 134-828A-15N-1, 23–25 cm, although both appear to have similar Ni content (131 and 143 ppm, respectively). Whether these differences reflect contrasting magma compositions or varying degrees of alteration is unclear. The concentration of Ba also appears to be very low (7–28 ppm), considering that a typical value for MORB ranges between 4 and 10 ppm (Wilson, 1989).

On a total alkali (Na_2O + K_2O) vs. SiO_2 diagram (not shown here), the samples fall in a field intermediate between alkaline and subalkaline compositions. However, the validity of such a classification is questionable in view of the altered nature of the samples and mobility of the elements concerned. The basalts (Samples 134-828A-15N-1, 23–25 cm, 134-828A-15N-2, 62–63 cm, and 134-828A-12X-1, 24–26 cm) have relatively high magnesium numbers (Mg#, magnesium number = $MgO/(MgO + FeO_{total})$ mol%) between 0.67 and 0.76. However, the more differentiated basaltic andesites (Samples 134-828A-15N-1, 122–123 cm, and 134-828A-15N-2, 3–4 cm) have Mg# between 0.51 and 0.50, respectively (Table 3).

The different degree of fractionation undergone by the lavas is also evident from Figure 17, where compatible element contents have been normalized to MORB (Dupuy et al., 1982). Samples 134-828A-12X-1, 24–26 cm, 134-828A-15N-1, 23–25 cm, and 134-828A-15N-2, 62–63 cm, considered almost undifferentiated, show nearly flat patterns, except for positive Cr anomalies, whereas more fractionated samples (Samples 134-828A-15N-1, 122–123 cm, and 134-828A-15N-2, 3–4 cm) are depleted in Cr and Ni. The conspicuous decrease in Cr and Ni contents indicates that the main liquidus phases are olivine

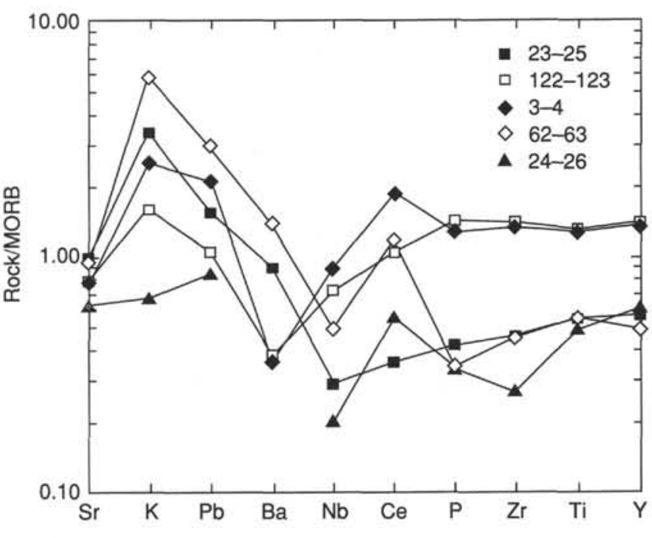

Figure 18. MORB-normalized incompatible element diagram for basaltic rocks from the top of North d'Entrecasteaux Ridge. Numbers as in Figure 17. Normalizing values from Pearce (1982).

and clinopyroxene, whereas the increase in Ti, V, and Fe suggests that the fractionation of oxide phases, such as magnetite or titanomagnetite, is negligible.

The incompatible element contents of the five samples normalized to MORB (values from Pearce, 1982) are shown in Figure 18. Although large ion lithophile (LIL) elements are likely to have been perturbed by alteration, some useful information may be provided by the high field strength (HFS) elements. Particularly significant in this regard is the depletion in Samples 134-828A-12X-1, 24–26 cm, 134-828A-15N-1, 23–25 cm, and 134-828A-15N-2, 62–63 cm, of elements such as Zr, Ti, and Y, together with the negative Nb anomaly. These elements, in fact, can be considered unaffected or only slightly affected by seawater-rock alteration processes (Hart et al., 1974; Bienvenu et al., 1990). Disregarding the LIL

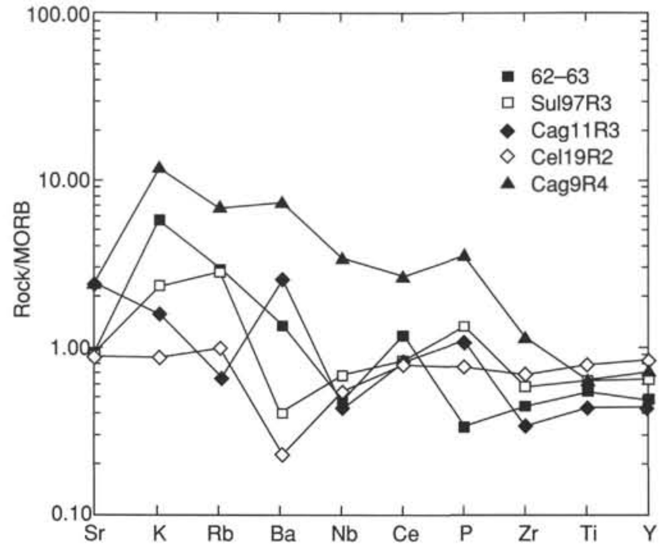

Figure 19. MORB-normalized incompatible element diagram for basaltic rocks of different magmatic affinities and a lava from the North d'Entrecasteaux Ridge (Sample 134-828A-15N-2, 62–63 cm). Cag9R4 and Cag11R3 refer to island-arc calc-alkaline and tholeiitic basalts, respectively, from the Cagayan Ridge (the Sulu Sea, ODP Leg 124; Spadea et al., 1991); Cel19R2 refers to MORB recovered from the Celebes Sea during Leg 124 (Serri et al., 1991); Sul97R3 refers to a basaltic rock with features transitional between island-arc tholeiites (IAT) and MORB recovered from the Sulu Sea during Leg 124 (Spadea et al., 1991).

elements, it will be seen that the HFS elements are more enriched in the basaltic andesite samples (Samples 134-828A-15N-1, 122–123 cm, and 134-828A-15N-2, 3–4 cm), which is probably a consequence of fractionation. Features such as the negative Nb anomaly and low HFS elements are typical geochemical signatures of subduction-related magmas (Wilson, 1989, and references therein).

In order to better constrain the tectonic environment of these magmas, a basalt sample (134-828A-15N-2, 62–63 cm) is plotted on the MORB-normalized diagram of Figure 19 together with a typical MORB from the Celebes Sea (Cel19R2; Serri et al., 1991), an island-arc tholeiite (IAT), and a calc-alkaline basalt from the Cagayan Ridge (Cag11R3 and Cag9R4, respectively; Spadea et al., 1991), and a basalt from the Sulu Sea that shows features transitional between IAT and MORB (Sul97R3; Spadea et al., 1991). The increase in low field strength (LFS) elements and decrease in HFS elements passing from tholeiitic to calc-alkaline types is apparent, and concentrations of Rb, Ba, and K vary by about one order of magnitude between the two series. Thus, the pattern for calc-alkaline magmas is steeper than that of MORB, which is almost flat, or, in some instances, depleted in LFS elements (Wilson, 1989, and references therein). The incompatible element pattern of Sample 134-828A-15N-2, 62–63 cm, one of the least differentiated basalts from the North d'Entrecasteaux Ridge (NDR), lies between those of MORB and IAT magmas (Fig. 19), as does that of the basalt from the Sulu Sea (Sul97R3). The only major difference between these two patterns is the higher phosphorus in the Sulu Sea sample.

Ti, Zr, and Y are among the most reliable elements for distinguishing the tectonomagmatic affinities of basaltic magmas (Pearce and Cann, 1973). Ti vs. Zr and Ti/100-Zr-Y*3 diagrams are considered here (Figs. 20 and 21). Because Samples 134-828A-15N-2, 3–4 cm, and 134-828A-15N-1, 122–123 cm, are more differentiated magmas they are not plotted on the diagrams. In Figure 20, rocks from NDR plot in the A and B fields, close to Sulu and Cagayan compositions, indicating a clear IAT tendency. In the Ti-Zr-Y diagram (Fig. 21), samples plot both in the IAT arc field and in the area between arc and mid-ocean ridge magmas. Hence the chemical compositions of the basaltic rocks recovered from NDR appear to indicate a magmatic affinity intermediate between basalts from an oceanic spreading axis and a volcanic island arc. Further studies are required to understand the significance of this signature in the evolution of DEZ and in the tectonic reconstruction of this part of the southwest Pacific.

SEDIMENT AND FLUID GEOCHEMISTRY

The pore-fluid chemistry was measured at Site 828 in order to determine the chemical composition of any fluid that may be subducted along with the downgoing plate and to observe chemical anomalies that might reflect fluids flowing out of the accretionary complex. In the Barbados subduction zone, low-chloride, methane-rich fluids were observed at the stratigraphic horizon of the décollement, but 4 km basinward of the deformation front (Mascle, Moore, et al., 1988; Gieskes et al., 1990), suggesting that fluids flowed from the décollement into the basin.

Only five pore fluid samples were collected, from the first and third core and then from every third core, because drilling encountered igneous rocks at a depth of 90.8 mbsf in Hole 828A and 100 mbsf in Hole 828B, reaching a total depth of only 129 mbsf (see "Lithostratigraphy" section, this chapter). The samples are evenly spaced approximately 30 m apart and were squeezed from sediment that appeared undisturbed by drilling. To minimize contamination, several millimeters were removed from the outer edge of each sample and thus the samples were probably not contaminated. There was little decrease in the yield of water with depth (Fig. 22), suggesting that the sediments are not greatly consolidated.

Results

Table 4 shows the contents of total carbon, organic carbon, inorganic carbon, and carbonate in these sediments. The carbonate content is plotted against depth in the "Lithostratigraphy" section (this chapter). The organic carbon content is plotted vs. depth in Figure 23.

Chlorinity and Salinity

The chloride concentration increases slightly with depth, reaching 569 mM at 47 mbsf (Fig. 24). This fairly constant chloride composition probably indicates that diffusive exchange with the overlying seawater is the dominant process controlling the chemistry of these pore fluids (Table 5). Except for the deepest sample, the salinity exhibits constant seawater value with depth. The slightly elevated chloride concentration may result from hydration of ash layers within the sediment column or from advection of chloride-rich fluids from the accretionary complex, possibly chloride-rich fluids observed similar to those observed at Site 827. The hydrology must be exceedingly complex, however, in order to mix fluids from Site 827 with the fluids at Site 828. The chloride-rich fluids at Site 827 were sampled from sediments confined to the upper plate whereas at Site 828 the high-chloride fluids were in sediments on the subducting plate. Fluids from within or below the décollement were not sampled at Site 827 and thus their chemistry is unknown.

Sodium, Potassium, Calcium, and Magnesium

Both sodium and potassium concentrations increase slightly from the sediment-water interface to 47 mbsf and

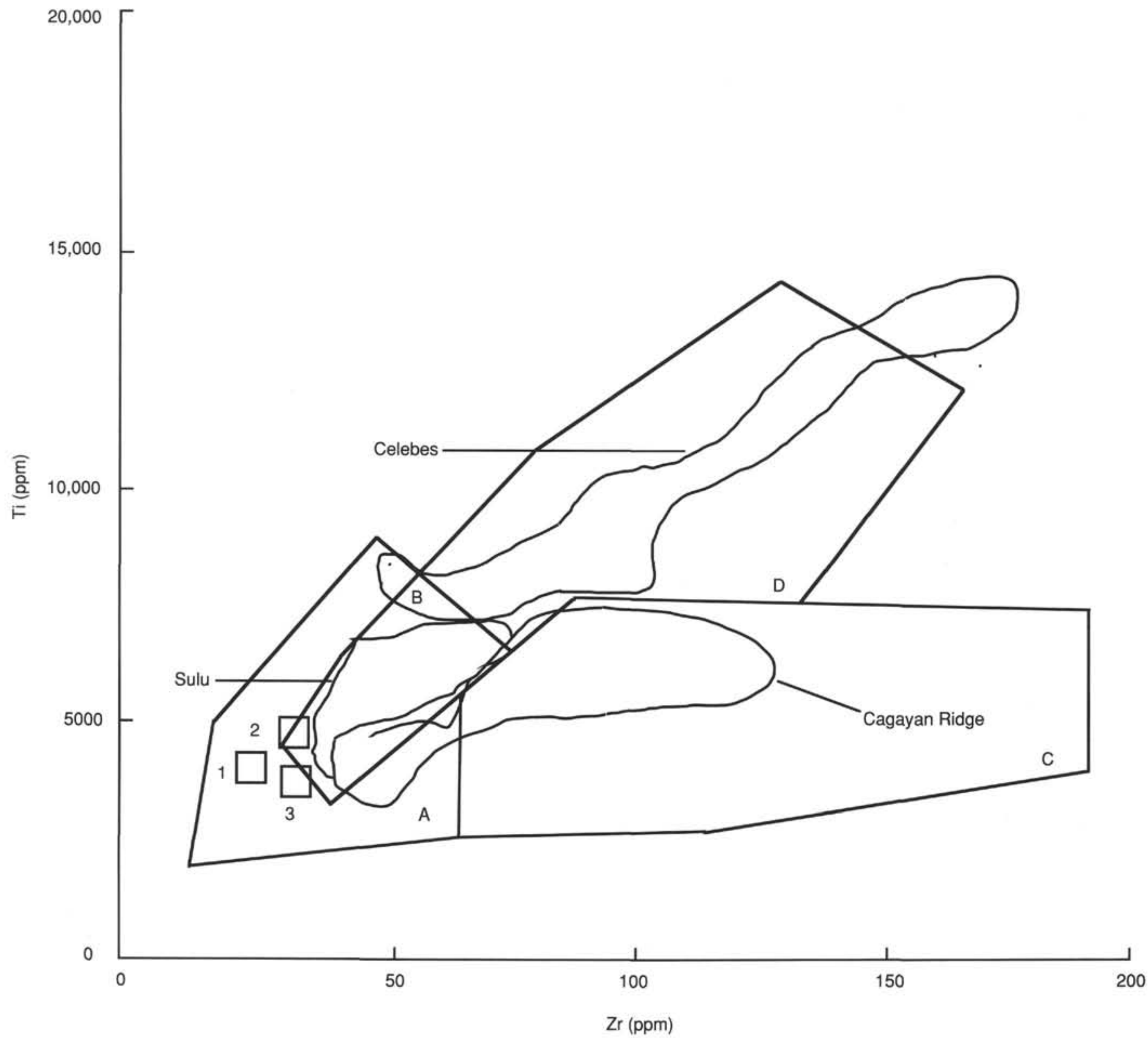

Figure 20. Samples from Site 828 plotted in the Ti-Zr tectonomagmatic discrimination diagram (after Pearce and Cann, 1973). Fields for samples from the Celebes and Sulu seas and the Cagayan Ridge are also included for comparison (Spadea et al., 1991; Serri et al., 1991). A and B = island-arc basalts; C = calc-alkaline basalts; D = mid-ocean ridge basalts; 1 = Sample 134-828A-15N-1, 23–25 cm; 2 = Sample 134-828A-15N-2, 62–63 cm; and 3 = Sample 134-828A-12X-1, 24–26 cm.

decrease from this depth to the sediment-basement contact; the sodium concentration decreases to 460 mM and potassium concentration decreases to 8.9 mM (Fig. 24). The calcium concentration exhibits approximately seawater value to 47 mbsf, but increases to nearly 30 mM at the sediment-basement contact. The magnesium profile is approximately linear with depth, decreasing to 43.2 mM. These solute concentrations probably result from diagenetic exchange reactions with the volcanic rocks at the total depth of this site, similar to the apparent diagenetic changes in concentrations at Site 827, although the concentration may reflect mixing of fluids from the accretionary wedge. Because the concentration profiles appear diffusional, exchange reactions with the basement rocks (McDuff and Gieskes, 1976; McDuff, 1981) are more likely to control the concentration gradients, particularly below the unconformity at ~50 mbsf, if it is an impermeable surface and prevents vertical diffusive exchange with the overlying seawater.

Ammonia, Phosphate, Alkalinity, Silica, Sulfate, and Methane

The profiles of ammonia, phosphate, and alkalinity exhibit distinct maxima at 18 mbsf (Fig. 24). The profiles probably result from oxidation of organic matter; the generally low concentrations of these solutes and lack of observable methane reflect the overall low organic carbon concentrations in the sediments (Fig. 23). The sulfate profile exhibits a distinct minimum at 18 mbsf, corresponding to the maximum in the phosphate, ammonia, and alkalinity concentration. This minimum probably reflects the extent of sulfate reduction.

The silica profile is characterized by a maximum at 47 mbsf (Fig. 24). The high silica concentration above 47 mbsf proba-

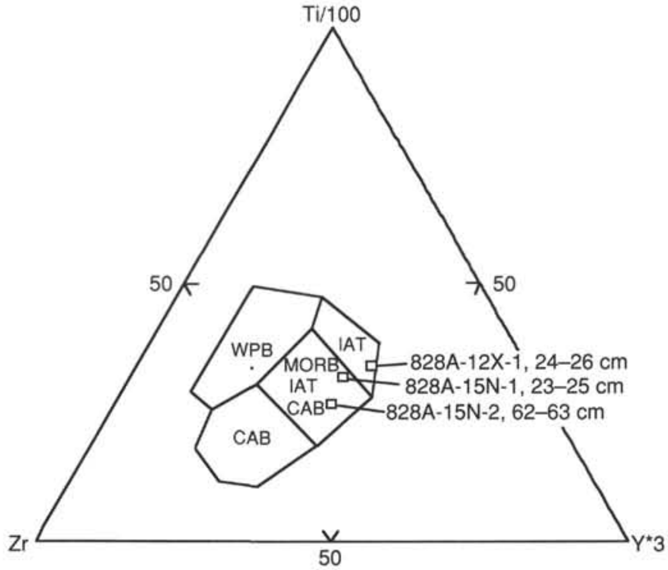

Figure 21. Ti-Zr-Y tectonomagmatic discrimination diagram (after Pearce and Cann, 1973) for basaltic lavas recovered at Site 828 on the North d'Entrecasteaux Ridge. WPB = within-plate basalts; IAT = island-arc tholeiites; CAB = calc-alkaline basalts; MORB = mid-ocean ridge basalt.

bly reflects alteration of the numerous volcanic ash layers. The decrease in silica below this depth may reflect the ash-poor nature of the nannofossil chalk of Unit III (see "Lithostratigraphy" section, this chapter).

Summary

The pore-fluid profiles apparently are controlled by diagenetic exchange reactions with volcanic ash-rich sediments and basement igneous rocks. These exchange reactions cause the sodium, potassium, and magnesium concentrations to decrease and also produce a large increase in the calcium concentration. The chloride concentration, however, exhibits a maximum that is ~2% greater than seawater concentration, which may either reflect local ash alteration or perhaps mixing with chloride-rich fluids from the accretionary wedge. The alteration of ash-rich sediments is also reflected in relatively high silica concentrations.

STRUCTURAL STUDIES

Cores recovered from Hole 828A do not display any structures related to tectonic activity. Bedding attitudes are generally horizontal, except in the uppermost part of the Hole 828A (Cores 134-828A-1H and 134-828A-2H) where dips up to 20° were measured (Fig. 25).

Several faults with dips ranging from 50° to 90° occur in Hole 828B (Sections 134-828B-1R-1 and -1R-2, 90–93 mbsf). These faults are conjugate; one set is composed of planes dipping steeply toward the east-southeast, and the other set consists of planes dipping steeply toward the west. Directions of dip are based on the core reference frame (see "Explanatory Notes" chapter, this volume). These features are considered to be natural faults rather than the result of drilling disturbances, because of the presence of mineralization on some slickensided planes that indicate *in-situ* faulting. A fault in the interval from 90 to 93 mbsf clearly indicates normal displacement. Furthermore, the bisectrix of the acute angle between the sets of conjugate fault planes is nearly vertical, which indicates that the compressional axis is more or less vertical.

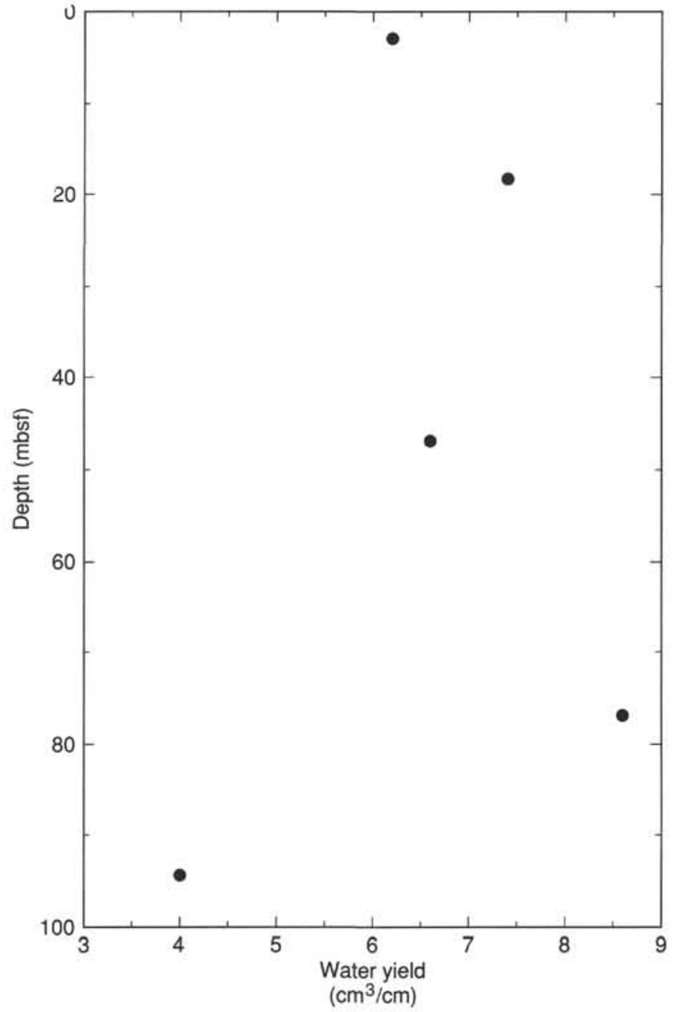

Figure 22. The yield of water per centimeter of core that was squeezed, Site 828. This value is only a qualitative measure of the water contained in the sediment because some variable amount of the sample was removed from each sample prior to squeezing.

Hole 828B is located on the northern flank of the NDR, where northwest-southeast-trending escarpments have been mapped from Seabeam bathymetric data (see "Introduction" chapter, this volume). Additional normal faults occur in Section 134-828B-1R-6, one of which shows an offset of the bedding plane of about 3 cm (Fig. 26).

PALEOMAGNETISM

Methods

Magnetic measurements using the pass-through cryogenic magnetometer were taken on all APC split archive halves recovered from Hole 828A and the first RCB core from Hole 828B. Alternating field (AF) demagnetization on these archive halves was performed at 5-cm intervals using a peak field intensity of 10 mT. This demagnetization level was chosen on the basis of our experience with Site 827 sediments, and turned out to be very appropriate. Several cores were oriented with the Eastman-Whipstock multishot tool *in situ* with respect to the downhole ambient field. A total of 30 discrete samples from the working halves were also measured in a stepwise demagnetization fashion. Magnetic susceptibility of

Table 4. Sediment carbon contents, Site 828.

Core, section, interval (cm)	Depth (mbsf)	Total carbon (wt%)	Inorganic carbon (wt%)	TOC (wt %)	$CaCO_3$ (wt%)
134-828A-					
1H-1, 117–120	1.2		0.8		7.0
1H-2, 125–130	2.8	1.6	1.3	0.3	10.6
1H-3, 95–98	4.0		1.0		8.6
2H-1, 101–104	5.4		1.3		10.7
2H-3, 101–104	8.4	1.8	1.4	0.5	11.2
2H-5, 101–104	11.4		1.1		9.4
2H-7, 54–57	13.9		1.0		8.2
3H-1, 122–124	15.1		1.1		9.0
3H-3, 122–124	18.1	1.7	1.3	0.4	11.0
3H-5, 126–128	21.2		1.5		12.2
3H-7, 10–12	23.0		1.3		10.7
4H-1, 110–113	24.5		1.2		10.1
4H-3, 110–113	27.5	2.0	1.6	0.4	13.4
5H-2, 110–113	35.5		1.2		9.6
5H-4, 110–113	38.5	1.9	1.5	0.4	12.7
5H-6, 110–113	41.5		1.4		12.0
6H-2, 105–108	45.0	1.3	1.1	0.2	9.1
6H-5, 105–108	49.5		2.6		21.2
6H-5, 137–140	49.8		2.4		20.0
6H-6, 105–108	51.0		2.3		19.0
7H-1, 143–145	53.3		2.6		21.8
7H-3, 143–145	56.3	3.5	3.1	0.4	25.7
7H-5, 143–145	59.3		6.5		53.8
8H-1, 140–143	62.8		11.2		93.5
8H-3, 140–143	65.8	11.7	11.3	0.3	94.5
8H-5, 140–143	68.8		11.3		93.7
8H-6, 140–143	70.3		9.9		82.4
9H-1, 23–26	71.1		9.7		80.9
9H-3, 22–24	74.1	10.5	9.9	0.5	82.6
9H-4, 103–104	76.4		10.0		83.5
9H-5, 20–22	77.1		10.1		84.0
9H-7, 22–24	80.1		10.5		87.3
10H-1, 37–40	80.8		10.2		84.7
10H-3, 37–40	83.8	10.6	10.2	0.4	84.5
10H-5, 37–40	86.8		9.6		79.6
11H-1, 37–40	90.3	10.2	9.4	0.8	78.1

Note: TOC = total organic carbon.

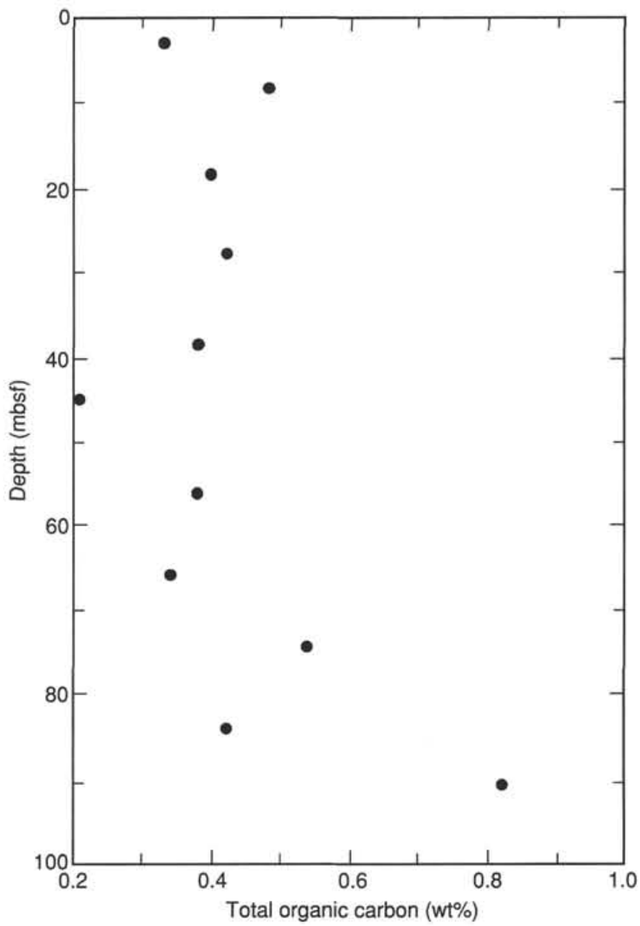

Figure 23. Total organic carbon content of sediments at Site 828 plotted vs. depth.

all cores was measured on the multisensor track (MST) at 2.5-cm interval prior to splitting.

Demagnetization Behavior

Typical examples of demagnetization diagrams are shown in Figure 27, and the variation of the intensity of magnetization vs. AF peak demagnetization for all demagnetized discrete samples is shown in Figure 28. Characteristic magnetizations are easily identified on the orthogonal demagnetization diagram and the secondary magnetization mostly induced by drilling is generally removed at 10 mT. The upper 60 m of Hole 828A consists of volcanic siltstone sediments. The magnetic behavior of these sediments is very similar to their counterparts at Site 827 although the preliminary results obtained on a few samples seem to indicate a slightly higher stability than that observed on Hole 827A.

The stable components of remanent magnetization for Cores 134-828A-1H through -7H (0–61.4 mbsf) are all of normal polarity, with a mean inclination value very close to the expected inclination from the Pleistocene to present (see Fig. 29). A major stratigraphic unconformity exists at the top of Core 134-828A-8H (61.4 mbsf), below which the sediments are mostly unconsolidated sand. Two discrete samples of the sand were taken at the top of Section 134-828A-8H-1. Negative and positive inclinations have been observed after demagnetization at 15 mT, which suggests two different polarities, although the results should be interpreted with caution.

The best evidence for a sequence of polarity reversals occurs in the interval from the bottom part of Core 134-828A-8H to the bottom of Core 134-828A-10H (61.4–89.9 mbsf) (Fig. 29). The polarity sequence determined from measurements in the cryogenic magnetometer was confirmed by progressive AF demagnetizations of the corresponding discrete samples (Fig. 27).

In Hole 828B, paleomagnetic results were obtained only on the first core because of poor recovery and eventual collapse of the hole. The magnetic polarity of the core was reversed.

Although the multishot orientation technique was applied to most of the APC cores at Site 828, this method only yielded readings for Cores 134-828A-4H, -6H, and -11H. The corrected declinations differed from the geographic north by a few tens of degrees. We noticed a systematic "leftward" shift of declination values throughout APC cores at this site, both before and after demagnetization. A close reexamination of the declination records of APC cores from Site 827 revealed the same shift. Although the cause of this shift is as yet unexplained, we suspect it may result in part from twisting of the drill string. Sediment twisting in the core pipe during coring can occur, and might explain the large variation in declination observed in Core 134-828A-6H. In addition, we have observed a systematic deviation up to 20° in marked plastic liners.

Magnetostratigraphy

The normal polarity of Cores 134-828A-1H through -7H (0–61.4 mbsf) suggests that these sediments were deposited during the Brunhes Chron (i.e., age <0.7 Ma). No magnetic polarity records are available for much of Core 134-828A-8H

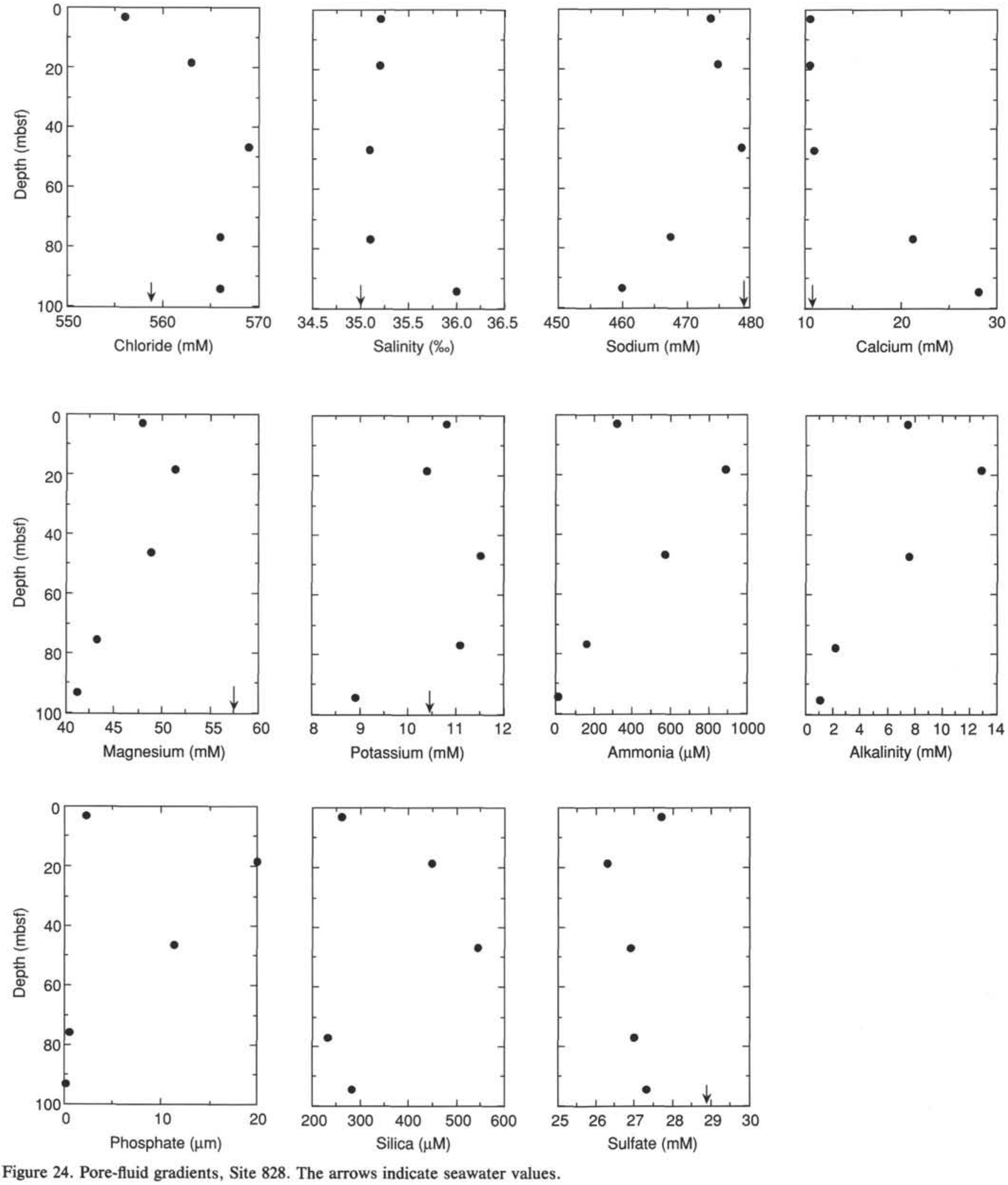

Figure 24. Pore-fluid gradients, Site 828. The arrows indicate seawater values.

because most of the recovered sediments are unconsolidated foraminiferal ooze. Major stratigraphic unconformities occur in Core 134-828A-8H as well; biostratigraphic ages in the core range from Pleistocene to Oligocene.

Five intervals of reversed polarity exist in the Oligocene sequence in Cores 134-828A-8H to -10H (61.4–89.9 mbsf). The preliminary biostratigraphic evidence suggests that the top of this sequence may represent nannofossil Zone CP17. However, biostratigraphic information from foraminifers seems to indicate a middle Oligocene age. Core 134-828A-11H did not provide any reliable polarity results (Fig. 29). The corresponding susceptibility data (Fig. 30) suggest that these

Table 5. Pore-fluid chemistry, Site 828.

Core, section, interval (cm)	Depth (mbsf)	pH	Salinity (‰)	Chloride (mM)	Sodium (mM)	Potassium (mM)	Magnesium (mM)	Calcium (mM)	Sulfate (mM)	Alkalinity (mM)	Phosphate (μM)	Ammonia (μM)	Silica (μM)
134-828A-													
1H-2, 145–150	3.0	7.8	35	556	474	10.8	49.9	10.4	27.7	7.3	2.3	323	263
3H-3, 145–150	18.4	7.9	35	563	475	10.4	53.3	10.4	26.3	12.7	20.0	888	449
6H-3, 145–150	46.9	7.6	35	569	479	11.5	50.9	10.9	26.9	7.4	11.4	567	545
9H-5, 145–150	76.9	7.6	35	566	467	11.1	45.3	21.1	27.0	2.0	0.5	161	232
134-828B-													
1R-3, 135–150	94.4	7.5	36	566	460	8.9	43.2	28.0	27.3	1.0	0.2	18	282

sediments differ from the pelagic sediments in Cores 134-828A-9H and -10H. Core 134-828B-1R consists of long (>20 cm), continuous pieces of sediments. Because the bedding planes of these sediments are nearly horizontal, the uniform positive inclination value exhibited by these sediments indicates a reversed polarity for Core 134-828B-1R. Although the reversal signal in Site 828 is a prominent, more precisely determined biostratigraphic ages as well as a more detailed paleomagnetic study are needed to construct a definitive magnetostratigraphy for Site 828.

Magnetic Susceptibility

Figure 30 shows the downhole profile of susceptibility for Hole 828A. Within the top 40 m, the magnetic susceptibilities have values consistently about 1.5×10^{-2} SI. These high susceptibility values correspond to the upper part of the Pleistocene volcanic silt in this interval. The susceptibility values gradually decrease below this interval, corresponding well with the lithological variation observed in these cores. There is almost no susceptibility signal in the nannofossil ooze zone. Pelagic sediments from Cores 134-828A-9H to -10H have low susceptibility values.

SEDIMENT ACCUMULATION RATES

Sediment accumulation rates were estimated for Holes 828A and 828B from an age-vs.-depth plot (Fig. 31). The curve is defined by 12 well-constrained chronostratigraphic events and zones (Table 6). These events include nannofossil and foraminiferal datum levels (first and last occurrences) and nannofossil zones. The boxes have been drawn to show the uncertainty of zonal boundaries (particularly important where the zone is limited by a hiatus, e.g., nannofossil Zone CP17 to CP19), compared to fixed points given by well-defined datums (e.g., first occurrence *Globorotalia tumida*). In addition, paleomagnetic information was used to draw that part of the curve in the Brunhes Chron. The beginning of the Brunhes Chron as a datum point appears more precise in this case than the use of either foraminifers and nannofossils (for an extensive discussion on differences in datum levels between these two groups of microfossils see "Biostratigraphy" section, this chapter). Radiometric ages follow the Cenozoic time scale outlined in the "Explanatory Notes" chapter (this volume).

High sediment accumulation rates are recorded for the Brunhes Chron (~60 m/m.y.), compared to the Pliocene to Eocene sequence (5 m/m.y. or less). Equally outstanding is the existence of two major hiatuses, one at ~62 mbsf (top of Core 134-828A-8H) where the upper Pliocene to lower Pleistocene are missing, and the other at ~69 mbsf (Section 134-828A-8H-6) where the Miocene to the uppermost Oligocene are missing. The relationship between the Eocene and Oligocene is not clear because microfossils in the lowermost interval of Hole 828A (Core 134-828A-11H) occurred only in the core catcher (see "Biostratigraphy" section, this chapter). At an equivalent depth in Hole 828B (Section 134-828A-1R-CC), an early Oligocene foraminiferal fauna (latest Eocene nannofossil assemblage), is found indicating a possible correlation horizon with Hole 828A (Fig. 31). Holes 828A and 828B are therefore combined to represent a continuous depositional sequence for the purpose of calculating sediment accumulation rates.

PHYSICAL PROPERTIES

Measurements of index properties, Hamilton Frame sonic velocities, undrained shear strength, and thermal conductivity were completed on sediments recovered at Site 828. Full APC cores from Hole 828A were measured with the gamma-ray attenuation porosity evaluator (GRAPE) and the compressional-wave (*P*-wave) logger (PWL) on the multisensor track. All measurements at Site 828 were made according to the procedures described in the "Explanatory Notes" chapter (this volume).

Index Properties

Values of porosity (wet and dry), bulk density (wet-, dry-, and grain), and water content (dry and wet) for Site 828 are listed in Table 7. Figure 32 illustrates the variation of porosity, water content, and bulk density as a function of depth below seafloor. Figure 33 illustrates the relationship between bulk density and porosity as a function of depth below seafloor.

At Site 828, porosity ranges from 72.2% to 38.2%, water content ranges from 92.6% to 22.3%. Bulk density ranges from 1.50 to 2.15 Mg/m^3.

The index properties at Site 828 correspond to the lithostratigraphic units (see "Lithostratigraphy" section, this chapter). Lithostratigraphic Unit I (0.5–58.7 mbsf) is composed of unlithified volcanic silt interbedded with layers of sandy volcanic silt. Porosity and water content increase slightly from 48.9% to 67.8% and from 46.6% to 69.3%, respectively, between the surface and near the base of the unit (2.7–51.0 mbsf). Values of bulk density are more scattered and decrease from 1.90 to 1.70 Mg/m^3 between 4.0 and 51.0 mbsf. Few measurements were made in the ooze of lithostratigraphic Unit II (58.7–69.3 mbsf). Porosity varies little, between 60.7% and 72.2%, with the exception of one value (48.6% at 65.8 mbsf). Both water content and bulk density are more scattered than porosity: water content ranges from 49.9% to 70.8% and bulk density ranges from 1.50 to 1.75 Mg/m^3. In the nannofossil chalk of lithostratigraphic Unit III (Hole 828A: 63.9–90.8 mbsf; Hole 828B: 90.0–100.0 mbsf), index properties are fairly constant. Porosity ranges only from 59.3% to 66.4%; water content and bulk density vary from 51.4% to 70.8% and 1.61 to 1.85 Mg/m^3, respectively. Only one measurement of the volcanic breccia in lithostratigraphic Unit IV (Hole 828A: 90.8–111.4 mbsf; Hole 828B: 100.0–111.4 mbsf) was made (93.3 mbsf in Hole 828A): porosity is 38.2%, water content is 22.3%, and bulk density is 2.15 Mg/m^3.

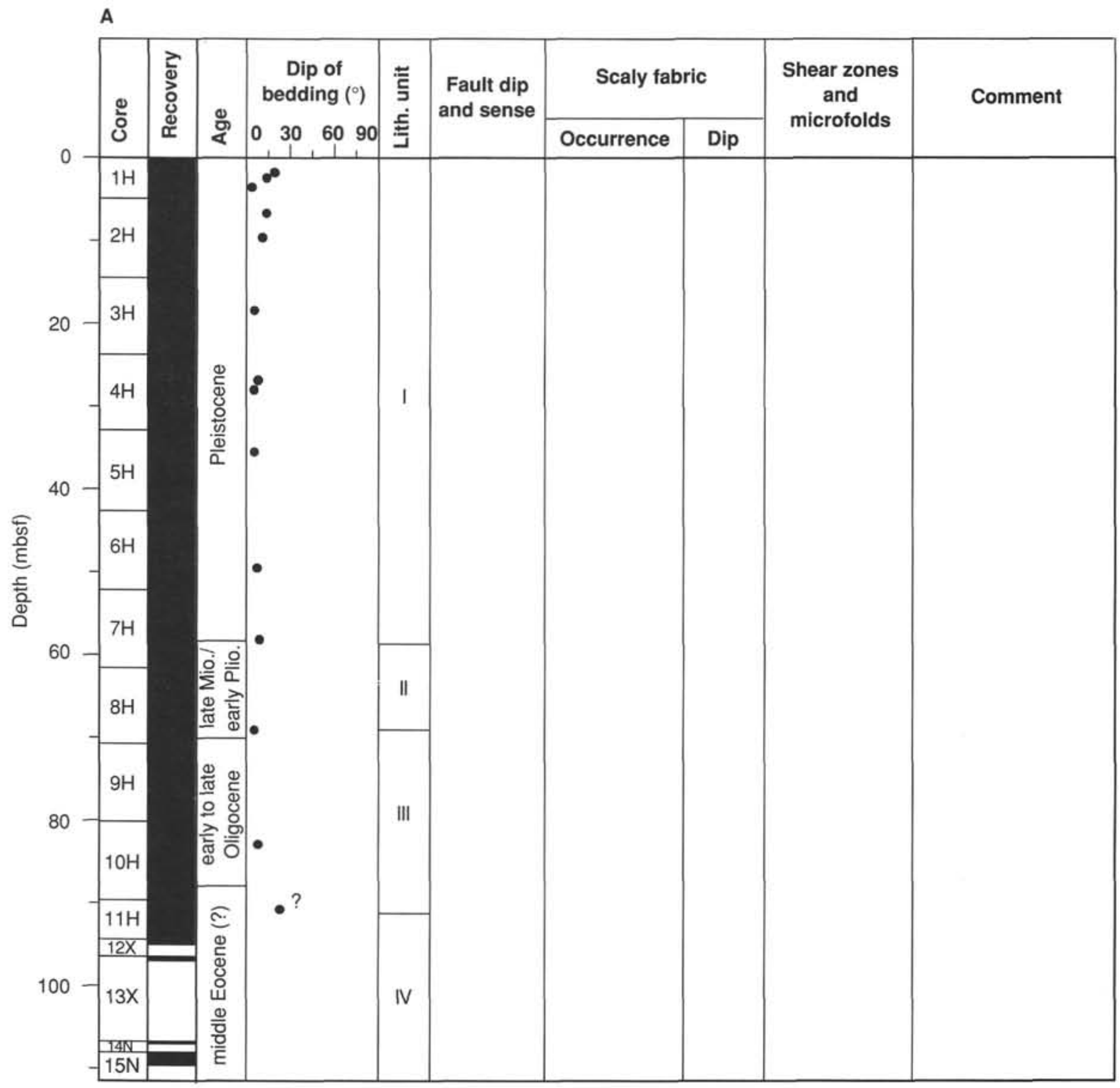

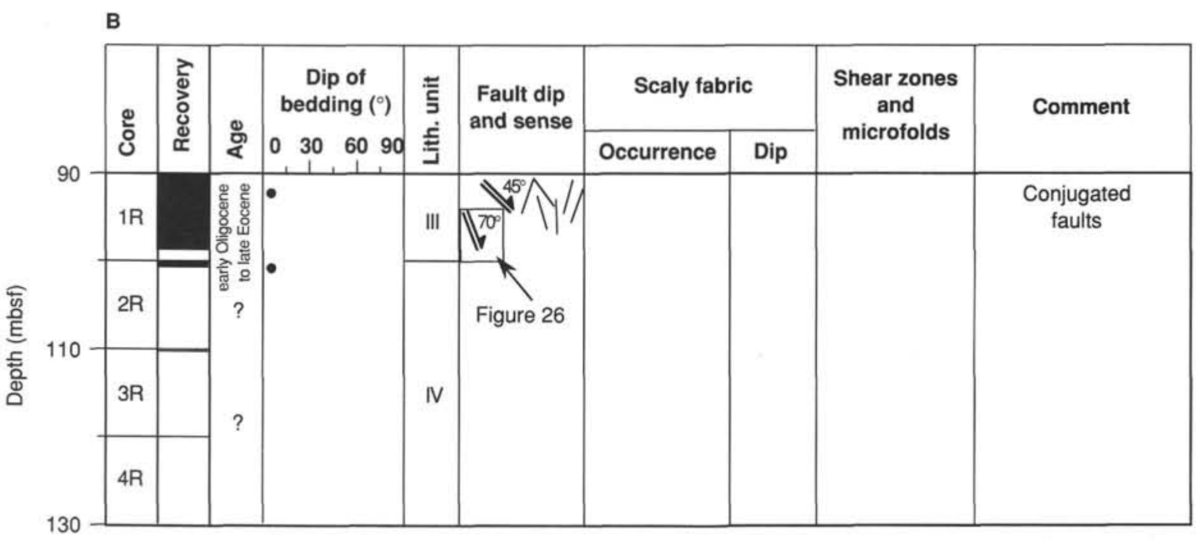

Figure 25. Structural logs of Hole 828A (**A**) and Hole 828B (**B**).

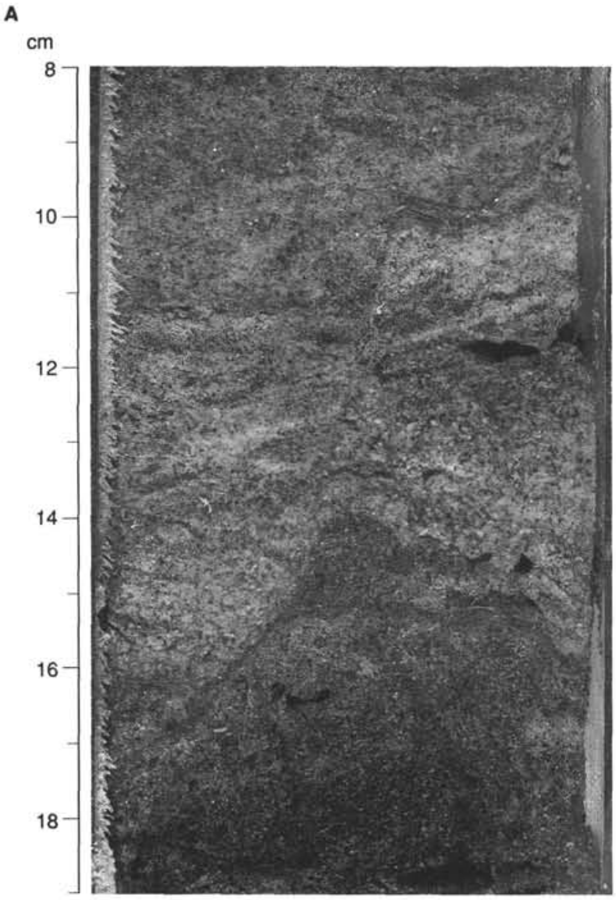

Figure 26. Photograph (**A**) and sketch (**B**) of the normal fault observed in Section 134-828B-1R-6.

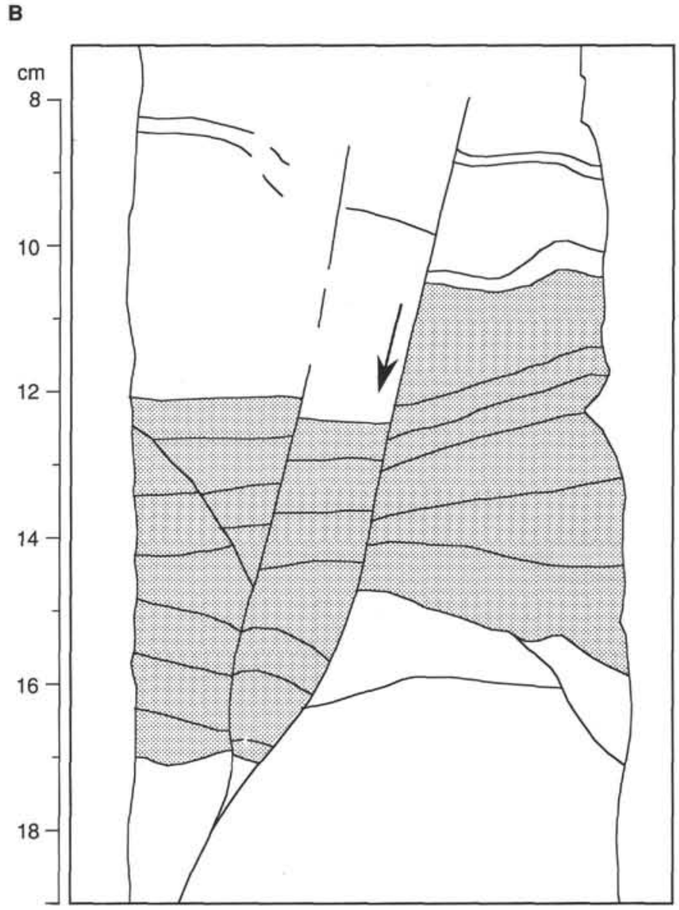

Figure 26 (continued).

Sonic Velocity

Sonic velocities were measured using both the PWL and the Hamilton Frame in Holes 828A and 828B. Hamilton Frame sonic velocity measurements are listed in Table 8, and the variation in velocity is shown in Figure 32. Measurements from PWL and Hamilton Frame agree well with each other, and because of this and the consistent use of the Hamilton Frame in all holes, only the measurements made in the Hamilton Frame are discussed below.

At Site 828, vertical velocity ranges from 1541 to 1825 m/s and horizontal velocity ranges from 1525 to 1912 m/s. The vertical and horizontal velocities are isotropic to semi-isotropic at Site 828. As with index properties, the velocity data at Site 828 correspond well with the lithostratigraphic units. In lithostratigraphic Unit I (0–58.7 mbsf), vertical velocity is fairly constant, and ranges from 1569 to 1641 m/s with one exception (1825 m/s at 56.3 mbsf). The horizontal velocity is slightly more scattered, and ranges from 1556 to 1707 m/s, although at 56.3 mbsf, horizontal velocity is 1859 m/s. The greatest anisotropy at Site 828 occurs at 24.5 mbsf, where the difference between the vertical and the horizontal velocity is 78 m/s. In lithostratigraphic Unit II (58.7–69.3 mbsf), only one vertical velocity was measured, 1598 m/s at 59.3 mbsf. The horizontal velocity increases slightly from 1590 to 1621 m/s between 59.3 and 65.6 mbsf. The vertical velocity is fairly constant in lithostratigraphic Unit III (Hole 828A: 63.9–90.8 mbsf; Hole 828B: 90.0–100.0 mbsf), and ranges from 1541 to 1579 m/s. The horizontal velocity decreases lightly from 1573 to 1525 m/s between the top of lithostratigraphic Unit III (70.3 mbsf) and 80.8 mbsf; from 83.8 to 92.9 mbsf, horizontal velocity is scattered and ranges from 1548 to 1652 m/s. At 97.7 mbsf, horizontal velocity is 1912 m/s, the highest velocity measured at Site 828. No other velocity data exist for lithostratigraphic Unit IV.

Shear Strength

Vane shear strength was measured on the parts of Hole 828A that were neither too stiff nor too unlithified for insertion of the blade. The miniature vane-shear device was used on cores down to 60.8 mbsf; from 72.1 to 89.8 mbsf, the torvane device was used for all but one measurement. Shear-strength measurements are listed in Table 9 and plotted as a function of depth below seafloor in Figure 34.

Shear strength increases in lithostratigraphic Unit I (0–58.7 mbsf) from 38.1 kPa at 2.7 mbsf to about 110 kPa at 58 mbsf. A maximum of 209.7 kPa was measured at 51.0 mbsf. Only two measurements of shear strength could be made in the soupy ooze of Unit II (58.7–69.3 mbsf): 83.6 kPa at 59.3 mbsf and 36.6 kPa at 60.8 mbsf. Shear strength increases in the nannofossil chalk of Unit III (69.3–90.8 mbsf) from 51.5 kPa at 70.3 mbsf to maximum of 142.3 kPa at 86.7 mbsf.

Thermal Conductivity

Thermal conductivity values at Site 828 range from 0.9 to nearly 1.6 W/(m · K) (Table 10) and, as at Site 827, follow a pattern that shows the influence of water content on thermal conductivity in the sediment (Fig. 35). Thermal conductivity values are constant around 1.0 W/(m · K) from the seafloor to 60 mbsf, with only minor deviations to 0.9 W/(m · K) at several depths. These slight decreases correlate with index proper-

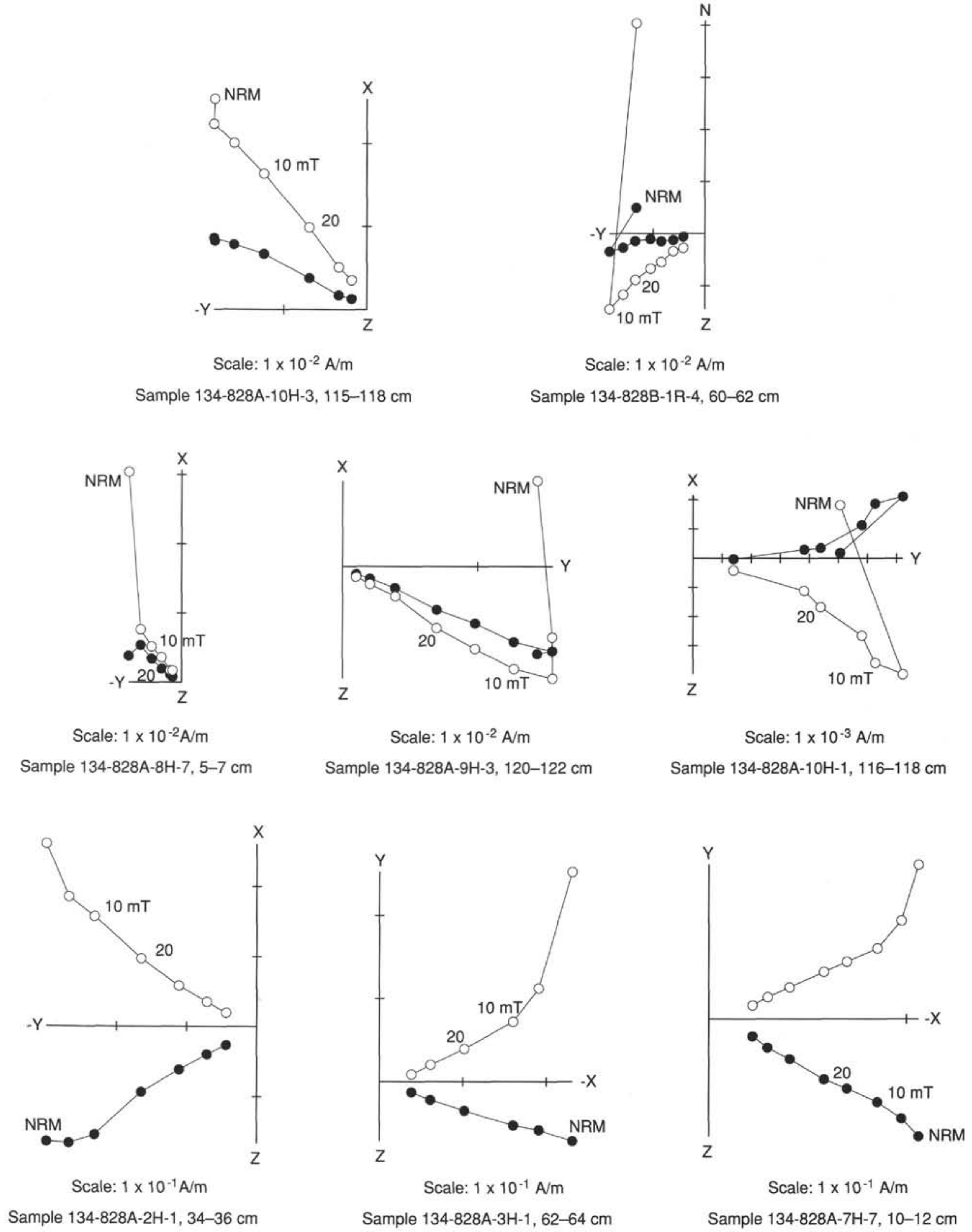

Figure 27. Representative orthogonal demagnetization plots of discrete samples from Site 828. Open circles represent vector endpoints projected onto the vertical plane; solid circles, endpoints projected onto the horizontal plane. NRM = natural remanent magnetization.

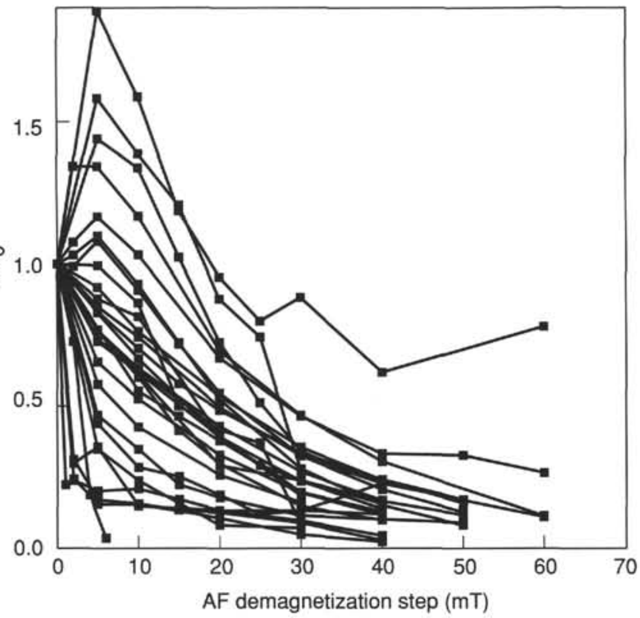

Figure 28. Normalized natural remanent magnetization (NRM) intensities vs. AF demagnetization steps for 30 discrete samples from Holes 828A and 828B. J/J_0 is the ratio of magnetic intensity (J) after demagnetization at a particular step to the NRM intensity (J_0). The sharp drop of the relative intensities indicates very low stability of the NRM.

ties, corresponding to measurements of increased water content and decreased bulk density. The lowest thermal conductivity value recorded was 0.91 W/(m · K) at 60 mbsf, in the soupy carbonate ooze of lithostratigraphic Unit II (58.7–69.3 mbsf). No other thermal conductivity measurements could be made in this unit because of the soupiness of the sediments. Thermal conductivity increases to a range of 1.20–1.40 W/(m · K) in lithostratigraphic Units III and IV, and reaches a maximum of almost 1.60 W/(m · K) from 90 to 95 mbsf in lithostratigraphic Unit IV, which consists of sed-lithic breccias. This point correlates with a very low water content value. However, other water content values in this unit are similar to those recorded at shallower depths. The increase in thermal conductivity may therefore result from some factor other than water content.

Summary

The most notable changes of physical properties at Site 828 are the increase in porosity and water content and the decrease in bulk density in lithostratigraphic Unit I (0–57.7 mbsf in Hole 828A). This unit and lithostratigraphic Unit I (0–86.0 mbsf in Hole 827A) at Site 827 comprise similar lithologies (dark greenish gray unlithified volcanic silt with interbeds of very dark gray, normally graded beds of sandy volcanic silt) and can therefore be correlated to each other. Porosity and water content increase in lithostratigraphic Unit I at Site 828, whereas general decrease occurs at Site 827. At about 58 mbsf, porosity is about 10% higher at Site 828 than at Site 827, water content is about 20% higher, and bulk density is 0.3 Mg/m^3 lower. No thrust faults or structures related to tectonic deformation are displayed in these sediments (see "Structural Studies" section, this chapter, and the "Site 827" chapter, this volume). Also, the measured shear strength values at Site 828 are generally lower than at Site 827 and do not show the same strong, continuous increase with depth, which suggests that the sediments at Site 828 generally are less disturbed than at Site 827. The divergent index properties and the shear strength results may reflect differences resulting from the location of the sites in relation to the subduction zone area. Site 827 is located on the forearc slope, and is more affected by subduction process than is Site 828, which is located on the northern flank of North d'Entrecasteaux Ridge.

SUMMARY AND CONCLUSIONS

Site 828 is located at 15°17.3′S, 166°17.04′E, on the Australia-India plate, along the northeastern flank of the NDR about 2 km west of the active convergent margin that separates the Australia-India plate from the Pacific plate (New Hebrides microplate). The site lies 150 km west of the active volcanic chain of the central New Hebrides Island Arc (Vanuatu) and about 40 km west of the western coast of Espiritu Santo Island, one of several islands associated with the lower Miocene Western Belt of islands. Site 828 is located on a flat, terrace-like feature that projects out from the otherwise steeply dipping slope in a water depth of 3086.7 m (Fig. 1). It lies near the collision zone of the NDR with the arc, an area where the Australia-India plate seafloor is bending down into the eastward-dipping subduction zone. In response to this curvature the terrace-like feature on which Site 828 lies has been faulted and may be part of a series of structural features oriented northwest-southeast that step down to the east. Site 827 is 4 km east of Site 828, across the convergence boundary where the forearc is deformed from the collision of the NDR and subduction.

Two holes were drilled at Site 828. Hole 828A was drilled and cored with the APC and XCB to 111.4 mbsf, with 101.34 m of core obtained for a recovery of 91%. Hole 828B, offset approximately 214 m to the northwest of Hole 828A, was drilled with the RCB to a depth of 129 mbsf, coring 39 m, with 7.92 m of core obtained for a recovery of 20.3%.

Four lithostratigraphic units were defined and described for this site (Fig. 36). Unit I (0–58.7 mbsf) is a 58.7-m-thick, Pleistocene, dark greenish gray volcanic silt with foraminiferal sand interbeds; the contact with underlying Unit II is marked by a dark brown bioturbated ash bed. Unit II (58.7–69.3 mbsf) is a 10.6-m-thick, upper Miocene–lower Pliocene to Pleistocene foraminiferal ooze divided into two subunits: Subunit IIA and Subunit IIB. Subunit IIA (58.7–61.9 mbsf) is a 3.2-m-thick, Pleistocene, light brownish gray to very pale brown foraminiferal ooze with nannofossils and alternating layers of silt and ash with firm to soupy foraminiferal sands. Subunit IIB (61.9–69.3 mbsf) is a 7.4-m-thick, lower Pliocene to upper Miocene, very pale brown to white unconsolidated foraminiferal ooze separated from Subunit IIA by an unconformity(?) and a sharp color change, marking the end of the volcanic components of the overlying sediment. Unit III (69.3–90.8 mbsf) is a 21.5-m-thick, lower to upper Oligocene, highly bioturbated, light yellowish brown nannofossil chalk that unconformably underlies Subunit IIB. Unit IV (90.83–111.4 mbsf) is at least 20.6 m thick and consists of upper Eocene to lower Oligocene igneous breccia, with basaltic clasts and diabase fragments. Clasts and matrix range in color from light greenish gray to dusky red.

Drilling at Site 828 revealed a nearly 91-m-thick, lower Oligocene to Pleistocene marine sedimentary sequence unconformably(?) overlying volcanic breccia that may have been subaerially altered. Hole collapse prevented penetration of basement rocks of the NDR, although the igneous rocks recovered are believed to be the eroded and weathered detritus of a volcanic basement complex. The rocks exhibit a blotchy red and greenish color that suggests extensive oxidation and alteration, perhaps during a period of emergence. The upper part of Unit IV included weathered clasts of apparently more differentiated volcanics within a coarse-grained breccia.

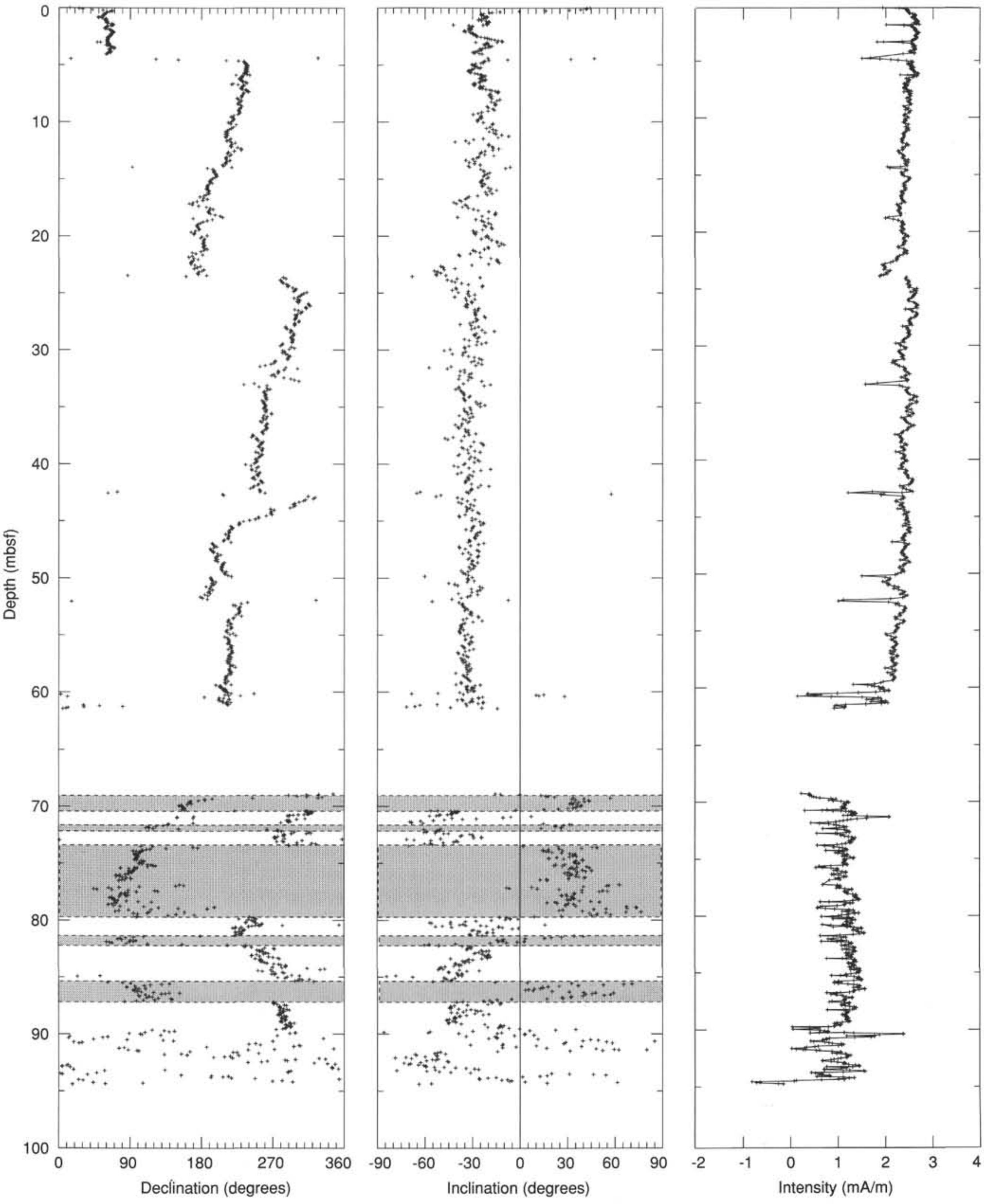

Figure 29. Depth plot of stable magnetization (after AF demagnetization at 10 mT) for cores in Hole 828A. Shaded areas represent possible reversed intervals, unshaded areas represent normal intervals.

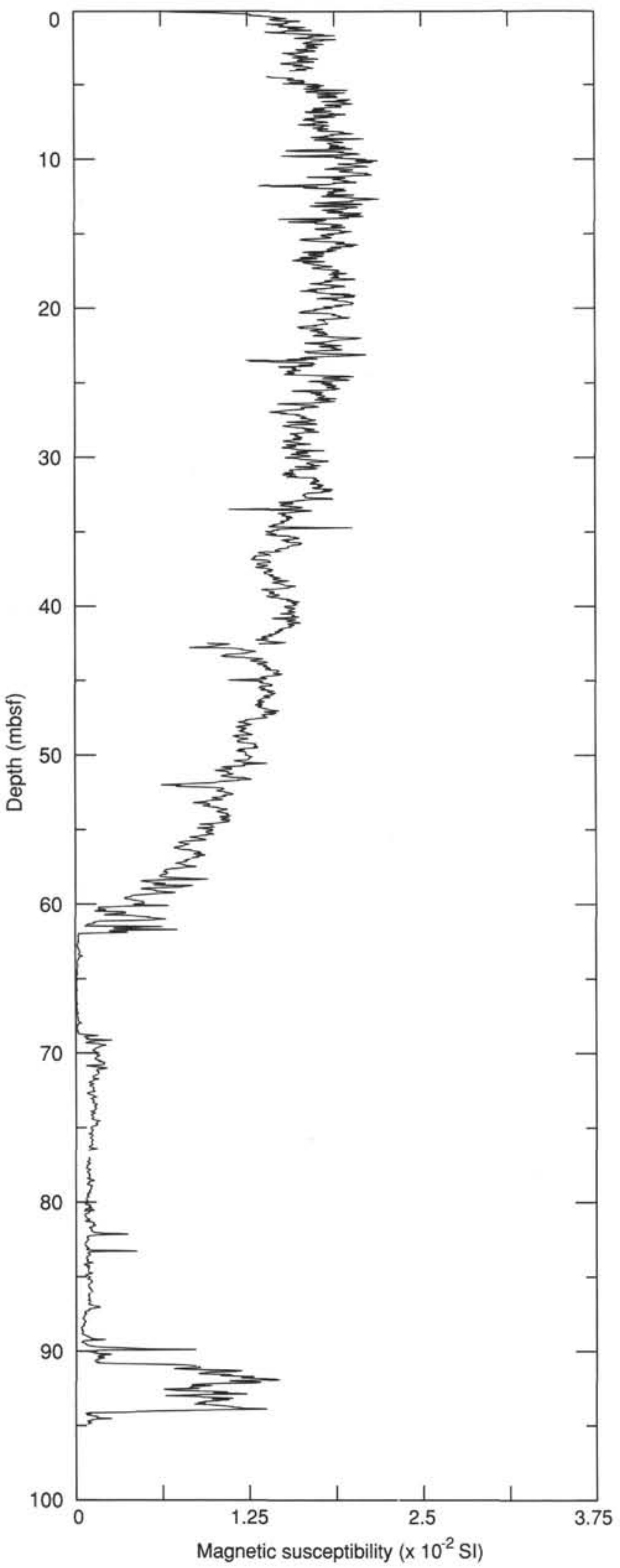

Figure 30. Plot of variation of the magnetic susceptibility with depth in Hole 828A.

Beneath the breccia, rubbly, weathered, aphyric, fine-grained, vesicular, basalts, and andesites were encountered. One piece of olivine dolerite was found in Hole 828B. In contrast to the volcanic rocks recovered at Site 827, igneous rocks at Site 828 appear more mafic and lack phenocryst-sized orthopyroxene and hornblende. Initial geochemical analyses indicate that the basaltic rocks share a magmatic affinity intermediate between MORB and island-arc tholeiite, suggesting that an oceanic island arc is their most probable origin.

At least three unconformities (61.9, 69.3, and 90.8 mbsf), two of which are questionable (61.9 and 90.8 mbsf), interrupt the marine sedimentary sequence above the igneous rocks of Unit IV (Fig. 36). These unconformities bound lithologic units that vary considerably in lithology and give clues about the tectonic development of the region. All of the unconformities are restricted to the lower part of the sedimentary sequence, beneath 58 mbsf.

Nannofossil chalk of Unit III appears to be in unconformable contact with volcanic breccia of Unit IV. This contact may be a subaerially eroded surface. The chalk is of early to late Oligocene age compared to the middle Eocene(?) age of Unit IV. Sediments of Unit III exhibit bioturbation and abundant dewatering structures.

Unconformably overlying Unit III is the upper Miocene to lower Pliocene foraminiferal ooze of Subunit IIB. The unconformity represents a major hiatus (~69 mbsf) of about 18 m.y., extending from late Oligocene (~24 Ma) to early Pliocene (~6 Ma); missing are deposits of the latest Oligocene and almost the entire Miocene epochs. At Deep Sea Drilling Project (DSDP) Site 286, located in the North Loyalty Basin approximately 120 km south of Site 828, the absence of Miocene strata indicates an important hiatus between 13 and 5 Ma (Shipboard Scientific Party, 1975), suggesting a regional elevation of the seafloor to a level where erosion occurred or deposition was curtailed. Subunit IIB is a very soupy foraminiferal ooze of late Miocene to early Pliocene age (6–4 Ma) that is unconformably(?) overlain by foraminiferal ooze of Subunit IIA, which is late Pleistocene (<1 Ma) in age. A hiatus of 3–5 m.y. may exist near 62 mbsf where sediments of middle Pliocene to middle Pleistocene age are missing. At least five paleomagnetic reversals have been recorded in the sediments of Units II and III. Units II through III were deposited in a lower bathyal environment during a time of low sedimentation rates, between 2 and 7 m/m.y., as calculated from the microfossil analyses. Above Subunit IIA a major lithologic change from the foraminiferal ooze and nannofossil chalks of Units II and III to the volcanic siltstones of Unit I occurs, although the depositional environment remains lower bathyal (Fig. 36). Unit I was deposited during the Brunhes Chron (within the last 700 k.y.) at a time of a high sedimentation rate (~60 m/m.y.). It consists primarily of Pleistocene volcanic silt interlayered with ash. Many interbeds, some with scoured bases, of normally graded, sandy volcanic silt with foraminifers occur indicating sedimentation on a slope with possible turbidity transport. A greater influence of volcanic sedimentation, as indicated by ash layers, appears to have occurred at Site 828 during the Pleistocene, indicating close proximity to a volcanic source.

Although logging was not done at Site 828 because of hole problems, physical properties measurements and fluid chemistry assisted in the definition of the lithostratigraphic units. Magnetic susceptibility and porosity curves are represented in Figure 36 and correlate well with the four lithostratigraphic units. Distinct "kicks" are given on both curves, and magnetic susceptibility remains high throughout Unit I, reaching zero at Unit II, increasing slightly through Unit III and becoming high again in Unit IV. Porosity increases slightly in

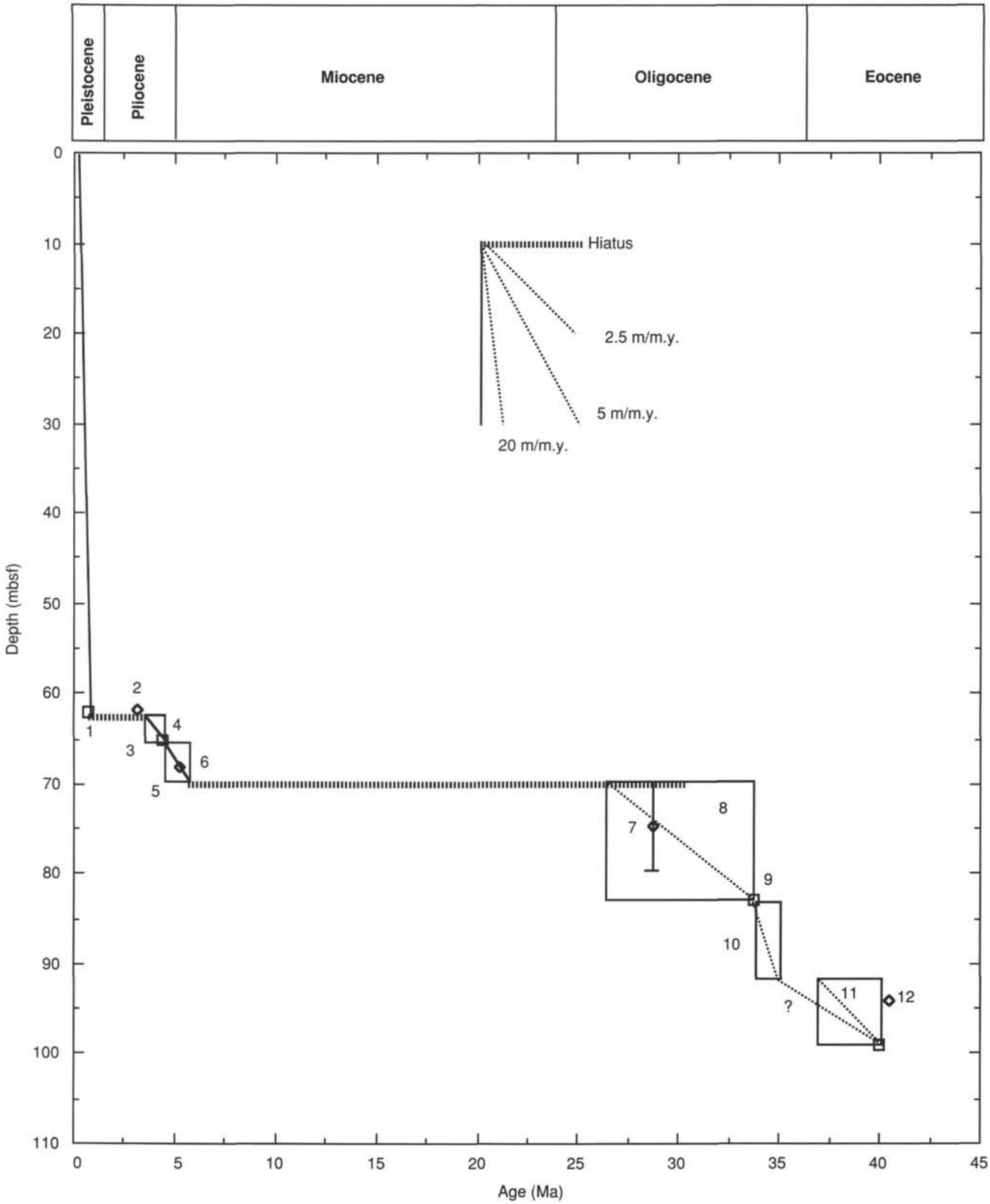

Figure 31. Sediment accumulation rates, Holes 828A and 828B (depth-vs.-age curve). Numbers refer to chronostratigraphic events and zones in Table 6.

Table 6. Chronostratigraphic events at Site 828.

Number	Datum levels/zones	Interval	Age (Ma)
1	Base of Brunhes Chron	Section 134-828A-7H-CC	0.73
2	FO *Gephyrocapsa oceanica*	Core 134-828A-7H (hiatus)	1.6
3	CN11 nannofossil zone	Between Sections 134-828A-8H-1 and -8H-4	3.56–4.4
4	LO *Ceratolithus primus*	Section 134-828A-8H-4	4.4
5	CN10 nannofossil zone	Between Sections 134-828A-8H-4 and -8H-6	4.4–5.5
6	FO *Globorotalia tumida*	Between Sections 134-828A-8H-2 and -8H-5	5.2
7	LO *Globorotalia opima*	Between Sections 134-828A-8H-CC and -9H-CC	28.2
8	CP17/19 nannofossil zone	Between Section 134-828A-8H-6 and Core 134-828A-10H	<33.8
9	LO *Reticulofenestra umbilica*	Within Core 134-828A-10H	33.8
10	CP16c nannofossil zone	Within Core 134-828A-10H and Section 134-828A-10H-CC	33.8–34.9
11	CP15 nannofossil zone	Within Core 134-828B-1R	36.7–40.0
12	LO *Truncorotaloides* spp.	Above Section 134-828A-11H-CC	40.6

Note: FO = first occurrence; LO = last occurrence.

Table 7. Index properties data, Site 828.

Sample (cm)	Depth (mbsf)	Unit	Wet-bulk density (Mg/m³)	Dry-bulk density (Mg/m³)	Grain density (Mg/m³)	Porosity Wet (%)	Porosity Dry (%)	Water content Wet (%)	Water content Dry (%)
134-828A-									
1H-1, 117	1.17	I	1.79	1.14	2.75	63.1	60.6	36.2	56.7
1H-2, 127	2.77	I	1.85	1.25	2.65	58.9	55.8	32.6	48.3
1H-3, 95	3.95	I	1.90	1.29	2.68	58.9	55.2	31.8	46.6
2H-1, 101	5.41	I	1.86	1.25	2.67	59.9	56.4	32.9	49.0
2H-3, 102	8.42	I	1.85	1.26	2.70	57.6	55.5	31.9	46.8
2H-5, 103	11.4	I	1.92	1.32	2.71	58.5	54.8	31.2	45.4
2H-7, 54	13.9	I	1.96	1.38	2.71	57.5	53.4	30.0	42.9
3H-1, 120	15.1	I	1.90	1.29	2.67	58.8	55.0	31.8	46.5
3H-5, 125	21.2	I	1.88	1.28	2.71	58.1	55.4	31.7	46.5
3H-7, 10	23.0	I	1.88	1.26	2.71	60.5	56.7	32.9	49.0
4H-1, 110	24.5	I	1.89	1.27	2.72	60.8	56.9	33.0	49.2
4H-3, 110	27.5	I	1.88	1.27	2.65	59.6	55.7	32.4	48.0
4H-5, 110	30.5	I	1.87	1.24	2.70	61.3	57.4	33.6	50.5
5H-2, 110	35.5	I	1.76	1.12	2.63	62.7	59.8	36.4	57.3
5H-4, 110	38.5	I	1.83	1.20	2.66	60.8	57.7	34.1	51.8
5H-6, 110	41.5	I	1.88	1.26	2.73	60.8	57.2	33.1	49.5
6H-2, 105	45.0	I	1.82	1.21	2.62	60.2	56.9	33.8	51.1
6H-5, 105	49.5	I	1.83	1.21	2.74	60.7	58.2	34.0	51.6
6H-5, 137	49.8	I	1.82	1.17	2.65	63.2	59.1	35.5	55.2
6H-6, 105	51.0	I	1.70	1.00	2.70	67.8	64.9	40.9	69.3
7H-1, 143	53.3	I	1.75	1.07	2.71	65.7	62.6	38.5	62.7
7H-3, 143	56.3	I	1.77	1.10	2.82	65.3	62.8	37.8	60.7
7H-5, 143	59.3	IIA	1.73	1.04	2.70	67.8	64.1	40.1	66.8
7H-6, 143	60.8	IIA	1.75	1.07	2.76	65.6	63.0	38.5	62.5
8H-1, 140	62.8	IIB	1.54	0.80	2.71	72.2	71.3	48.1	92.6
8H-3, 140	65.8	IIB	1.50	1.00	3.03	48.6	59.8	33.3	49.9
8H-5, 140	68.8	IIB	1.64	0.96	2.69	66.4	65.3	41.4	70.8
8H-6, 140	70.3	III	1.83	1.21	2.76	60.6	58.3	34.0	51.4
9H-1, 23	71.1	III	1.72	1.08	2.59	62.6	60.4	37.4	59.6
9H-3, 22	74.1	III	1.76	1.12	2.58	62.7	59.5	36.6	57.6
9H-4, 103	76.4	III	1.79	1.15	2.64	62.2	59.1	35.6	55.3
9H-5, 20	77.1	III	1.80	1.16	2.63	62.3	58.7	35.4	54.9
9H-7, 22	80.1	III	1.84	1.20	2.69	62.4	58.6	34.7	53.2
10H-1, 37	80.8	III	1.61	1.00	2.24	59.3	57.2	37.7	60.5
10H-5, 37	86.8	III	1.85	1.20	2.83	63.4	60.2	35.2	54.2
11H-1, 37	90.3	III	1.66	0.99	2.71	65.4	64.5	40.4	67.7
134-828B-1R-2, 130	92.8	III	1.73	1.05	2.75	66.0	63.6	39.1	64.2
134-828A-11H-3, 37	93.3	IV	2.15	1.76	2.63	38.2	36.6	18.2	22.3
134-828B-1R-6, 3	97.5	III	1.78	1.13	2.70	63.1	60.3	36.4	57.1

Unit I from about 59% to 68%, varying considerably from 49% to 72% in the soupy foraminiferal ooze of Unit II, remaining fairly constant between 62% and 66% in the nannofossil chert of Unit III, and exhibiting a sharp decrease from 66% to about 36% in the volcanic breccia of Unit IV.

Interstitial fluids of Hole 828A have chloride concentrations that reach values at 50 mbsf of 570 mM, approximately 2% higher than seawater, which may result from local ash alteration or perhaps mixing with chloride-rich fluids from the accretionary wedge. Potassium, sodium, and magnesium decrease with depth whereas calcium concentrations increase. This may result from diagenetic exchange reactions with the volcanic ash-rich sediments and basement igneous rocks.

Initial examination of the cores from Site 828 suggests that the eastern terminus of the NDR formed in close association with a volcanic island arc. Igneous rocks recovered in both Holes 828A and 828B support the view that the ridge may have originated along a subduction zone as proposed by Daniel et al. (1977) and Maillet et al. (1983). During the Eocene, volcanic breccia and lava flows built up the flank of

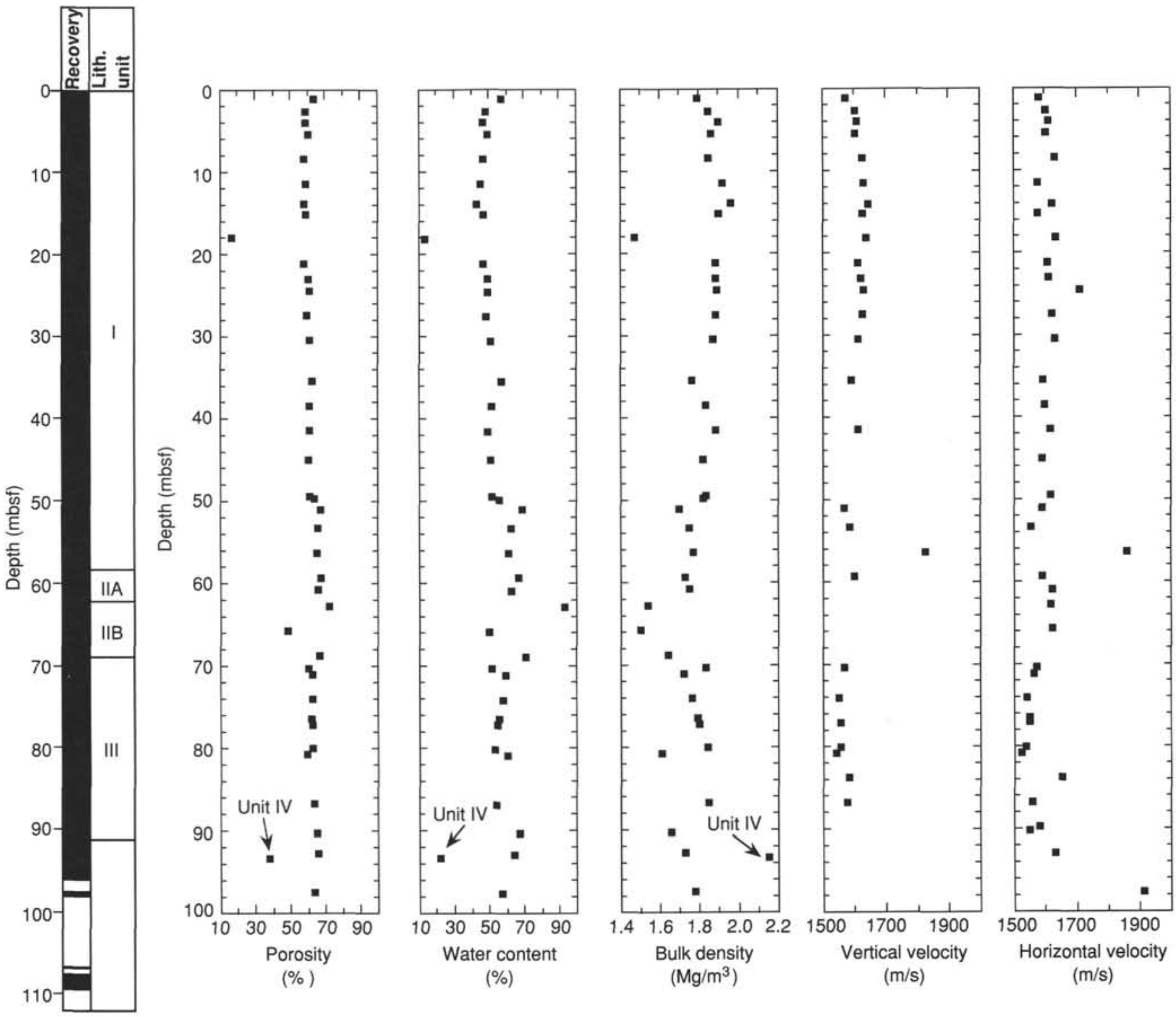

Figure 32. Porosity, water content, bulk density, and vertical and horizontal velocities vs. depth, Site 828.

the ridge of Site 828 where the highly oxidized volcanic rubble was drilled. Subsidence of the ridge then occurred, followed by the deposition of over 21.5 m of pelagic nannofossil ooze during the early to late Oligocene (~7–12 m.y.). This was a time of low deposition rate as indicated by the ~5 m/yr average sediment accumulation rate and the presence of small manganese nodules found in Unit III. Sometime between the late Oligocene and late Miocene, probable elevation and perhaps emergence of the NDR took place, causing complete removal or nondeposition of sediment, thus producing the 18-m.y. hiatus.

Subsidence recurred with slow deposition of the pelagic foraminiferal ooze during the late Miocene to early Pliocene. This unconsolidated, highly permeable unit is an aquifer that may facilitate transport of fluids away from the subduction zone. Sometime during the Pliocene, sea level fell or elevation may have once again occurred, perhaps in association with the arrival of the present eastern terminus of the NDR, including the location of Site 828 at the outer bulge, causing erosion or preventing deposition to produce the hiatus of 3–5 m.y.

Sedimentation rate during the Pleistocene increased considerably to ~60 m/m.y. with the influx of volcanic silts and ash. This was most likely in response to the convergence of the NDR, including Site 828, with the New Hebrides Island Arc. Sedimentation was influenced both by ash fall and hemipelagic contribution from the active volcanoes of the island arc. Geochemical analyses of some of the Pleistocene ashes indicate that they originated from explosive events associated with the volcanically active Central Chain, some 150 km to the southeast. Site 828 is currently about to be subducted beneath the forearc of the central New Hebrides Island Arc and appears to be undergoing initial tensional faulting in response to the bending of the lithosphere in this area.

REFERENCES

Bienvenu, P., Bougault, H., Joron, J. L., Treuil, M., and Dmitriev, L., 1990. MORB alteration: rare-earth element/non-rare-earth hygromagmato-phile element fractionation. *Chem. Geol.*, 82:1–14.

Briqueu, L., Bougault, H., and Joron, J. L., 1984. Quantification of Nb, Ta, Ti and V anomalies in magmas associated with subduction zones: petrogenetic implications. *Earth Planet. Sci. Lett.*, 68:297–308.

Burne, R. V., Collot, J.-Y., and Daniel, J., 1988. Superficial structures and stress regimes of the downgoing plate associated with subduction-collision in the Central New Hebrides Arc (Vanuatu). *In* Greene, H. G., and Wong, F. L. (Eds.), *Geology and Offshore Resources of Pacific Island Arcs—Vanuatu Region*. Circum-Pac. Council Energy Miner. Resour., Earth Sci. Ser., 8:357–376.

Collot, J.-Y., Daniel, J., and Burne, R. V., 1985. Recent tectonics associated with the subduction/collision of the d'Entrecasteaux zone in the central New Hebrides. *Tectonophysics*, 112:325–356.

Collot, J.-Y., Pelletier, B., Boulin, J., Daniel, J., Eissen, J.-P., Fisher, M. A., Greene, H. G., Lallemand, S., and Monzier, M., 1989. Premiers résultats des plongées de la campagne SUBPSO1 dans la zone de collision des rides d'Entrecasteaux et de l'arc des Nouvelles Hébrides. *C. R. Acad. Sci. Ser. 2*, 309:1947–1954.

Daniel, J., Jouannic, C., Larue, B., and Récy, J., 1977. Interpretation of d'Entrecasteaux zone (north of New Caledonia). *Int. Symp. on Geodyn. in South-west Pac., Noumea, New Caledonia, 1976*. Paris (Editions Technip), 117–124.

Dupuy, C., Dostal, J., Marcelot, G., Bougault, H., Joron, J. L., and Treuil, M., 1982. Geochemistry of basalts from central and southern New Hebrides arc: implication for their source rock composition. *Earth Planet. Sci. Lett.*, 60:207–225.

Fisher, M. A., 1986. Tectonic processes at the collision of the d'Entrecasteaux zone and the New Hebrides island arc. *J. Geophys. Res.*, 91:10470–10486.

Fisher, M. A., Collot, J-Y., and Geist, E. L., 1991. The collision zone between the North d'Entrecasteaux Ridge and the New Hebrides Island arc. Part 2: structure from multichannel seismic data *J. Geophys. Res.*, 96:4479–4495.

Fisher, M. A., Collot, J.-Y., and Smith, G. L., 1986. Possible causes for structural variation where the New Hebrides island arc and the d'Entrecasteaux zone collide. *Geology*, 14:951–954.

Gieskes, J. M., Blanc, G., Vrolijk, P., Elderfield, H., and Barnes, R., 1990. Interstitial water chemistry—major constituents. *In* Moore, J. C., Mascle, A., et al., *Proc. ODP, Sci. Results*, 110: College Station, TX (Ocean Drilling Program), 155–178.

Hart, S. R., Erlank, A. J., and Kable, J. D., 1974. Sea floor basalt alteration: some chemical and Sr isotopic effects. *Contrib. Mineral. Petrol.*, 44:219–230.

Hills, S. J., and Thierstein, H. R., 1989. Plio-Pleistocene calcareous plankton biochronology. *Mar. Micropaleontol.*, 14:67–96.

Kennett, J. P., and Srinivasan, M. S., 1983. *Neogene Planktonic Foraminifera: A Phylogenetic Atlas:* Stroudsburg, PA (Hutchinson Ross).

Kroenke, L. W., Jouannic, C., and Woodward, P. (Compilers), 1983. Bathymetry of the southwest Pacific, Chart 1: *Geophysical Atlas of the Southwest Pacific*, Scale 1:6,442,192 at 0°, Suva, Fiji. U. N. Econ. Soc. Comm. Asia Pac., CCOP/SOPAC Tech. Secretariat.

Luyendyk, B. P., Bryan, W. B., and Jezek, P. A., 1974. Shallow structure of the New Hebrides island arc. *Geol. Soc. Am. Bull.*, 85:1287–1300.

Maillet, P. M., Monzier, M., Selo, M., and Storzer, D., 1983. The d'Entrecasteaux zone (southwest Pacific): a petrological and geochronological reappraisal. *Mar. Geol.*, 53:179–197.

Mascle, A., Moore, J. C., et al., 1988. *Proc. ODP, Init. Repts.*, 110: College Station, TX (Ocean Drilling Program).

McDuff, R. E., 1981. Major cation gradients in DSDP interstitial waters: the role of diffusive exchange between seawater and the upper ocean crust. *Geochim. Cosmochim. Acta*, 45:1701–1713.

McDuff, R. E., and Gieskes, J. M., 1976. Calcium and magnesium profiles in DSDP interstitial water: diffusion or reaction? *Earth Planet. Sci. Lett.*, 33:1–10.

Pearce, J. A., 1982. Trace element characteristics of lavas from destructive plate boundaries. *In* Thorpe, R. S. (Ed.), *Andesites: Orogenic Andesites and Related Rocks:* New York (Wiley), 525–548.

Pearce, J. A., and Cann, J. R., 1973. Tectonic setting of basic volcanic rocks determined using trace element analysis. *Earth Planet. Sci. Lett.*, 24:419–426.

Serri, G., Spadea, P., Beccaluva, L., Civetta, L., Coltorti, M., Dostal, J., Sajona, F., Vaccaro, C., and Zeda, O., 1991. Petrology of igneous rocks from the Celebes Sea basement. *In* Rangin, C., Silver, E. A., von Breymann, M. T., et al., *Proc. ODP, Sci. Results*, 124: College Station, TX (Ocean Drilling Program), 271–296.

Shipboard Scientific Party, 1975. Site 286. *In* Andrews, J. E., Packham, G., et al., *Init. Repts. DSDP*, 30: Washington (U.S. Govt. Printing Office), 69–131.

Spadea, P., Beccaluva, L., Civetta, L., Coltorti, M., Dostal, J., Sajona, F., Serri, G., Vaccaro, C., and Zeda, O., 1991. Petrology of basic igneous rocks from the floor of the Sulu Sea. *In* Rangin, C., Silver, E. A., von Breymann, M. T., et al., *Proc. ODP, Sci. Results*, 124: College Station, TX (Ocean Drilling Program), 251–270.

Wilson, M., 1989. *Igneous Petrogenesis: A Global Tectonic Approach:* London (Unwin Hyman).

Ms 134A-108

NOTE: All core description forms ("barrel sheets") and core photographs have been printed on coated paper and bound as Section 4, near the back of this volume, beginning on page 581.

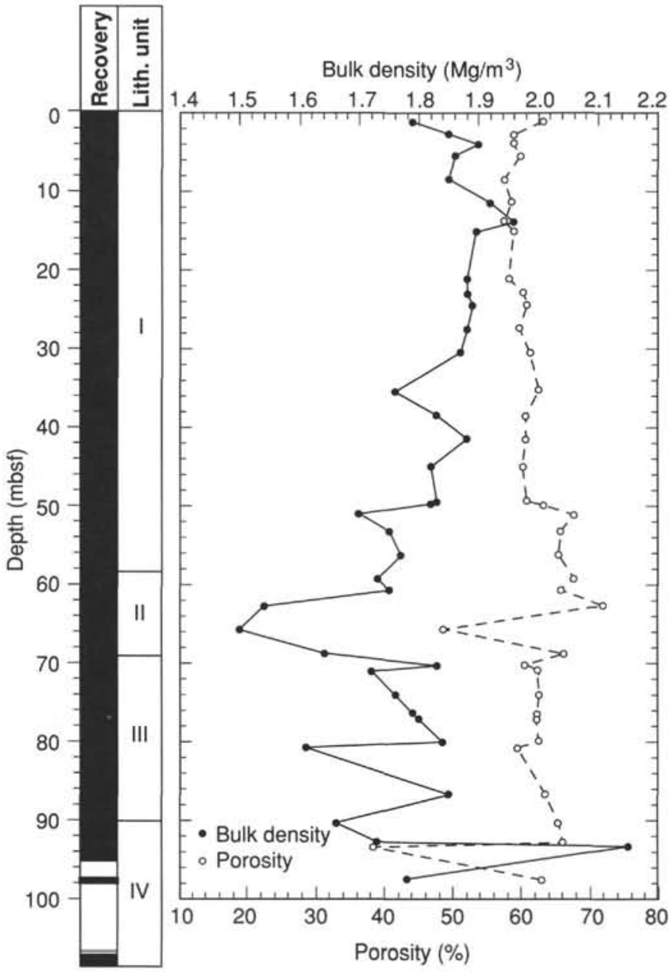

Figure 33. Porosity and bulk density vs. depth, Site 828.

Table 8. Vertical and horizontal velocity data, Site 828A.

Sample (cm)	Depth (mbsf)	Unit	Vertical velocity (m/s)	Wave type[a]	Horizontal velocity (m/s)	Wave type[a]
134-828A-						
1H-1, 112	1.12	I	1573	C	1583	C
1H-2, 127	2.77	I	1605	C	1601	C
1H-3, 95	3.95	I	1606	C	1610	C
2H-1, 101	5.41	I	1602	C	1601	C
2H-3, 102	8.42	I	1625	C	1628	C
2H-5, 103	11.43	I	1631	C	1577	C
2H-7, 54	13.94	I	1641	C	1620	C
3H-1, 120	15.10	I	1627	C	1576	C
3H-3, 122	18.12	I	1637	C	1635	C
3H-5, 125	21.15	I	1612	C	1608	C
3H-7, 10	23.00	I	1621	C	1613	C
4H-1, 110	24.50	I	1629	C	1707	C
4H-3, 110	27.50	I	1624	C	1622	C
4H-5, 110	30.50	I	1610	C	1628	S
5H-2, 110	35.50	I	1589	S	1594	S
5H-4, 110	38.50	I			1597	S
5H-6, 110	41.50	I	1612	S	1618	S
6H-2, 105	44.95	I			1589	S
6H-5, 105	49.45	I			1614	S
6H-6, 105	50.95	I	1569	S	1589	S
7H-1, 143	53.33	I	1584	C	1556	C
7H-3, 143	56.33	I	1825	S	1859	S
7H-5, 143	59.33	IIA	1598	C	1590	C
7H-6, 143	60.83	IIA			1620	S
8H-1, 134	62.74	IIB			1614	C
8H-3, 122	65.62	IIB			1621	C
8H-6, 140	70.30	III	1569	C	1573	S
9H-1, 29	71.19	III			1562	C
9H-3, 17	74.07	III	1550	C	1540	C
9H-4, 103	76.43	III			1550	C
9H-5, 11	77.01	III	1556	C	1551	C
9H-7, 16	80.06	III	1555	C	1539	C
10H-1, 37	80.77	III	1541	C	1525	C
10H-3, 37	83.77	III	1579	C	1652	C
10H-5, 37	86.77	III	1575	C	1560	C
10H-7, 37	89.77	III			1583	C
11H-1, 32	90.22	III			1548	C
134-828B-						
1R-2, 136	92.86	III			1630	C
1R-6, 15	97.65	III			1912	C

[a] C = compressional (*P*-wave) and S = shear (*S*-wave).

Table 9. Shear-strength data, Site 828.

Sample (cm)	Depth (mbsf)	Unit	Method[a]	Undrained shear strength (kPa)
134-828A-				
1H-1, 100	1.00	I	SP	12.5
1H-2, 122	2.72	I	SP	38.1
1H-3, 90	3.90	I	SP	46.2
2H-1, 95	5.35	I	SP	59.4
2H-3, 97	8.37	I	SP	50.6
2H-5, 95	11.35	I	SP	60.9
2H-7, 46	13.86	I	SP	51.3
3H-1, 129	15.19	I	SP	63.1
3H-3, 115	18.05	I	SP	61.6
3H-5, 131	21.21	I	SP	89.4
3H-7, 5	22.95	I	SP	61.6
4H-1, 125	24.65	I	SP	85.0
4H-3, 116	27.56	I	SP	69.6
4H-5, 103	30.43	I	SP	103.4
5H-2, 116	35.56	I	SP	78.4
5H-4, 106	38.46	I	SP	88.0
5H-6, 116	41.56	I	SP	93.1
6H-2, 113	45.03	I	SP	76.2
6H-5, 123	49.63	I	SP	115.8
6H-6, 112	51.02	I	SP	209.7
7H-1, 138	53.28	I	SP	129.4
7H-3, 138	56.28	I	SP	104.2
7H-5, 139	59.29	IIA	SP	83.6
7H-6, 139	60.79	IIA	SP	36.6
8H-6, 136	70.26	III	SP	51.5
9H-1, 32	71.22	III	TD	63.9
9H-3, 24	74.14	III	TD	44.8
9H-7, 23	80.13	III	SP	74.4
10H-1, 35	80.75	III	TD	48.2
10H-3, 42	83.82	III	TD	116.5
10H-5, 34	86.74	III	TD	142.3
10H-7, 36	89.76	III	TD	39.2

[a] SP = Wykeham-Farrance spring vane-shear apparatus; TD = ODP motorized miniature vane shear (torvane device).

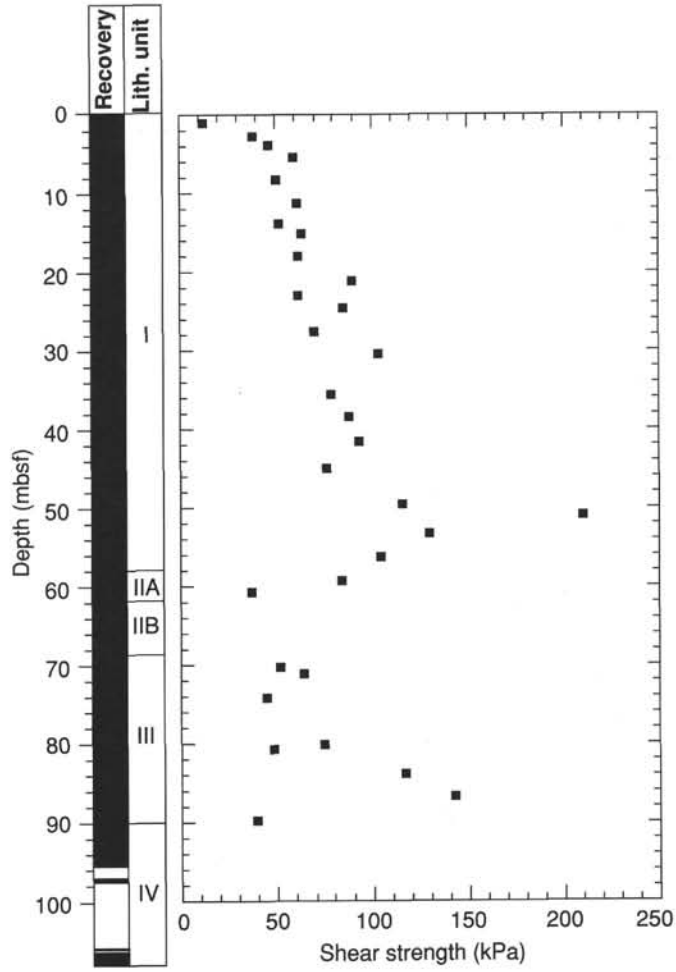

Figure 34. Shear strength vs. depth, Site 828.

Table 10. Thermal conductivity data, Site 828.

Sample (cm)	Depth (mbsf)	Unit	Value (W/[m · K])
134-828A-			
1H-1, 75	0.75	I	1.0484
1H-2, 75	2.25	I	1.0969
1H-3, 60	3.60	I	0.9225
2H-1, 75	5.15	I	1.1154
2H-2, 75	6.65	I	1.0278
2H-4, 75	9.65	I	1.0235
2H-6, 75	12.65	I	1.0148
3H-1, 75	14.65	I	1.0348
3H-3, 75	17.65	I	1.0338
3H-4, 75	19.15	I	1.0097
3H-6, 75	22.15	I	1.0385
4H-1, 75	24.15	I	0.9409
4H-3, 75	27.15	I	0.9655
4H-5, 75	30.15	I	0.9910
4H-7, 20	32.60	I	1.0001
5H-1, 75	33.65	I	0.9893
5H-3, 75	36.65	I	0.9166
5H-5, 75	39.65	I	1.0269
5H-6, 75	41.15	I	1.0125
6H-1, 75	43.15	I	0.9886
6H-3, 75	46.15	I	0.9868
6H-5, 75	49.15	I	1.0393
6H-6, 75	50.65	I	0.9889
7H-1, 90	52.80	I	1.0397
7H-3, 90	55.80	I	0.9315
7H-4, 90	57.30	I	0.9595
7H-6, 90	60.30	IIA	0.9115
8H-6, 75	69.65	IIA	1.4793
8H-7, 20	70.60	III	1.1708
9H-1, 75	71.65	III	1.3874
9H-3, 75	74.65	III	1.1611
9H-5, 75	77.65	III	1.2263
9H-7, 35	80.25	III	1.2114
10H-1, 75	81.15	III	1.4077
10H-3, 75	84.15	III	1.2410
10H-4, 75	85.65	III	1.1657
10H-6, 75	88.65	III	1.2558
11H-1, 75	90.65	III	1.1486
11H-2, 50	91.90	III	1.6040
11H-4, 35	94.75	III	1.5541

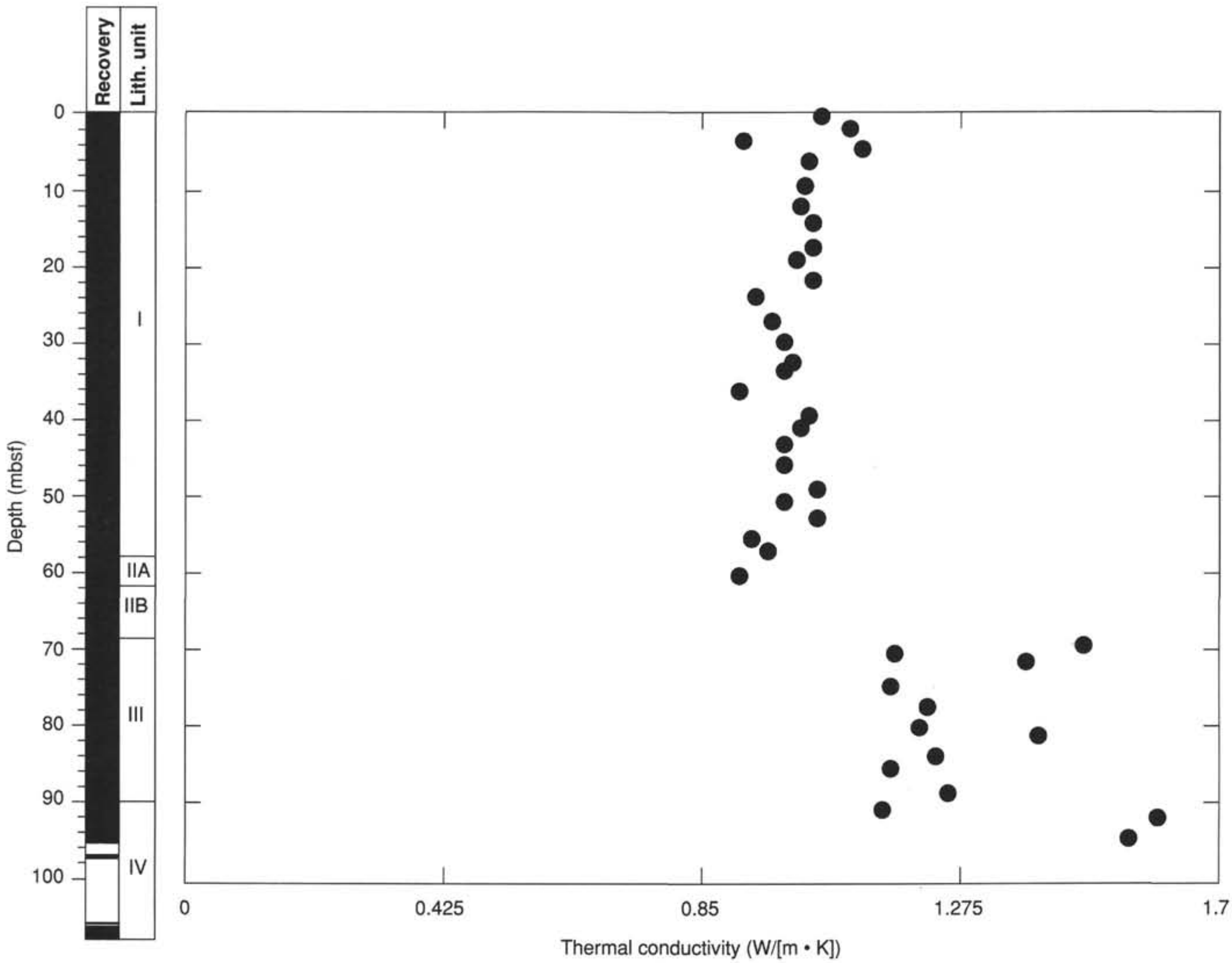

Figure 35. Thermal conductivity (W/[m · K]) vs. depth, Site 828.

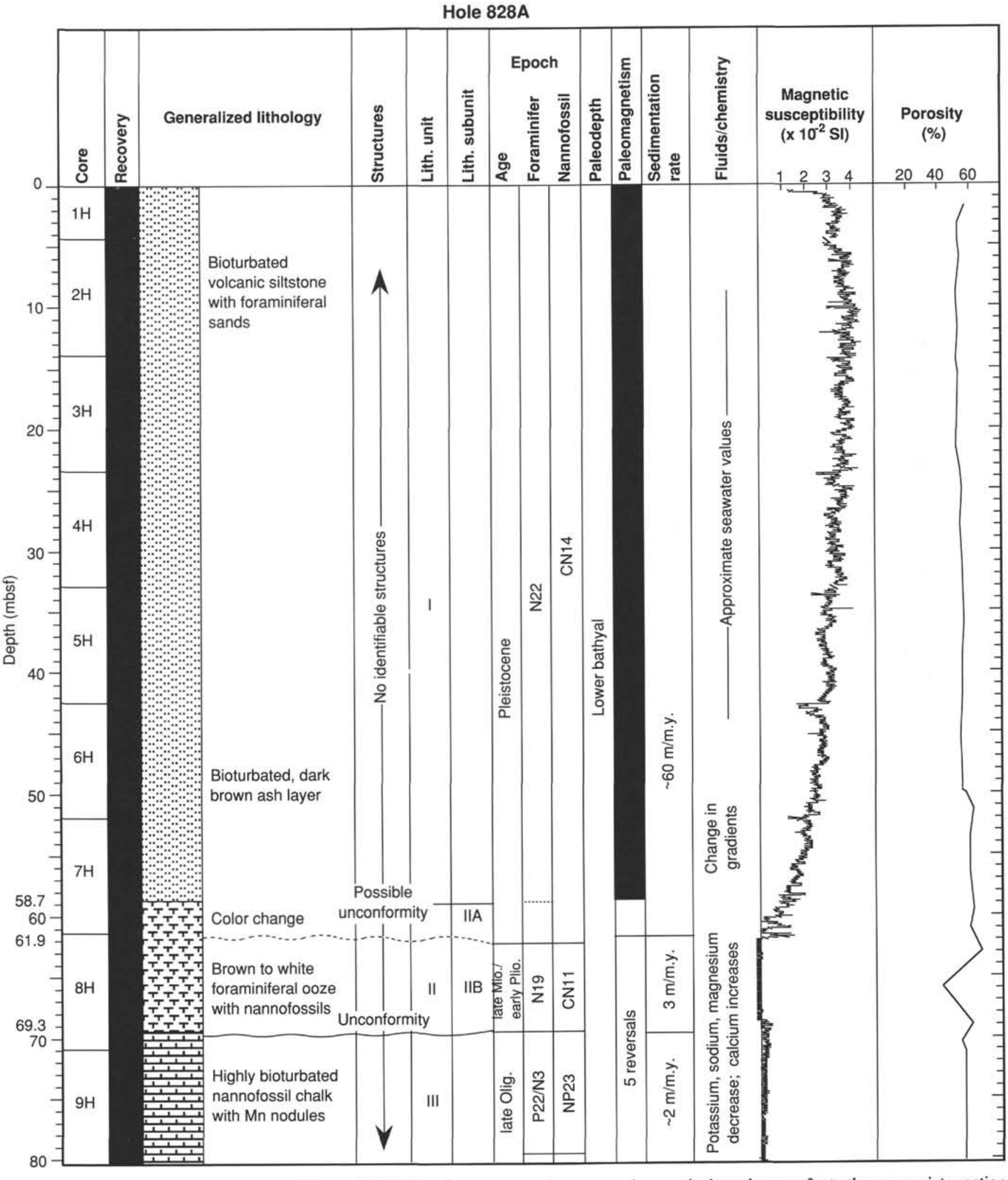

Figure 36. Generalized summary of Holes 828A and 828B. If no data or annotations appear in a particular column, refer to the appropriate section of this chapter for information.

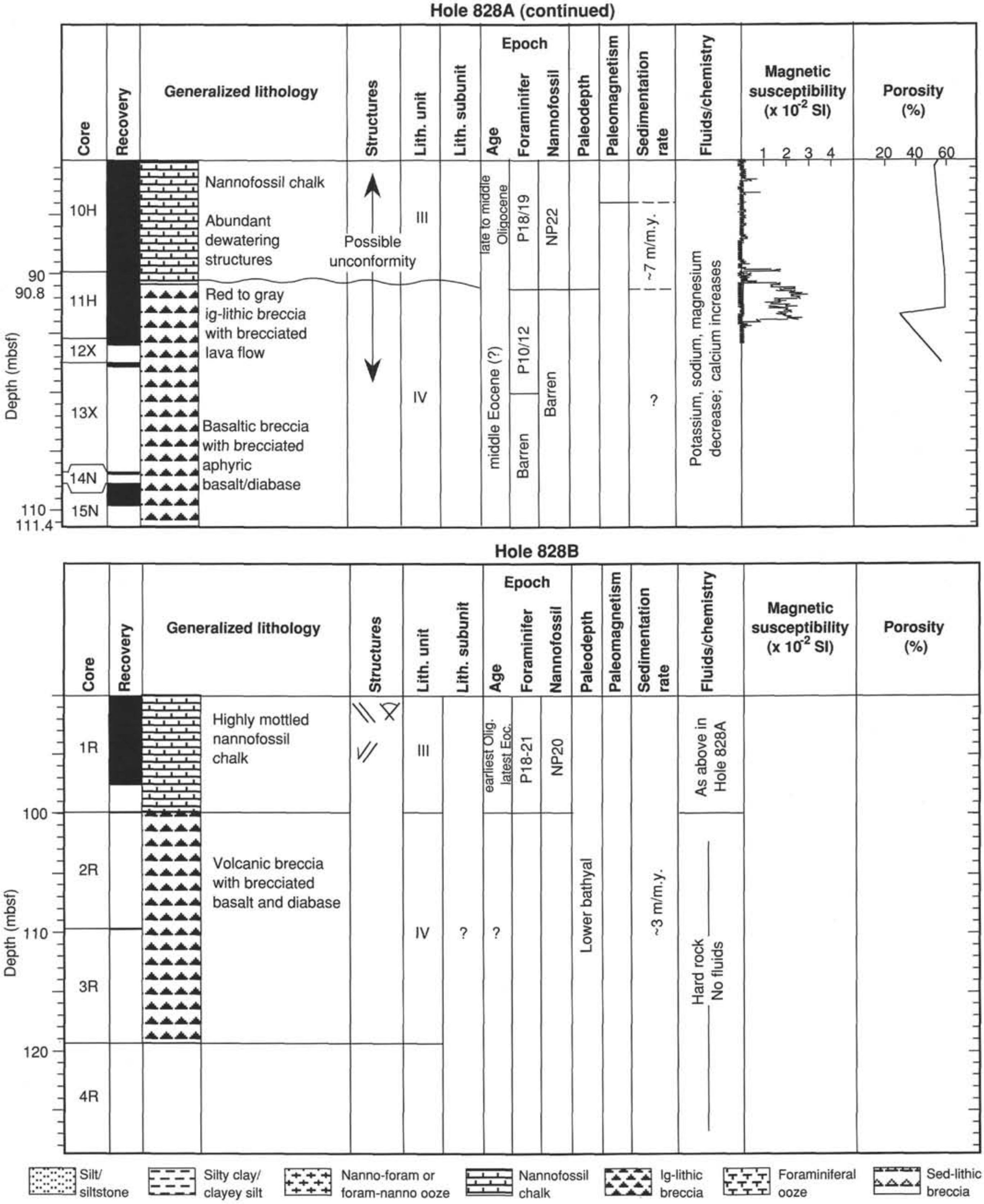

Figure 36 (continued).